

UCLA

UCLA Electronic Theses and Dissertations

Title

The Role of Surface in Photovoltaic Perovskites: From Quantum Dots to Bulk Thin films

Permalink

<https://escholarship.org/uc/item/9ht8c3s8>

Author

Xue, Jingjing

Publication Date

2020

Peer reviewed|Thesis/dissertation

UNIVERSITY OF CALIFORNIA

Los Angeles

The Role of Surface in Photovoltaic Perovskites: From Quantum Dots to Bulk Thin films

A dissertation submitted in partial satisfaction of the
requirements for the degree Doctor of Philosophy
in Materials Science and Engineering

by

Jingjing Xue

2020

© Copyright by
Jingjing Xue
2020

ABSTRACT OF THE DISSERTATION

The Role of Surface in Photovoltaic Perovskites: From Quantum Dots to Bulk Thin Films

by

Jingjing Xue

Doctor of Philosophy in Materials Science and Engineering

University of California, Los Angeles, 2020

Professor Yang Yang, Chair

The surface of a semiconductor often has a key role in determining its properties. For metal halide perovskites, understanding the surface features and their impact on the materials and devices is becoming increasingly important. At length scales down to the nanoscale regime, surface features become dominant in regulating the properties of perovskite materials owing to the high surface-to-volume ratio. For perovskite bulk films in the micrometer range, defects and structural disorder readily form at the surface and affect device performance. Through concerted efforts to optimize processing techniques, high-quality perovskite thin films can now be fabricated with monolayer-like polycrystalline grains or even single crystals. Surface defects, therefore, remain the major obstacle to progress, pushing surface studies to the forefront of perovskite research. Hence, research towards fundamental understanding of perovskite surfaces and how they can affect the materials properties is crucial to further improving the perovskite-based optoelectronic devices.

In Chapter 2, surface energies will be shown to play an important role in affecting the phase stability of perovskite materials. Thermodynamic and crystallographic analyses revealed that enhanced contribution of the surface energy and lattice contraction contribute to the superior stability of colloidal quantum dots (CQDs). This approach provides a new route for achieving stable formamidinium lead iodide (FAPbI₃) perovskite solar cells. Later on, in Chapter 3, a conjugated small molecule ITIC was introduced into the FAPbI₃ CQDs perovskite solar cells to further enhance the power conversion efficiency of the devices.

In Chapter 4, I will show that in lead halide perovskites, how their “soft” nature renders them highly responsive to the external field, allowing for extended depth scale affected by the surface. By taking advantage of this unique feature of perovskites, I demonstrate a methodology for property manipulation of perovskite thin films based on secondary grain growth, where tuning of the surface induces the internal property evolution of the entire perovskite film. While in conventional microelectronic techniques secondary grain growth generally involves harsh conditions such as high temperature and straining, it is easily triggered in a perovskite thin film by a simple surface post-treatment, producing enlarged grain sizes of up to 4 μm. The resulting photovoltaic devices exhibit significantly enhanced power conversion efficiency and operational stability over a course of 1000 h and an ambient shelf stability of over 4000 h while maintaining over 90% of its original efficiency.

Surface trap-mediated non-radiative charge recombination is a major limit to achieving high-efficiency metal-halide perovskite photovoltaics. The ionic character of perovskite lattice has enabled molecular defect passivation approaches via interaction between functional groups and

defects. However, a lack of in-depth understanding of how the molecular configuration influence the passivation effectiveness is a challenge to rational molecule design. In Chapter 5, the chemical environment of a functional group that is activated for defect passivation was systematically investigated with theophylline, caffeine and theobromine. When N-H and C=O were in an optimal configuration within the molecule, hydrogen-bond formation between N-H and I assisted the primary C=O binding with the antisite Pb defect to maximize surface-defect binding. A stabilized power conversion efficiency of 22.6% of photovoltaic device was demonstrated with theophylline treatment.

The dissertation of Jingjing Xue is approved.

Yu Huang

Richard B. Kaner

Chong Liu

Yang Yang, Committee Chair

University of California, Los Angeles

2020

Table of Contents

Chapter 1 Introduction to the surface features of halide perovskites	1
1.1 Surface terminations and disorders.....	3
1.2 Surface electronic structures and properties	7
1.3 Surface features of perovskite quantum dots.....	10
References.....	12
Chapter 2 Surface Ligand Management for Stable FAPbI ₃ Perovskite Quantum Dot Solar Cells.....	25
2.1 Synthesis and surface ligand treatment of FAPbI ₃ CQDs.....	26
2.2 Device performance of FAPbI ₃ CQDs based solar cells	31
2.3 Improved stability of FAPbI ₃ CQDs.....	33
References.....	37
Chapter 3 Small Molecule ‘Charge Driver’ Enables Perovskite Quantum Dot Solar Cells with Efficiency Approaching 13%	51
3.1 The effect of ITIC on the photovoltaic performance of CQDs based device	53

3.2 Properties and carrier dynamics of CQDs thin films.....	54
3.3 Conclusion.....	58
Chapter 4 Crystalline Liquid-like Behavior: Surface-Induced Secondary Grain Growth of Photovoltaic Perovskite Thin Film.....	67
4.1 Theoretical modeling of the driving force.....	68
4.2 Characterizations of the grain growth and film properties.....	69
4.3 Device performance and stability	73
4.4 Conclusion.....	76
References.....	77
Chapter 5 Constructive molecular configurations for surface-defect passivation of perovskite photovoltaics.....	85
References.....	94
Appendix A.....	103
Appendix B.....	141

List of Figures

Figure 1.1 a | Side views of three representative surface terminations in MAPbI₃ (where MA⁺ is methylammonium). **b** | The 12 types of native point defects found in metal halide perovskites. V_Y denotes a Y vacancy, Y_i denotes an interstitial Y-site and Y_Z denotes a Z-site substituted by Y, where Y and Z represent an ion of APbX₃ (where A⁺ is a monovalent cation and X⁻ a halide). **c** | Other surface features of metal halide perovskites include ion dimers (Pb²⁺ dimers and halide dimers), zigzag patterns, various orientations of the organic cations and the incursion of foreign species, such as O₂. The high-resolution scanning tunnelling microscopy images on the right show the formation of halide dimers (top) and a zigzag pattern (bottom) on the surface of MAPbI₃. The unit cells are denoted by dashed white rectangles. (Page 21)

Figure 1.2 a | The various ligand-binding motifs according to the covalent-bond-classification method, illustrated here for a metal chalcogenide nanoparticle. **b** | Various ligands and surface-treatment methods have been adopted in the synthesis of perovskite nanoparticles. The ligands have been classified by their function: to improve the luminescent properties, enhance the electronic coupling or increase stability. The prototypical oleylamine–oleic acid ligand pairs used in the synthesis of metal halide perovskite quantum dots result in surface binding involving oleylammonium halide or oleylammonium oleate, as depicted in blue. **c** | Calculated defect-formation energies for interstitial, charged and neutral vacancies, and antisite substitutions on the surface of CsPbBr₃ quantum dots (where C is core, SC is surface centre and SE is surface edge). V_Y denotes a Y vacancy, Y_i denotes an interstitial Y-site and Y_Z denotes a Z-site substituted by Y, where Y and Z represent an ion of CsPbBr₃. The right superscript denotes the charge of the defect and a left superscript denotes the number of the defects considered when calculating the formation energy. Backflip means that the antisite displacement goes back to its initial non-defective configuration. Calculations were performed using density functional theory with the PBE functional. (Page 23)

Figure 2.1 (A) Transmission electron microscopic (TEM) image and (B) X-ray diffraction (XRD) patterns of as-synthesized FAPbI₃ CQDs and bulk films; δ and * indicate hexagonal non-perovskite phase and PbI₂, respectively. (C) UV-visible absorption (broken lines), steady-state photoluminescence (PL, solid lines) and (D) time-resolved PL spectra of CsPbI₃ CQDs (red) and FAPbI₃ CQDs (dark red). Open circles indicate measured data while solid lines are fitted curves. (Page 44)

Figure 2.2 The strategy for designing rational solvent-treatment routes to manage surface ligands of FAPbI₃ CQDs. (Page 45)

Figure 2.3 (A) Nuclear magnetic resonance (NMR) spectra of FAPbI₃ CQDs with increasing number of surface treatment cycles in solution, indicating a gradual decrease of the oleyl species (right) and schematic illustration of the ligand density control during solution-state surface treatment (left); (B) Fourier transform infrared (FTIR) spectra of FAPbI₃ CQDs before and after solid-state surface treatment (right) and a schematic illustration of the ligand density change and inter-dot coupling during the solid-state surface treatment (left). (Page 46)

Figure 2.4 (A) A Schematic device structure and cross sectional scanning electron microscopic (SEM) image of the FAPbI₃ CQDs solar cell; (B) current density-voltage (*J-V*) curves and (C) External quantum efficiency (EQE) of the devices based on FAPbI₃ CQDs with increasing cycles of surface treatment. (Page 47)

Figure 2.5 (A, B) UV-vis absorption spectra of (A) FAPbI₃ CQDs and (B) bulk FAPbI₃ stored under ambient condition (relative humidity $\sim 35 \pm 2\%$ and temperature 23 ± 3 °C). Inset of (A) and (B) shows corresponding photos of the films. (C, D) X-ray diffraction (XRD) patterns of (C) FAPbI₃ CQDs and (D) bulk FAPbI₃ films measured before and after the exposure. α : cubic perovskite phase, δ : hexagonal non-perovskite phase, *h*: hydrated perovskite phase. (Page 48)

Figure 2.6 (A) A schematic showing XRD measurement. Characteristic XRD peaks of (B) silicon substrate at plane (004), (C) at plane (001) and (D) at plane (002) of bulk FAPbI₃ and FAPbI₃ CQD films. (E) Evolution of power conversion efficiency (PCE) of photovoltaic devices based on bulk FAPbI₃ and FAPbI₃ CQDs stored under ambient condition without encapsulation. Inset of (E) shows photos of the device before and after the exposure. (F) Change in PCE of the encapsulated device under continuous illumination (90 ± 5 mW/cm²). The devices were maintained under open-circuit condition at room temperature (ca. 30 ± 3 °C). (Page 49)

Figure 3.1 Schematic diagram of FAPbI₃CQD/ITIC film fabrication (insert: chemical structure of ITIC). (Page 63)

Figure 3.2 a) A cross-sectional SEM image of the device structure. b) *J-V* curves of the devices based on FAPbI₃ CQDs with and without ITIC. c) Steady-state power conversion efficiency measurement of the device with ITIC. d) Distribution of PCEs measured from 40 solar cell devices. (Page 64)

Figure 3.3 a) Transmission electron microscopic (TEM) image of as-synthesized FAPbI₃ CQDs. b) UV-visible absorption, c) steady-state photoluminescence (open circles indicate measured data while solid lines are fitted curves), and d) TRPL spectra of FAPbI₃ CQDs with (red) and without (black) ITIC. (Page 65)

Figure 3.4 TA spectra of FAPbI₃ CQD film a) without and b) with ITIC (excitation power was 4 μJ/cm²). c) The dynamic of bleaching peak probed at ~770 nm of FAPbI₃ CQDs with and without ITIC. d) Schematic energy diagram showing charge transfer between FAPbI₃ CQDs and ITIC. e) TPV and f) TPC measurements of devices with and without ITIC. (Page 66)

Fig. 4.1 The effect of organic ammoniums on surface servicing as the driving force of surface induced secondary grain growth.

Optimized (100) slab model of perovskite with (A) BA, (B) OCA, (C) OLA termination by DFT-D3 method; Optimized (111) slab model of perovskite with (D) BA, (E) OCA, (F) OLA termination by DFT-D3 method. (Page 81)

Fig. 4.2 Demonstration of the surface induced secondary grain growth.

(A) Top-view SEM images of perovskite film with various treatments (IPA, BA, OCA and OLA). (B) Grain size statistical distribution of perovskite films with various treatments (IPA, BA, OCA and OLA). (C) Schematic demonstration of the process of surface induced secondary grain growth. (Page 82)

Fig. 4.3 Characterization of Perovskite film with the surface induced secondary grain growth by OLA.

(A) Evolution of the (100) peak position of perovskite film with OLA extracted from real-time in-situ GIWAXS measurement. (B and C) 2D GIWAXS patterns of perovskite films (B) without OLA treatment and (C) with OLA treatment. (D) Radially integrated intensity plots along (100) crystal plane from the 2D GIWAXS patterns in perovskite films with or without OLA treatment. (E) XPS data for Pb 4f_{7/2} and Pb 4f_{5/2} core level spectra in perovskite films with or without OLA treatment. (F) Time-of-flight secondary ion mass spectroscopy (TOF-SIMS) depth profile of perovskite film with OLA treatment. (Page 83)

Fig. 4.4 Enhanced photovoltaic performance and long-term stability of perovskite film with surface induced secondary grain growth by OLA.

(A) Current density–voltage (J – V) curves of perovskite solar cells with or without OLA treatment. (B) Normalized transient photovoltage decay of perovskite solar cells with or without OLA treatment. (C) Nyquist plots of perovskite solar cells with or without OLA treatment measured in the dark and at corresponding open-circuit voltages. (D) Normalized transient

photocurrent decay of perovskite solar cells with or without OLA treatment. (E) Evolution of power conversion efficiency (PCE) of perovskite solar cells with or without OLA treatment. The devices were stored under nitrogen with controlled temperature (85 °C). (F) Evolution of power conversion efficiency (PCE) of perovskite solar cells with or without OLA treatment. The devices were stored under dark with controlled humidity. (G) Evolution of the PCEs measured from the encapsulated perovskite solar cells with or without OLA treatment exposed to continuous light ($90 \pm 5 \text{ mW cm}^{-2}$) under open-circuit condition. (Page 84)

Fig. 5.1 Surface defect identification and constructive configuration of the C=O group in three different chemical environments.

(A) Chemical structures of three different passivation molecules. (top to bottom: Theophylline, Caffeine and Theobromine) (B) Top view of the various types of surface defects. (C) *J-V* curves of perovskite solar cells with or without small molecules treatment under reverse scan direction. (D) Theoretical models of perovskite with molecular surface passivation of Pb_I antisite. (Page 99)

Fig. 5.2 Investigation of the interactions between surface defects and the small molecules.

FTIR spectra of (A) pure theophylline and theophylline- PbI_2 films; (B) pure caffeine and caffeine- PbI_2 films; (C) pure theobromine and theobromine- PbI_2 films. (D) PL spectra of perovskite films without and with small molecules treatment. (E) Trap density of states (*t*DOS) in perovskite solar cells with or without small molecules treatment. (F) Nyquist plots of perovskite solar cells with or without small molecules treatment measured in the dark and at corresponding open-circuit voltages. (Page 100)

Fig. 5.3 Characterization of perovskite films and interfaces with theophylline treatment.

(A) XPS data for Pb 4f 7/2 and Pb 4f 5/2 core level spectra in perovskite films with or without theophylline treatment. (B) UPS spectra of perovskite films with or without theophylline treatment. (C) AFM and KPFM images of perovskite films with (right) or without (left) theophylline treatment. (D) Time-resolved PL spectra of perovskite films before and after depositing Spiro-OMeTAD without and with theophylline treatment. (E) Cross-section SEM images and the corresponding EBIC images and line profile of the perovskite solar cells with (right) or without (left) theophylline treatment. (Page 101)

Fig. 5.4 Enhanced photovoltaic performance and long-term stability of perovskite solar cells with theophylline treatment.

(A) Current density–voltage (J – V) curves of perovskite solar cells with or without theophylline treatment. (B) EQE curves of perovskite solar cells with or without theophylline treatment. (C) Stabilized maximum power output and the photocurrent density at maximum power point as a function of time for the best performing perovskite solar cells with or without theophylline treatment, as shown in Fig. 4A, recorded under simulated one-sun AM1.5G illumination. (D) PCE distribution of perovskite solar cells with or without theophylline treatment. (E) Evolution of the PCEs measured from the encapsulated perovskite solar cells with or without theophylline treatment exposed to continuous light ($90 \pm 10 \text{ mW cm}^{-2}$) under open-circuit condition. (Page 102)

List of Tables

Table 2.1 The summary of size and ligand density of FAPbI₃ CQDs after different number of surface treatment cycles in solution phase. (Page 50)

Acknowledgments

The dissertation and the work behind were accomplished with the generous support and supervision of many. I would like to convey my sincerest appreciation to them and my honest wish that while the dissertation has concluded our friendships continue to bloom.

First, I express my sincerest thanks to Prof. Yang Yang, my Ph.D. research advisor, for the opportunity to participate in this famous research group. His research advice of ‘always thinking as deep as you can’ has influenced me the most. During the years, I have never been lacking in inspiration, trust, and encouragement from my advisor. I have also learned from him the scientific spirits, as well as the attitude to life, which will benefit my whole life.

I also thank my committee members, Prof. Yu Huang, Prof. Richard B. Kaner, and Prof. Chong Liu, for their kindly mentorship.

I would like to thank Dr. Rui Wang for his special supports during my research. I thank Dr. Jin-Wook Lee for his kind help in my early-stage research. We had a lot of comprehensive discussions about my projects and what I have learned from him is inspiring and extremely valuable for my career. I would also like to thank Dr. Ilhan Yavuz and Ms. Selbi Nuryyeva for their help in the theoretical modeling in many of my early projects. We had uncountable discussions during these projects, which has helped me to gain deep insights into many physical models.

I will not forget to thank my senior partners in Prof. Yang’s Lab during my Ph.D. career: Dr. En-

Ping Yao, Dr. Tae-Hee Han, Dr. Dong Meng, Dr. Pengyu Sun, Dr. Nicholas De Marco, Prof. Qifeng Han, Dr. Sang-Hoon Bae, Dr. Yao-Tsung Hsieh, Dr. Wenchao Huang, Dr. Bowen Zhu, Dr. Huanjun Chen, Prof. Zhao-Kui Wang, Prof. Zhenxing Li, and Prof. Yu Duan. I also want to thank my collaborators during my Ph.D. study: Dr. Xihan Chen from NREL, Dr. Canglang Yao from U of Toledo, Ms. Yanqi Luo from UCSD, Dr. Rui Wang from Nanjing University, Dr. Kai Zhu from NREL, Dr. Chenhui Zhu from LBNL, Mr. Michael E. Liao, Prof. Mark S. Goorsky and Prof. Kendall N. Houk from UCLA, Prof. David Fenning from UCSD, Prof. Chunfeng Zhang from Nanjing University, Prof. Yanfa Yan from U of Toledo.

I am glad to have the chance to share the joys and hard times together with my fellow colleges: Dr. Zhengxu Wang, Selbi Nuryyeva, Tianyi Huang, Dr. Jiahui Zhu, Dr. Minhuan Wang, Shaun Tan, Yepin Zhao, Dr. Jun Yuan, Hao-Cheng Wang, Dr. Quantan Wu, Dr. Haowen Cheng, Zhiyu Zhao, Ran Zheng, and Yuan Zhu. I wish them best for their life and career.

At last, I thank my parents, my grandparents and my other family members. I would not have reached this step without their belief in me.

Chapter 1 is a version of *Nat. Rev. Mater.* **2020**, 10.1038/s41578-020-0221-1; Chapter 2 is a version of *Joule*, **2018**, 2, 1866-1878. Chapter 3 is a version of *Adv. Mater.* **2019**, 31, 1900111. Chapter 4 is a version of *J. Am. Chem. Soc.*, **2019**, 141, 35, 13948; Chapter 5 is a version of *Science*, **2019**, 366, 1509. All the permissions have been granted by the publishers.

VITA

- 2012-2016 Bachelor's degree. Chemistry and Chemical Engineering, Nanjing University, Nanjing, China
- 2016-2020 Graduate Student Researcher, Department of Materials Science and Engineering, University of California, Los Angeles, CA, USA

Selected Publications

1. Jingjing Xue, Rui Wang, Yang Yang*, The surface of metal halide perovskites from nano to bulk, *Nat. Rev. Mater.* 2020, 10.1038/s41578-020-0221-1.
2. Jingjing Xue†, Jin-Wook Lee†, Zhenghong Dai, Rui Wang, Selbi Nuryyeva, Michael E. Liao, Sheng-Yung Chang, Lei Meng, Dong Meng, Pengyu Sun, Oliver Lin, Mark S. Goorsky, Yang Yang*, Surface Ligand Management for Stable FAPbI₃ Perovskite Quantum Dot Solar Cells, *Joule*, 2018, 2, 1866-1878. (†Equal contributions)
3. Jingjing Xue†, Rui Wang†, Lan Chen, Selbi Nuryyeva, Tae-Hee Han, Tianyi Huang, Shaun Tan, Jiahui Zhu, Minhuan Wang, Zhao-Kui Wang, Chunfeng Zhang, Jin-Wook Lee*, Yang Yang*, Small Molecule 'Charge Driver' Enables Perovskite Quantum Dot Solar Cells with Efficiency Approaching 13%, *Adv. Mater.* 2019, 31, 1900111. (†Equal contributions)
4. Jingjing Xue†, Rui Wang†, Kai-Li Wang†, Zhao-Kui Wang, Ilhan Yavuz*, Yang Wang, Yingguo Yang, Xingyu Gao, Tianyi Huang, Selbi Nuryyeva, Jin-Wook Lee, Yu Duan, Liang-Sheng Liao*, Richard Kaner and Yang Yang*, Crystalline Liquid-like Behavior: Surface-Induced Secondary Grain Growth of Photovoltaic Perovskite Thin Film, *J. Am.*

Chem. Soc. 2019, 141, 13948-13953. (†Equal contributions)

5. Rui Wang†, Jingjing Xue†*, Kai-Li Wang†, Zhao-Kui Wang*, Yanqi Luo, David Fenning, Guangwei Xu, Selbi Nuryyeva, Tianyi Huang, Yepin Zhao, Jonathan Lee Yang, Jiahui Zhu, Minhuan Wang, Shaun Tan, Ilhan Yavuz*, Kendall N. Houk* and Yang Yang*, Constructive molecular configurations for surface-defect passivation of perovskite photovoltaics, *Science* (2019). (†Equal contributions)
6. Rui Wang†, Jingjing Xue†, Lei Meng, Jin-Wook Lee, Zipeng Zhao, Pengyu Sun, Le Cai, Tianyi Huang, Zhengxu Wang, Zhao-Kui Wang, Yu Duan, Johnathon Lee Yang, Shaun Tan, Yonghai Yuan, Yu Huang, Yang Yang, Caffeine Improves the Performance and Thermal Stability of Perovskite Solar Cells, *Joule* (2019). (†Equal contributions)
7. Tae-Hee Han†, Shaun Tan†, Jingjing Xue†, Lei Meng†, Jin-Wook Lee* and Yang Yang*, Interface and Defect Engineering for Metal Halide Perovskite Optoelectronic Devices, *Adv. Mater.* 2019, 1803515. (†Equal contributions)
8. Zhenxing Li†*, Rui Wang†, Jingjing Xue†, Xiaofei Xing, Chengcheng Yu, Tianyi Huang, Junmei Chu, Kai-li Wang, Chong Dong, Zhiting Wei, Yepin Zhao, Zhao-Kui Wang*, Yang Yang*, Core-Shell ZnO@ SnO₂ Nanoparticles for Efficient Inorganic Perovskite Solar Cells, *J. Am. Chem. Soc.* 2019, 141, 17610-17616. (†Equal contributions)

Chapter 1 Introduction to the surface features of halide perovskites

The surface of a semiconductor is where the periodic structure of the crystal lattice is terminated, accompanied by reconstruction of the atomic structure owing to surface-energy minimization. Interruption of the periodicity, either intrinsically or extrinsically, generates surface-specific states that deviate from those in the bulk crystal^{1,2}. These states substantially affect the performance of semiconductor microelectronic devices, motivating intensive research towards understanding the surface science of semiconductors. A new class of semiconductors, metal halide perovskites (MHPs), has emerged in the past decade to prevail in the optoelectronics landscape³⁻⁵. Exploiting the exceptional optical and electronic properties of these materials has led to the remarkably rapid development of MHP-based devices. MHP-based photovoltaic cells with power conversion efficiencies (PCEs) of >25% and light-emitting diodes (LEDs) with external quantum efficiencies of >20% were developed within a decade⁶⁻⁹. The general chemical formula of MHPs is ABX_3 , where A^+ is a monovalent cation, such as methylammonium (MA^+), formamidinium (FA^+) or cesium (Cs^+); B^{2+} is a divalent cation, such as Pb^{2+} or Sn^{2+} ; and X^- is a halide anion. Compared with classical perovskite oxides, the larger and more polarizable ionic components, as well as the lower charge on the X-site, result in weaker coulombic interactions and softer ionic bonding within MHPs. These softer interactions produce a mobile and sensitive surface that facilitates atomic reconstruction and irregularities. Various combinations of ions can occupy the three sites, governed by the geometrical Goldschmidt tolerance factor (for close-packed ions), giving rise to compositional tunability. Mixed-ion occupation is allowed for each site, further extending the tunability of the chemical composition. The structural susceptibility and compositional variability give rise to the intricate surface behavior of MHPs, making the role of the surface more pronounced in affecting the materials properties and device performance. Lattice discontinuities and

perturbation of the periodicity of chemical bonds, intrinsically or by external stimuli, at the surface of MHPs, creates electronic states specific to the surface that can have a substantial effect on the band structure and electron behavior. Moreover, the structural disorder at the surface is generally metastable, intensifying degradation pathways of the materials and devices^{10,11}.

As the surface-to-volume ratio scales inversely with the linear dimensions, surface effects intensify as the particle size shrinks and eventually become dominant in quantum dots (QDs), which are a few nanometers in size. The large contribution from the surface means that the properties of semiconductor QDs are significantly influenced by the surface features¹². Nevertheless, their unique ‘defect tolerance’ (discussed below) enables MHP QDs to be highly emissive, even without a second surface capping material to form the core–shell structure that is widely adopted in conventional QDs. However, most of the photoluminescence quantum yields (PLQYs) reported are only ‘close’ to unity, indicating that MHPs are defect tolerant rather than entirely defect free¹³. This finding further emphasizes the significance of the surface in enhancing the optical properties of MHP QDs, especially in optoelectronic applications for which the surface ligand chemistry needs to be adjusted to provide a benign environment for charge-carrier transport¹⁴. As the length scale increases to micrometers, the regime reaches that of bulk films, upon which the most efficient MHP photovoltaic devices to date are based. The unremitting efforts to establish sophisticated processing techniques have culminated in high-quality MHP thin films with monolayered polycrystalline grains or even single crystals^{15–17}. Considering the vertical direction of carrier transport in photovoltaic and LED devices, the surface imperfections are now the primary obstacle in limiting the carrier dynamics and, thus, device performance. Most of the recently reported high-efficiency perovskite optoelectronic devices have been enabled by surface-treatment techniques^{7,9,15,17–19},

signifying the crucial role of surfaces in the most advanced perovskite devices. Taking advantage of the defect tolerance of MHPs, high-performance MHP devices have been achieved at an early stage; however, the impossibility of defect-free MHPs, according to the maximum entropy principle²⁰, has brought the study of MHP surfaces to the forefront.

1.1 Surface terminations and disorders

The 3D crystal structure of MHPs consists of corner-sharing $[BX_6]^{2-}$ octahedra with an A-site cation occupying the central void. When the atomic periodicity is interrupted, the crystal surface can terminate with either metal halide units or organic cations. As the majority of surfaces are metastable and MHPs possess a particularly weak ionic bonding character, the surface terminations of MHPs are highly dependent on their synthesis and/or processing history. Different surface terminations are associated with different surface properties, which in turn impart the character of the entire material and the device behavior. Hence, for the development of more efficient devices, it is prerequisite to have a comprehensive understanding of the atomic structure of the surface terminations and to establish surface structure–property relationships.

In terms of lowest energy configurations, the (001) and (110) surfaces of $MAPbI_3$ are generally considered to be energetically favourable^{21,22}. Three representative surface terminations on a (001) surface are MAI, PbI_2 flat and vacant²¹ (Fig. 1.1a). Focusing on the (001) surface, PbI_2 flat termination is less thermodynamically stable than MAI termination²³. Theoretical analysis of the surface grand potentials of various surface terminations of PbI_x polyhedra found that vacant and PbI_2 flat terminations coexist on the energetically favourable (110) and (001) surfaces²⁴. Nevertheless, under the thermodynamic equilibrium conditions of bulk $MAPbI_3$, a vacant

termination is generally more stable than PbI_2 flat terminations on all surfaces^{24,25}. Similar thermodynamic energetics were observed for the MABr -terminated (001) surface of MAPbBr_3 (refs^{26,27}).

Considering the two dipole orientations of polar ammonium cations at a surface, a lower surface energy is achieved when the dipoles point into the inorganic layer²⁶. By starting from a cubic geometry and allowing the MAPbI_3 bulk cell to relax, insight into the (001) surface of a pseudocubic structure was obtained using molecular dynamics simulations. The surface relaxation was driven by competition between contraction of the inorganic cage on the PbI_2 flat (001) surface, maximization of the hydrogen bonding between MA^+ and the bridging I^- ions, and the dipole alignment of the MA^+ cations²⁸. Owing to the weak binding of the ionic lattice and the dynamic rotation of the organic cations, the surface terminations of MHPs do not have a fixed composition or structure, particularly nonstoichiometric MHP surfaces with various types of structural disorder, which trigger more intricate surface reconstruction.

As in the bulk, there are three types of intrinsic point defects that are likely to exist at the surface of MHPs, namely interstitial defects, antisite defects and vacancies²⁹⁻³¹. Overall, 12 point defects can be present at a MHP surface (Fig. 1.1b). Theoretical analysis of the unusual defect physics in MAPbI_3 suggests that the dominant point defects create only shallow trap states, whereas the remaining point defects that are likely to create deep-trap states have high formation energies, which is regarded as the origin of the defect tolerance in MHPs^{30,32}. However, when these defects are present on the surface, their energetics can become more complicated and might deviate from those in the bulk. The chemical environment around a defect on the surface differs from that in the

bulk owing to variations in the surface terminations, the chemical conditions and the undercoordinated sites with reduced steric hindrance. The relationship between surface defect formation and the surface chemical conditions has been investigated in MAPbI₃ (ref.²⁰). It was suggested that different types of defects are dominant on the surface, depending on the chemical conditions, that is, different surface terminations form under I-rich, Pb-rich or moderate (thermodynamic equilibrium with the bulk MAPbI₃) conditions. The formation energies of carrier-trapping surface defects are generally higher under Pb-rich conditions than under I-rich conditions, indicating the superiority of the Pb-rich over the I-rich environment. Under the moderate condition, all surface point defects except Pb vacancies, which are shallow carrier-trapping states, show high formation energies, suggesting that this condition might be advantageous to reduce the number of detrimental trap states on the surface²¹.

Interest in MHPs based on FA⁺ is growing owing to the possibility of achieving higher PCEs. Theoretical modelling indicates that, compared with MA⁺-related defects in bulk MAPbI₃, FA⁺-related defects in FAPbI₃ form more readily owing to weaker van der Waals interactions between the FA⁺ cations and [PbI₆]²⁻ octahedra³³. This weaker binding results from the larger size and smaller molecular dipole moment of FA⁺ compared with MA⁺ (ref.³⁴). The defect formation energies in the bulk were further compared with those on the surface of FA⁺-based perovskites to investigate the dominant surface defects. With a much lower formation energy, the antisite Pb_I defect was found to more readily form on the surface than in the bulk¹⁵.

The calculation of the transition levels of charged defects on surfaces is, however, complicated by the dissipation of charges, which limits the accuracy of theoretical predictions of MHP surface

defects and increases the significance of experimental approaches to probe the atomic structure of perovskite surfaces. Distinct surface features, such as halide dimers (accompanied by unpaired halide protrusions) and zigzag patterns were experimentally observed on the surface of MAPbX_3 using scanning tunnelling microscopy (STM; Fig. 1.1c, top right). These features most likely originate from the reorientation of the surface MA^+ cations and the electrostatic interaction between the positive charge of the ammonium groups and the neighboring halides^{35–37}. Two different surface structures with stripes and armchair domains were recently observed in all-inorganic CsPbBr_3 , originating from a complex interplay between the Cs^+ cations and Br^- anions³⁸. Vacant defect clusters were also detected in MAPbBr_3 , and identified as dynamic pairs of MA^+ and halide vacancies that tend to diffuse together when moving along a specific crystallographic orientation. Ion transport on or towards the surface was assisted by these vacancy clusters³⁷, indicating that the surface disorder of MHPs is far from simple combinations of intrinsic point defects or defect pairs. Intricate defect coupling, grouping and/or reconstructions are likely to be widely present given the flexibility of the surface, with more space for geometrical reorganization than that in the bulk^{37,39,40}. Structural heterogeneity observed in bulk MHPs, such as twinning, Ruddlesden–Popper planar faults and self-organized superlattices with phase coexistence, would also affect surface structures^{41–43}. Therefore, further studies towards a more comprehensive picture of surface states are in high demand.

The metastable nature of MHP surfaces makes them susceptible to attack by foreign species, resulting in various types of extrinsic surface disorder, which contribute to the complexity of perovskite surface structures (Fig. 1.1c, bottom left). For example, under ambient atmosphere, the surfaces of MHPs suffer from the intrusion of oxygen and moisture. The photoinduced oxygen

degradation mechanism of MAPbI_3 involves the simultaneous reduction of O_2 in I^- vacancies and the formation a superoxide⁴⁴. Various surface features are observed upon exposure of a MHP to moisture, owing to the strong surface-termination dependence of the interaction with water molecules. For example, the MAI-terminated surface of MAPbI_3 undergoes rapid hydration driven by the absorption of water molecules at the Pb sites. By contrast, the PbI_2 -terminated surface was more immune to surface solvation by virtue of the moderately robust Pb–I bonds, except when the termination became defective and facilitated the hydration process^{45,46}. Water absorption on MAPbI_3 surfaces also shows polarization dependence, with absorption being more favorable on a MAI-terminated surface with $-\text{NH}_3^+$ pointing towards the surface than on a MAI-terminated surface with $-\text{CH}_3$ pointing towards the surface. By contrast, the PbI_2 -terminated surface shows the opposite dependence on the dipole orientation⁴⁷. In summary, although the MAI-terminated surface is thermodynamically more stable, the MAPbI_3 surface tends to reconstruct into a PbI_2 -terminated one, ultimately generating a hydrated species upon exposure to ambient conditions.

1.2 Surface electronic structures and properties

The atomic structure of the surface determines the distribution of surface electronic states. Theoretical simulations reveal that the electronic properties at the surface of MHPs do not significantly deviate from those of the bulk. Particularly for non-defective or vacancy-only surface terminations, the surface electronic structures largely maintain the characteristics of the bulk phase with no midgap states observed^{24–26,31}. The band structure at the surface of MAPbI_3 resembles that of the bulk form, with the valence band maximum consisting mostly of I $5p$ and Pb $6s$ orbitals, and the conduction band minimum largely derived from Pb $6p$ orbitals^{24,48,49}. Owing to the absence of strong interactions between the MA^+ cations and $[\text{PbI}_6]^{2-}$ network, the hybridized σ bonds of MA^+

are located deep within the valence band and remain without major dispersion. The strong coupling between the lone-pair Pb 6s and the I 5p orbitals raises the valence band maximum and, hence, acceptor-like defects generally end up shallower than the band edge. The high ionicity also makes the energetically dominant donor-like defects shallow-level states³¹. Consequently, defects with a low formation energy create only shallow trap states; this is interpreted as the primary origin of the so-called defect tolerance^{30,48,50,51}. However, when looking into the extraordinarily long carrier lifetime within a MHP single crystal⁵², compared with those in a polycrystalline film, the question arises as to what extent the surface electronic properties resemble the bulk properties and whether the MHP surface is indeed defect tolerant.

Disregarding the effects from surface lattice irregularities, termination-dependent variations in the band structure have been observed. In MAPbX₃, the bandgap of the PbX₂-terminated surface is slightly smaller than that of the MAX-terminated surface, owing to the emergence of surface states located just above the conduction band minimum^{24–26,53}. The surface-weighted states do not fall in the midgap of the band structure, and thus they can probably be characterized as surface resonant states rather than true surface states and could be beneficial to hole transfer^{24–26}. For MAPbBr₃, surface reconstruction and the interplay between the orientation of the organic cations and the positions of the hosting halide anions was found to lead to the formation of electronically distinct domains with ferroelectric and antiferroelectric character, and contributions from both Br⁻ and MA⁺ orbitals to the electron density on the surface³⁵. Additionally, the Rashba effect — that is, momentum-dependent band splitting as a consequence of spin-orbit coupling and inversion symmetry breaking⁵⁴ — also exhibits strong surface dependence in MHPs. In contrast to the ‘dynamic’ Rashba effect, with fluctuations on a temporal and spatial scale, reported for the bulk of

MHPs⁵⁵, a ‘static’ band-splitting effect is found on the surface and is probably due to surface structural distortions^{56,57}. The reorientation of the organic cations in the outermost layers (Fig. 1.1c, bottom centre) in MAI-terminated surfaces only marginally affects the inorganic cages but causes pyramidalization of the outermost Pb cations in PbI₂-terminated surfaces, which increases the Rashba splitting⁵⁶. The effect of MA⁺ alignment in the bulk, however, leads to stronger Rashba splitting than that on the surface. For mixed-halide CH₃NH₃Pb(Br_{1-x}Cl_x)₃ ($0 \leq x \leq 0.19$) single crystals, the Rashba effect was suppressed at the surface owing to the disorder in the MA⁺ alignment but increased in the bulk upon Cl⁻ incorporation as a result of compression of the unit cell volume and, thus, the space available for MA⁺ orientational degrees of freedom⁵⁸.

Surface structural disorder introduces specific features in the electronic energetic landscape. As evidenced using transient reflection spectroscopy, the total carrier lifetime in a polycrystalline MHP thin film is limited by the recombination at the top and bottom surfaces, indicating that many detrimental trap states are present at the surfaces despite the defect tolerance observed in the bulk⁵⁹. As the defect formation energy is highly dependent on the chemical environment^{21,60}, it is plausible that the proposed deep-level point defects of the bulk with high formation energies could form more readily on the surface owing to the altered chemical environment, engendering many non-radiative charge-recombination centres that are particular to the surface^{21,40,61}. The energetically favourable defects of the bulk that do not affect the band structure, such as vacancies, cluster on the surface and considerably raise the local work function of the perovskite surface. Additional surface electronic features could develop through, for example, the covalency-induced formation of ion dimers⁶² (Fig. 1.1c, top left) and vacancy-based doubly charged surface layers⁶³. The invasion of foreign species under ambient conditions also contributes to the distortion of the electronic

structure at the surface. The incorporation of oxygen into defect-free MAPbI₃ creates midgap trap states that originate from the unoccupied oxygen π antibonding orbital, and the occupation of I⁻ vacancies with O₂⁻ superoxide species shifts the oxygen state downwards into the valance band, indicating favourable oxygen reduction⁴⁴. The absorption of water molecules on the surface slightly increases the surface bandgap and induces more degrees of disorder in the surface structure of MHPs. External stimuli, such as incident light, also induce specific surface states in MHP thin films. Irradiation of (Cs_{0.06}MA_{0.15}FA_{0.79})Pb(Br_{0.4}I_{0.6})₃ films triggered the formation of inhomogeneous I⁻-rich perovskite domains at the surface, leading to low-bandgap emitting sites with a high local concentration of charges, ensuring radiative bimolecular processes dominate recombination⁶⁴.

1.3 Surface features of perovskite quantum dots

The surfaces of QDs are distinct from those of bulk counterparts because the ligands used in the synthesis contribute substantially to the surface structure. According to the covalent bond classification method, the surface ligands of QDs include L-type (two-electron donor ligands, which act as Lewis bases), Z-type (two-electron acceptor ligands, which act as Lewis acids) and X-type (one-electron donor ligands)^{12,65} (Fig. 1.2a). Most of the MHP QDs synthesized to date primarily rely on long-alkyl-chain ligands, the prototypical example of which is the oleylamine–oleic acid pair⁶⁶. With the ionic character of MHP QDs, the surface ligand binding falls into the binary X-type category; surfaces are typically dynamically stabilized with either an oleylammonium halide or oleylammonium oleate⁶⁷. The cation and anion bind onto the surface of MHP QDs as an ionic pair, with the ammonium cation taking the place of a surface A-cation while the halide or carboxylate attaches on the surface and maintains charge neutrality^{67–69} (the blue

structures in Fig. 1.2b). The large diffusion coefficient of surface ligands implies highly dynamic ligand binding, with fast exchange between the bound and free states, which is likely the origin of the ease of halide exchange^{39,70} and ligand loss upon purification of MHP QDs^{71–73}. This unique binary binding mode has inspired numerous new ligands for MHP QDs (Fig. 1.2b), the details of which are discussed below.

The non-unity and frequent loss of PLQY upon cyclic purification implies the existence of structural disorder at the surface of MHP QDs. Surface imperfections are more prominent in nanoparticles than in the bulk phase, owing to their larger number of surface atoms and size of a few nanometres. The small size enables bulk defects in the core of the QDs to travel towards the surface if they are more stable in this region. The energetics of surface defect formation in QDs are also expected to differ from those in the bulk, as the chemical environment of QD surface defects involves a complex interplay between lattice termination, ligands, surrounding solvent and size-induced inherent strain redistribution and symmetry breaking^{74,75}. The most plausible scenario for the formation of defects on the surface is the detachment of capping ligands to leave behind vacancies. The electronic structure evolution of $[\text{CsPbX}_3](\text{PbX}_2)_k\{\text{AX}'\}_n$ (where k and n are the numbers of PbX_2 units and $\{\text{AX}'\}$ ligands on the outermost two atomic layers, respectively) was evaluated theoretically while stripping ion pairs from the QD surface. Even when 75% of the $\{\text{AX}'\}$ units had been removed, midgap states remained absent and the structural integrity was preserved. However, such defect-tolerant behaviour no longer holds for PbX_2 -terminated $[\text{CsPbX}_3](\text{PbX}_2)_k$ or uncapped QDs, for which stripping only 25% of the surface PbX_2 units causes midgap states to appear and triggers structural deformation⁷⁶. Deeper insight into the electronic structure of surface defects in MHP QDs was recently gained through systematic theoretical

screening of interstitial, vacancy and antisite defects on the surface of CsPbBr₃ QDs⁷⁵, as has been intensively studied in the bulk. In contrast to bulk MHPs, nanoparticles capped with surface ligands are usually formed in a low dielectric solvent. Hence, ion pairs are usually responsible for the creation of the point defects, where the addition, removal or substitution of an ion on the surface has to be accompanied by a counterion to neutralize the charge. Therefore, the atomic and electronic surface features generated in nanoparticles can be distinct from those of the bulk. The defect formation energies of each type of point defect at different locations were compared (Fig. 1.2c). With the most negative defect formation energies, surface interstitial defects were determined to be energetically favoured, especially at the surface edge. Midgap states of the most stable Pb²⁺ interstitials emerged from the counterion (halide) instead of Pb²⁺ itself, and only when the halide occupies a surface position that points outwards from the surface. Although the expulsion of ions in their elemental form from the lattice would also result in midgap states, this process is strongly endothermic, which limits the formation of such surface defects. Other point defects on QD surfaces either do not create midgap states or undergo reconstruction of the configuration to give rise to non-defective structures or electronically benign defects⁷⁵.

References

1. Davison, S. G., Steshcka, M. *Basic theory of surface states*. 46-54 (Clarendon Press, 1992).
2. Shockley, W. On the surface states associated with a periodic potential. *Phys. Rev.* **56**, 317–323 (1939).
3. Kim, H. S. *et al.* Lead iodide perovskite sensitized all-solid-state submicron thin film mesoscopic solar cell with efficiency exceeding 9%. *Sci. Rep.* **2**, 591 (2012).

4. Kojima, A., Teshima, K., Shirai, Y. & Miyasaka, T. Organometal halide perovskites as visible-light sensitizers for photovoltaic cells. *J. Am. Chem. Soc.* **131**, 6050-6051 (2009).
5. Yuan, M. *et al.* Perovskite energy funnels for efficient light-emitting diodes. *Nat. Nanotechnol.* (2016).
6. NREL. Best Research-Cell Efficiency Chart. *National Renewable Energy Laboratory* <https://www.nrel.gov/pv/assets/pdfs/best-research-cell-efficiencies.20191106.pdf> (2019).
7. Xu, W. *et al.* Rational molecular passivation for high-performance perovskite light-emitting diodes. *Nat. Photonics* **13**, 418–424 (2019).
8. Cao, Y. *et al.* Perovskite light-emitting diodes based on spontaneously formed submicrometre-scale structures. *Nature* **562**, 249–253 (2018).
9. Lin, K. *et al.* Perovskite light-emitting diodes with external quantum efficiency exceeding 20 per cent. *Nature* **562**, 245–248 (2018).
10. Meggiolaro, D., Mosconi, E. & De Angelis, F. Formation of Surface Defects Dominates Ion Migration in Lead-Halide Perovskites. *ACS Energy Lett.* **4**, 779–785 (2019).
11. Wang, R. *et al.* A Review of Perovskites Solar Cell Stability. *Adv. Funct. Mater.* **29**, 1808843 (2019).
12. Boles, M. A., Ling, D., Hyeon, T. & Talapin, D. V. The surface science of nanocrystals. *Nat. Mater.* **15**, 141–153 (2016).
13. Levchuk, I. *et al.* Brightly Luminescent and Color-Tunable Formamidinium Lead Halide Perovskite FAPbX_3 (X = Cl, Br, I) Colloidal Nanocrystals. *Nano Lett.* **17**, 2765–2770 (2017).
14. Kagan, C. R. & Murray, C. B. Charge transport in strongly coupled quantum dot solids. *Nat. Nanotechnol.* **10**, 1013–1026 (2015).

15. Wang, R. *et al.* Constructive molecular configurations for surface-defect passivation of perovskite photovoltaics. *Science* **366**, 1509–1513 (2019).
16. Chen, Z. *et al.* Thin single crystal perovskite solar cells to harvest below-bandgap light absorption. *Nat. Commun.* **8**, 1890 (2017).
17. Min, H. *et al.* Efficient, stable solar cells by using inherent bandgap of a-phase formamidinium lead iodide. *Science* **366**, 749-753 (2019).
18. Jung, E. H. *et al.* Efficient, stable and scalable perovskite solar cells using poly(3-hexylthiophene). *Nature* **567**, 511–515 (2019).
19. Jiang, Q. *et al.* Surface passivation of perovskite film for efficient solar cells. *Nat. Photonics* **13**, 460–466 (2019).
20. Callen, H. *et al.* *Thermodynamics and an Introduction to Thermostatistics* 27-35 (Wiley, 1985)
21. Uratani, H. & Yamashita, K. Charge Carrier Trapping at Surface Defects of Perovskite Solar Cell Absorbers: A First-Principles Study. *J. Phys. Chem. Lett.* **8**, 742-746 (2017).
22. Mosconi, E., Ronca, E. & De Angelis, F. First-principles investigation of the TiO₂/organohalide perovskites interface: The role of interfacial chlorine. *J. Phys. Chem. Lett.* **5**, 2619–2625 (2014).
23. Quarti, C., De Angelis, F. & Beljonne, D. Influence of Surface Termination on the Energy Level Alignment at the CH₃NH₃PbI₃ Perovskite/C60 Interface. *Chem. Mater.* **29**, 958–968 (2017).
24. Haruyama, J., Sodeyama, K., Han, L. & Tateyama, Y. Termination dependence of tetragonal CH₃NH₃PbI₃ surfaces for perovskite solar cells. *J. Phys. Chem. Lett.* **5**, 2903–2909 (2014).

25. Haruyama, J., Sodeyama, K., Han, L. & Tateyama, Y. Surface Properties of $\text{CH}_3\text{NH}_3\text{PbI}_3$ for Perovskite Solar Cells. *Accounts of Chemical Research* **49**, 554–561 (2016).
26. Huang, X., Paudel, T. R., Dowben, P. A., Dong, S. & Tsymbal, E. Y. Electronic structure and stability of the $\text{CH}_3\text{NH}_3\text{PbBr}_3$ (001) surface. *Phys. Rev. B* **94**, 195309 (2016).
27. Komesu, T. *et al.* Surface Electronic Structure of Hybrid Organo Lead Bromide Perovskite Single Crystals. *J. Phys. Chem. C* **120**, 21710–21715 (2016).
28. Torres, A. & Rego, L. G. C. Surface effects and adsorption of methoxy anchors on hybrid lead iodide perovskites: Insights for spiro-MeOTAD attachment. *J. Phys. Chem. C* **118**, 26947–26954 (2014).
29. Ran, C., Xu, J., Gao, W., Huang, C. & Dou, S. Defects in metal triiodide perovskite materials towards high-performance solar cells: Origin, impact, characterization, and engineering. *Chem. Soc. Rev.* **47**, 4581-4610 (2018).
30. Yin, W.-J., Shi, T. & Yan, Y. Unusual defect physics in $\text{CH}_3\text{NH}_3\text{PbI}_3$ perovskite solar cell absorber. *Appl. Phys. Lett.* **104**, 63903 (2014).
31. Liu, Y. *et al.* Atomistic Origins of Surface Defects in $\text{CH}_3\text{NH}_3\text{PbBr}_3$ Perovskite and Their Electronic Structures. *ACS Nano* **11**, 2060–2065 (2017).
32. Kim, J., Lee, S. H., Lee, J. H. & Hong, K. H. The role of intrinsic defects in methylammonium lead iodide perovskite. *J. Phys. Chem. Lett.* **5**, 1312-1317 (2014).
33. Liu, N. & Yam, C. Y. First-principles study of intrinsic defects in formamidinium lead triiodide perovskite solar cell absorbers. *Phys. Chem. Chem. Phys.* **20**, 6800-6804 (2018).
34. Kabakova, I. V. *et al.* The effect of ionic composition on acoustic phonon speeds in hybrid perovskites from Brillouin spectroscopy and density functional theory. *J. Mater. Chem. C* **6**, 3861-3868 (2018).

35. Ohmann, R. *et al.* Real-Space Imaging of the Atomic Structure of Organic-Inorganic Perovskite. *J. Am. Chem. Soc.* **137**, 16049–16054 (2015).
36. She, L., Liu, M. & Zhong, D. Atomic structures of CH₃NH₃PbI₃ (001) surfaces. *ACS Nano* **10**, 1126–1131 (2016).
37. Stecker, C. *et al.* Surface defect dynamics in organic-inorganic hybrid perovskites: From mechanism to interfacial properties. *ACS Nano* **13**, 12127–12136 (2019).
38. Hieulle, J. *et al.* Imaging of the Atomic Structure of All-Inorganic Halide Perovskites. *J. Phys. Chem. Lett.* **11**, 818–823 (2020).
39. Akkerman, Q. A. *et al.* Tuning the optical properties of cesium lead halide perovskite nanocrystals by anion exchange reactions. *J. Am. Chem. Soc.* **137**, 10276–10281 (2015).
40. Meggiolaro, D., Mosconi, E. & De Angelis, F. Modeling the Interaction of Molecular Iodine with MAPbI₃: A Probe of Lead-Halide Perovskites Defect Chemistry. *ACS Energy Lett.* **3**, 447–451 (2018).
41. Thind, A. S. *et al.* Atomic Structure and Electrical Activity of Grain Boundaries and Ruddlesden–Popper Faults in Cesium Lead Bromide Perovskite. *Adv. Mater.* **31**, 1805047 (2019).
42. Rothmann, M. U. *et al.* Direct observation of intrinsic twin domains in tetragonal CH₃NH₃PbI₃. *Nat. Commun.* **8**, 14547 (2017).
43. Kim, T. W. *et al.* Self-Organized Superlattice and Phase Coexistence inside Thin Film Organometal Halide Perovskite. *Adv. Mater.* **30**, 1705230 (2018).
44. Aristidou, N. *et al.* Fast oxygen diffusion and iodide defects mediate oxygen-induced degradation of perovskite solar cells. *Nat. Commun.* **8**, 15218 (2017).

45. Zhang, L., Ju, M. G. & Liang, W. The effect of moisture on the structures and properties of lead halide perovskites: A first-principles theoretical investigation. *Phys. Chem. Chem. Phys.* **18**, 23174–23183 (2016).
46. Mosconi, E., Azpiroz, J. M. & De Angelis, F. Ab Initio Molecular Dynamics Simulations of Methylammonium Lead Iodide Perovskite Degradation by Water. *Chem. Mater.* **27**, 4885–4892 (2015).
47. Koocher, N. Z., Saldana-Greco, D., Wang, F., Liu, S. & Rappe, A. M. Polarization Dependence of Water Adsorption to $\text{CH}_3\text{NH}_3\text{PbI}_3$ (001) Surfaces. *J. Phys. Chem. Lett.* **6**, 4371–4378 (2015).
48. Yin, W. J., Yang, J. H., Kang, J., Yan, Y. & Wei, S. H. Halide perovskite materials for solar cells: A theoretical review. *J. Mater. Chem. A* **3**, 8926–8942 (2015).
49. Schulz, P., Cahen, D. & Kahn, A. Halide Perovskites: Is It All about the Interfaces? *Chemical Reviews* **119**, 3349–3417 (2019).
50. Xiao, Z., Song, Z. & Yan, Y. From Lead Halide Perovskites to Lead-Free Metal Halide Perovskites and Perovskite Derivatives. *Advanced Materials* **31**, 1803792 (2019).
51. Brandt, R. E. *et al.* Searching for ‘defect-Tolerant’ Photovoltaic Materials: Combined Theoretical and Experimental Screening. *Chem. Mater.* **29**, 4667–4674 (2017).
52. Cheng, X., Yang, S., Cao, B., Tao, X. & Chen, Z. Single Crystal Perovskite Solar Cells: Development and Perspectives. *Adv. Funct. Mater.* **30**, 1905021 (2019).
53. Geng, W. *et al.* Effect of surface composition on electronic properties of methylammonium lead iodide perovskite. *J. Mater.* **1**, 213–220 (2015).
54. Stranks, S. D. & Plochocka, P. The influence of the Rashba effect. *Nat. Mater.* **17**, 381–382 (2018).

55. Etienne, T., Mosconi, E. & De Angelis, F. Dynamical Origin of the Rashba Effect in Organohalide Lead Perovskites: A Key to Suppressed Carrier Recombination in Perovskite Solar Cells? *J. Phys. Chem. Lett.* **7**, 1638–1645 (2016).
56. Mosconi, E., Etienne, T. & De Angelis, F. Rashba Band Splitting in Organohalide Lead Perovskites: Bulk and Surface Effects. *Journal of Physical Chemistry Letters* **8**, 2247–2252 (2017).
57. Niesner, D. *et al.* Giant Rashba Splitting in $\text{CH}_3\text{NH}_3\text{PbBr}_3$ Organic-Inorganic Perovskite. *Phys. Rev. Lett.* **117**, 126401 (2016).
58. Li, Z. *et al.* Optoelectronic Dichotomy of Mixed Halide $\text{CH}_3\text{NH}_3\text{Pb}(\text{Br}_{1-x}\text{Cl}_x)_3$ Single Crystals: Surface versus Bulk Photoluminescence. *J. Am. Chem. Soc.* **140**, 11811–11819 (2018).
59. Yang, Y. *et al.* Top and bottom surfaces limit carrier lifetime in lead iodide perovskite films. *Nat. Energy* **2**, 16207 (2017).
60. Yu, Z. L., Ma, Q. R., Zhao, Y. Q., Liu, B. & Cai, M. Q. Surface Termination - A Key Factor to Influence Electronic and Optical Properties of CsSnI_3 . *J. Phys. Chem. C* **122**, 9275–9282 (2018).
61. Chen, B., Rudd, P. N., Yang, S., Yuan, Y. & Huang, J. Imperfections and their passivation in halide perovskite solar cells. *Chem. Soc. Rev.* **48**, 3842-3867 (2019).
62. Agiorgousis, M. L., Sun, Y. Y., Zeng, H. & Zhang, S. Strong covalency-induced recombination centers in perovskite solar cell material $\text{CH}_3\text{NH}_3\text{PbI}_3$. *J. Am. Chem. Soc.* **136**, 14570–14575 (2014).
63. Sarmah, S. P. *et al.* Double Charged Surface Layers in Lead Halide Perovskite Crystals. *Nano Lett.* **17**, 2021–2027 (2017).

64. Andaji-Garmaroudi, Z. *et al.* A Highly Emissive Surface Layer in Mixed-Halide Multication Perovskites. *Adv. Mater.* **31**, 1902374 (2019).
65. Anderson, N. C., Hendricks, M. P., Choi, J. J. & Owen, J. S. Ligand exchange and the stoichiometry of metal chalcogenide nanocrystals: Spectroscopic observation of facile metal-carboxylate displacement and binding. *J. Am. Chem. Soc.* **135**, 18536–18548 (2013).
66. Akkerman, Q. A., Rainò, G., Kovalenko, M. V. & Manna, L. Genesis, challenges and opportunities for colloidal lead halide perovskite nanocrystals. *Nat. Mater.* **17**, 394–405 (2018).
67. De Roo, J. *et al.* Highly Dynamic Ligand Binding and Light Absorption Coefficient of Cesium Lead Bromide Perovskite Nanocrystals. *ACS Nano* **10**, 2071–2081 (2016).
68. Ravi, V. K. *et al.* Origin of the Substitution Mechanism for the Binding of Organic Ligands on the Surface of CsPbBr₃ Perovskite Nanocubes. *J. Phys. Chem. Lett.* **8**, 4988–4994 (2017).
69. Almeida, G. *et al.* Role of Acid-Base Equilibria in the Size, Shape, and Phase Control of Cesium Lead Bromide Nanocrystals. *ACS Nano* **12**, 1704–1711 (2018).
70. Nedelcu, G. *et al.* Fast Anion-Exchange in Highly Luminescent Nanocrystals of Cesium Lead Halide Perovskites (CsPbX₃, X = Cl, Br, I). *Nano Lett.* **15**, 5635–5640 (2015).
71. Li, J. *et al.* 50-Fold EQE Improvement up to 6.27% of Solution-Processed All-Inorganic Perovskite CsPbBr₃ QLEDs via Surface Ligand Density Control. *Adv. Mater.* **29**, 1603885 (2017).
72. Pan, A. *et al.* Insight into the Ligand-Mediated Synthesis of Colloidal CsPbBr₃ Perovskite Nanocrystals: The Role of Organic Acid, Base, and Cesium Precursors. *ACS Nano* **10**, 7943–7954 (2016).

73. Ten Brinck, S. & Infante, I. Surface Termination, Morphology, and Bright Photoluminescence of Cesium Lead Halide Perovskite Nanocrystals. *ACS Energy Lett.* **1**, 1266–1272 (2016).
74. Forde, A., Inerbaev, T., Hobbie, E. K. & Kilin, D. S. Excited-State Dynamics of a CsPbBr₃ Nanocrystal Terminated with Binary Ligands: Sparse Density of States with Giant Spin-Orbit Coupling Suppresses Carrier Cooling. *J. Am. Chem. Soc.* **141**, 4388–4397 (2019).
75. Ten Brinck, S., Zaccaria, F. & Infante, I. Defects in Lead Halide Perovskite Nanocrystals: Analogies and (Many) Differences with the Bulk. *ACS Energy Lett.* **4**, 2739–2747 (2019).

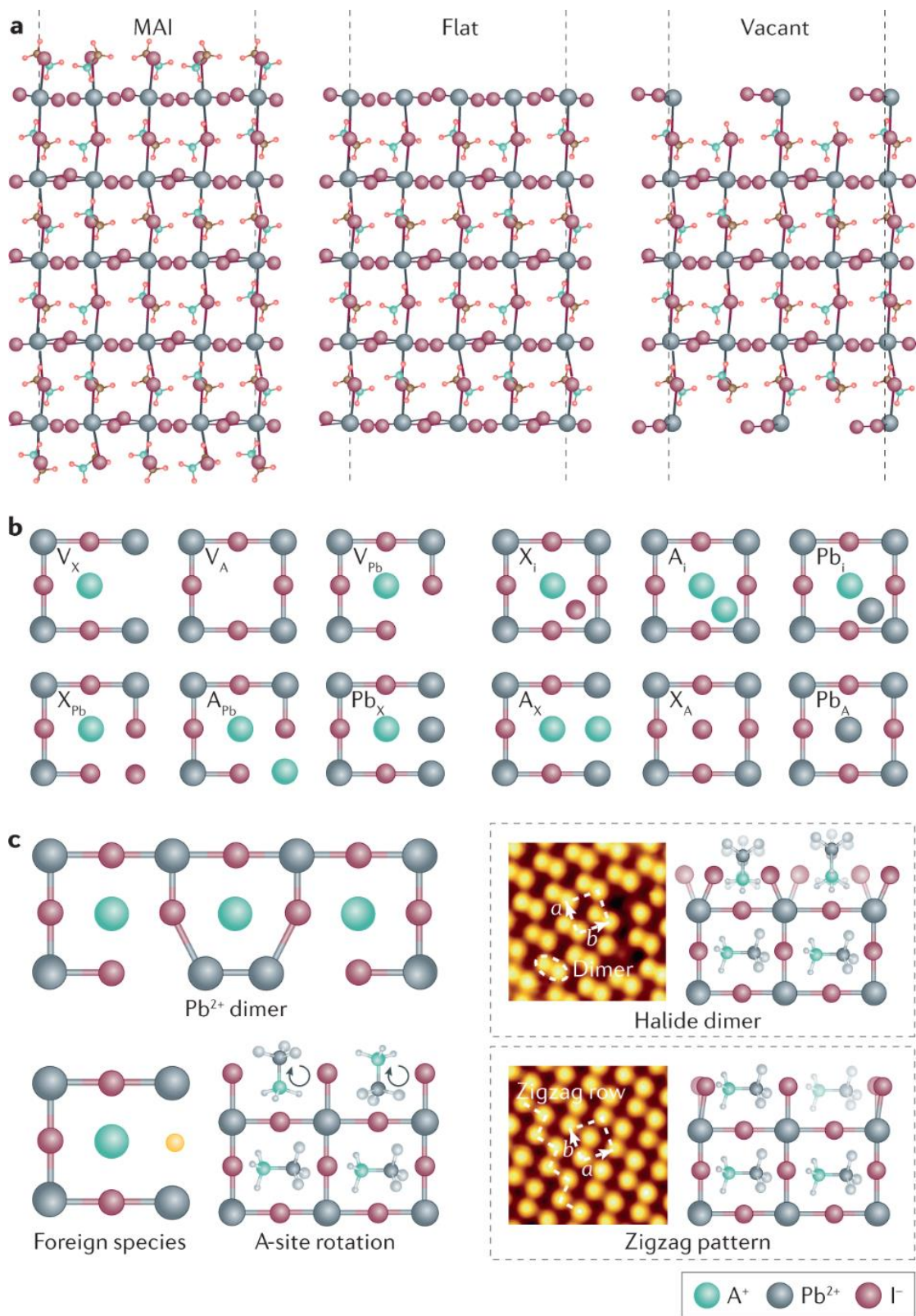


Figure 1.1 a | Side views of three representative surface terminations in MAPbI_3 (where MA^+ is methylammonium). **b** | The 12 types of native point defects found in metal halide perovskites. V_Y denotes a Y vacancy, Y_i denotes an interstitial Y-site and Y_Z denotes a Z-site substituted by Y, where Y and Z represent an ion of APbX_3 (where A^+ is a monovalent cation and X^- a halide). **c** | Other surface features of metal halide perovskites include ion dimers (Pb^{2+} dimers and halide dimers), zigzag patterns, various orientations of the organic cations and the incursion of foreign species, such as O_2 . The high-resolution scanning tunnelling microscopy images on the right show the formation of halide dimers (top) and a zigzag pattern (bottom) on the surface of MAPbI_3 . The unit cells are denoted by dashed white rectangles.

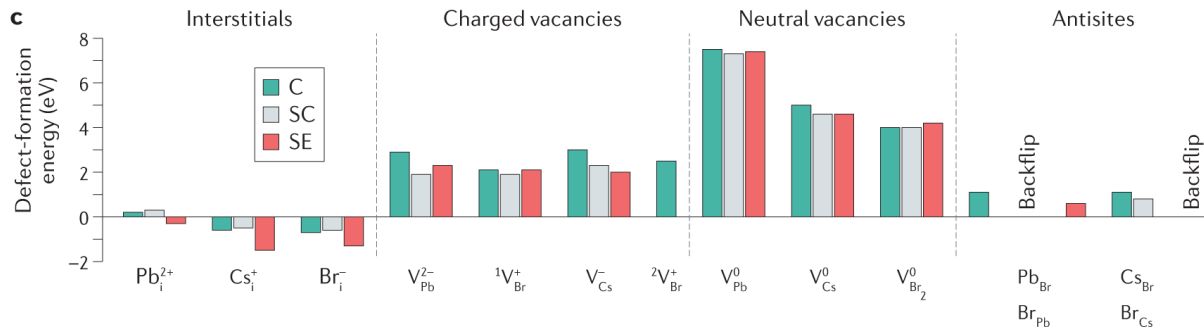
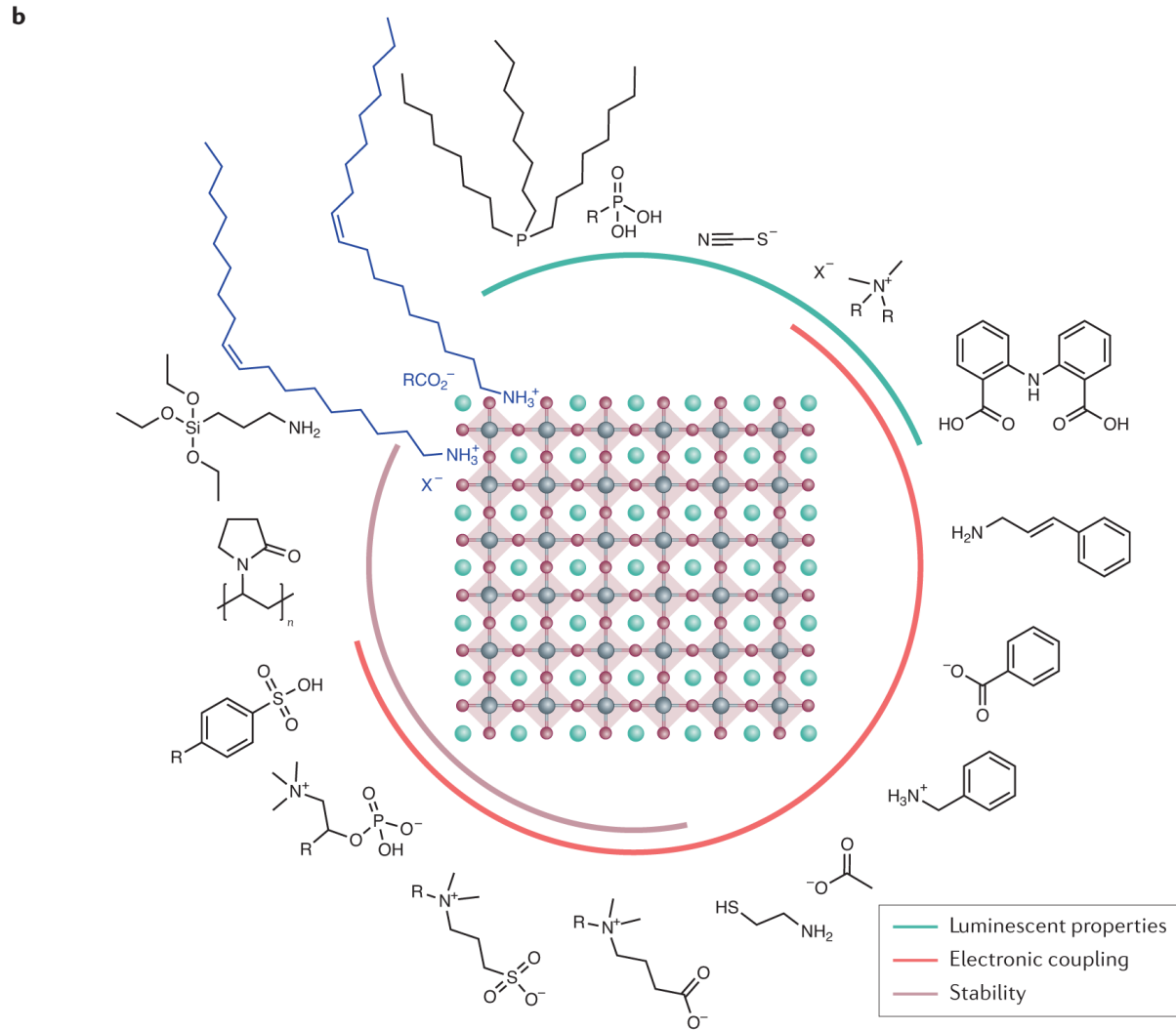
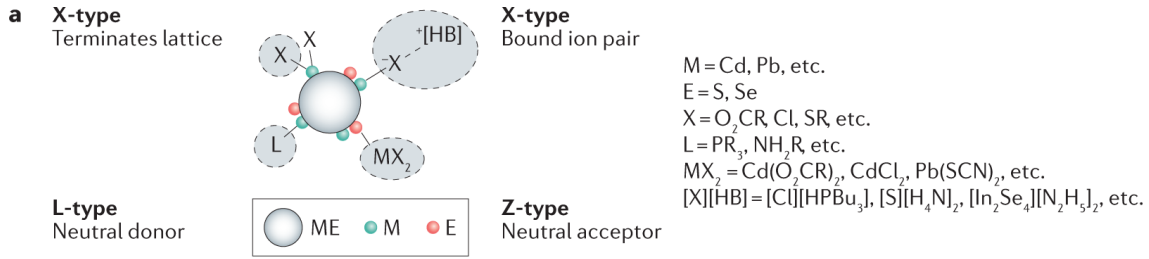


Figure 1.2 a | The various ligand-binding motifs according to the covalent-bond-classification method, illustrated here for a metal chalcogenide nanoparticle. **b** | Various ligands and surface-treatment methods have been adopted in the synthesis of perovskite nanoparticles. The ligands have been classified by their function: to improve the luminescent properties, enhance the electronic coupling or increase stability. The prototypical oleylamine–oleic acid ligand pairs used in the synthesis of metal halide perovskite quantum dots result in surface binding involving oleylammonium halide or oleylammonium oleate, as depicted in blue. **c** | Calculated defect-formation energies for interstitial, charged and neutral vacancies, and antisite substitutions on the surface of CsPbBr₃ quantum dots (where C is core, SC is surface centre and SE is surface edge). V_Y denotes a Y vacancy, Y_i denotes an interstitial Y-site and Y_Z denotes a Z-site substituted by Y, where Y and Z represent an ion of CsPbBr₃. The right superscript denotes the charge of the defect and a left superscript denotes the number of the defects considered when calculating the formation energy. Backflip means that the antisite displacement goes back to its initial non-defective configuration. Calculations were performed using density functional theory with the PBE functional.

Chapter 2 Surface Ligand Management for Stable FAPbI₃ Perovskite Quantum Dot Solar Cells

Semiconductor colloidal quantum dots (CQDs) have emerged as promising materials for next-generation photovoltaic devices owing to their unique features, such as low-temperature processability, tunable absorption, ability to design flexible devices, and multiple exciton generation (MEG).¹⁻⁴ A variety of semiconductor CQDs have been studied, such as PbS, PbSe, CdS, CdSe and CdTe, with power conversion efficiencies (PCEs) exceeding 10% achieved through development of surface chemistry.⁴⁻⁸ Recently, a new class of halide perovskite CQDs have been added to the pool of semiconductor CQDs⁹⁻¹¹ which have shown great promise when incorporated into photovoltaic devices, breaking the record PCE of CQDs photovoltaics.¹² The halide perovskite materials generally have an ABX₃ structure, where A is a monovalent organic cation or an alkali metal cation, B is a divalent cation (e.g. Pb²⁺, Sn²⁺) and X is a halide anion (e.g. Cl⁻, Br⁻, I⁻). These materials exhibit a unique combination of high absorption coefficients, long carrier diffusion lengths and small exciton binding energy, making perovskite CQDs competitive to conventional chalcogenides CQDs for efficient photovoltaic devices.¹³⁻¹⁶ Furthermore, it has been demonstrated that the enhanced contribution of surface energy in CQDs can stabilize the desirable cubic CsPbI₃ perovskite phase, which is thermodynamically unfavorable in bulk form at low temperature. This provides a new strategy of improving the stability of perovskite solar cells.⁹

The ionic bonding character of the halide perovskite materials makes them sensitive to polar solvents, resulting in accelerated degradation of perovskite CQDs upon exposure to such solvents.¹⁷⁻¹⁹ This has posed the difficulty in dealing with the long organic ligands on the surface of

as-synthesized perovskite CQDs, which are detrimental to carrier transport in CQDs solar cells. Furthermore, the relatively weak bonding of the organic cations with inorganic cages (PbI_6 octahedra) in organic-inorganic hybrid perovskite CQDs than inorganic counterparts²⁰⁻²² causes them to be even more vulnerable to polar solvents, posing greater challenges to effective treatment of the ligands. Hence, only few studies on perovskite CQDs solar cells have been reported so far, with photoactive materials limited to cesium-containing inorganic perovskite CQDs.^{9-12,23} However, the cesium-containing perovskite materials have a relatively larger bandgap (1.73 eV for CsPbI_3) and shorter carrier lifetime compared to their organic-inorganic hybrid counterparts, which limit further enhancement of PCE.^{24,25} In this regard, formamidium lead triiodide (FAPbI_3) has the most desirable bandgap (ca. 1.5 eV) among the Pb-based perovskite materials.²⁶ Furthermore, the faster formation of large polaron in the organic-inorganic hybrid perovskite than in its inorganic counterparts would make FAPbI_3 CQD more desirable than CsPbI_3 CQD in terms of charge-transporting properties.²²

Here, we introduce efficient strategies for managing the surface ligands on FAPbI_3 perovskite CQDs. Rational design of post-synthetic processes enabled effective control of ligand density. Because of the well-designed ligand control, FAPbI_3 CQDs solar cell with an initial PCE of 8.38% was demonstrated for the first time without device optimization. Furthermore, despite poor phase stability of bulk FAPbI_3 ,²⁷ the FAPbI_3 CQDs and devices showed superior ambient- and operational-stability over bulk FAPbI_3 films and devices.

2.1 Synthesis and surface ligand treatment of FAPbI_3 CQDs

FAPbI₃ CQDs were synthesized via a modified hot-injection method,²⁸ yielding a nearly cubic shaped ensemble with an average size of 17.7 ± 2.5 nm (**Figure 2.1A** and **Figure A2.1**). The synthesized FAPbI₃ CQDs were confirmed to be cubic perovskite phase with no secondary phase from X-ray diffraction (XRD) measurement in **Figure 2.1B**.²⁹ For comparison, the XRD pattern of the bulk FAPbI₃ film was compared where hexagonal non-perovskite phase (δ -phase) was observed.³⁰ The FAPbI₃ CQDs exhibited a photoluminescence (PL) emission peak and an absorption edge at around 800 nm. As a reference, we synthesized the CsPbI₃ CQDs according to the previous work,⁹ which showed a PL emission peak and absorption edge at around 690 nm (**Figure 2.1C**). The obvious red-shift of the absorption edge of FAPbI₃ CQDs (1.55 eV) compared to that of CsPbI₃ CQDs (1.80 eV) indicates a more desirable bandgap for photovoltaics. The time-resolved PL decay profile of FAPbI₃ CQDs exhibited nearly biexponential decay characteristics (**Table B2.1**) with average relaxation time of 70.9 ns (**Figure 2.1D**), which is more than an order of magnitude longer than that of CsPbI₃ CQDs (2.7 ns). This is indicative of longer carrier lifetime and thus demonstrates the potential of achieving high efficiency CQDs solar cells with the FAPbI₃ CQDs.

The as-synthesized FAPbI₃ CQDs were capped with oleic acid and oleylamine, which act as surface ligands that are necessary to maintain good dispersion. However, these long insulating ligands are detrimental to efficient charge carrier transport because they introduce large potential barrier that prevents electrical coupling between the CQDs.³¹ Therefore, dealing with the surface ligands becomes the prerequisite to constructing efficient photovoltaic devices based on perovskite CQDs. Upon synthesis, the surface of perovskite CQDs is reported to be terminated by oleylammonium halide and oleylammonium carboxylates, which are ionically bonded to the perovskite surface.³²

Such ionic nature of the ligand binding causes ligands to be highly loose and easy to completely desorb once attacked by any polar solvents. Hence, it results in the difficulty to retain the colloidal integrity during the surface treatment.^{17,33} Also, the ionic binding character of perovskite lattice, as well as, the organic component FA⁺ make it more challenging to retain perovskite structural integrity in highly polar solvents because of its weaker bonding with surrounding PbI₆ cages than inorganic counterparts evidenced by relatively poor thermal stability and higher degree of rotational motion.¹⁷ Furthermore, relatively poor phase stability of FAPbI₃ compared with other organic-inorganic hybrid perovskites, as observed in their bulk form, would require more delicate post-synthetic processes. As a result, no traditional surface treatment technique can be applied because they involve highly polar solvents such as methanol and acetone. These factors motivated us to design a customized surface treatment for FAPbI₃ perovskite CQDs.^{34,35}

In order to design a rational surface treatment process, we classified the solvents into three grades by their polarity (**Figure 2.2**). The highly polar solvents bearing the strongest dipoles are in the ‘Grade I’, in which ionic bonds in FAPbI₃ can be completely destroyed (**Figure 2.2**). On the other end, solvents with too low polarity (Grade III) will not be able to break the bond between the ligand and FAPbI₃.³⁴ To effectively handle the surface ligands without destroying CQDs, proper antisolvents with moderate polarity (Grade II) should be employed. A series of commonly used solvents with different polarity were tested (listed in **Table B2.2**). As a result, water, methanol, ethanol, isopropanol were classified as ‘Grade I’ solvents that would cause immediate degradation of FAPbI₃ CQDs once added; chlorobenzene, toluene, octane, and hexane were classified as ‘Grade III’ solvents that are not able to remove the ligands. By avoiding ‘Grade I’ and ‘Grade III’ solvents, a novel surface treatment method was successfully developed, where the ligand density was

sequentially decreased in solution and in solid phase, while the integrity of FAPbI₃ CQDs was maintained. This was achieved by employing a set of ‘Grade II’ solvents with gradually reduced polarity in surface treatment cycle.

Our surface treatment process consists of three cycles. As shown in **Figure 2.2A** (left), the first two cycles of surface treatment processes are in solution phase. In the first cycle, 2-pentanol was used as an antisolvent. Compared to commonly used antisolvents such as methanol, ethanol and propanol, 2-pentanol has relatively longer alkyl chain with stronger electron-donating effect that can reduce the dipole of C-O bond and, thus, the polarity of the solvent.³⁶ Additionally, 2-pentanol is a protic solvent, which can assist in keeping FA⁺ protonated in FAPbI₃ CQDs so as to maintain the ionic lattice structure of perovskite. t-Butanol was also tested and was found to induce flocculation of FAPbI₃ CQDs without destroying them. However, the long-term stability of these CQDs was found to be poor, undergoing degradation within 12 hours. Since the polarity indexes of t-butanol and 2-pentanol are similar, we further consider dimensions of component compatibility using Hansen model. If the Hansen distances of PbI₂ (one of the precursors of perovskite) and a chosen antisolvent are very similar, it indicates that such antisolvent will easily dissolve PbI₂ and, thus, cause the degradation of perovskite lattice. In the case of 2-pentanol and t-butanol, the Hansen parameters are as following: $\delta D=15.8$, $\delta P=5.7$, $\delta H=14.5$ for t-butanol; and $\delta D=15.6$, $\delta P=6.4$, $\delta H=13.3$ for 2-pentanol. where δD , δP and δH are dispersion, polar and hydrogen-bonding parameters, respectively.³⁷ Since Hansen parameters of lead salts are unknown, we made an assumption, as suggested in the literature, that their position on the three dimensional Hansen graph is somewhere between the positions of DMF and DMSO because both these solvents dissolve PbI₂ very well.^{38,39} In this case, t-butanol shows shorter distance to the assumed Hansen parameters of

PbI₂, indicating a stronger interaction of the t-butanol with PbI₂ than that of the 2-pentanol, which might lead to a faster degradation of perovskite lattice. As the dispersion and polar components of the two solvents are similar, the stronger hydrogen-bonding between t-butanol and lead salts might play a more important role. Interestingly, the FAPbI₃ CQDs get destroyed if 2-pentanol is used again in the second cycle of surface treatment. This might be due to the lower ligand density on the surface of FAPbI₃ CQDs, which exposed more perovskite ionic lattice to the antisolvent. Hence, the CQDs could not ‘tolerate’ the polarity of 2-pentanol anymore. In order to maintain the integrity of perovskite CQDs in the second cycle of surface treatment, a different ‘Grade II’ antisolvent with slightly lower polarity should be used. Mixed solvent of acetonitrile/toluene is well known for its adjustable polarity by varying the volume ratio of acetonitrile and toluene. By rational control of its polarity, acetonitrile/toluene (**Table B2.2**) was used in the second cycle of surface treatment to further decrease the ligand density on the surface of FAPbI₃ CQDs. The gradual reduction of the surface ligand density was monitored by nuclear magnetic resonance (NMR). As shown in **Figure 2.2A**, the total concentration of oleyl species (determined by the resonance of hydrogen atoms on a double bond) gradually reduced with increasing cycles of surface treatment. After the first cycle of surface treatment, strong resonance signals from octadecene (ODE) and oleyl species (at around 5.3 ppm)⁴⁰ were still detected, while after second cycle of surface treatment, these signals became negligible, indicating an effective removal of ligands from the surface. The ligand density, defined as the concentration of oleyl species on a unit surface area of CQDs, was calculated (**Table 2.1**) to be 3.6, 2.0, and 1.2 a.u./cm² after 0-cycle (as-synthesized CQDs), 1-cycle, and 2-cycle surface treatment, respectively, by the combination of inductively coupled plasma atomic absorption spectroscopy (ICP-AES), NMR and TEM measurements (**Figure A2.2**).^{40,41} After two cycles of surface treatment in solution phase, majority of excess ligands were removed, while a small amount

of ligands remained to maintain the colloidal integrity of FAPbI₃ CQDs. To further decrease the ligand density and, thus, improve the inter-dot coupling without losing colloidal integrity of FAPbI₃ CQDs,³¹ one more step of surface treatment was carried out during the film formation process (**Figure 2.2B**, left). However, 2-pentanol and the mixed solvent of acetonitrile/toluene used in the first two cycles of surface treatment were not applicable in this step, as upon addition of them on the CQDs film, the CQDs underwent immediate degradation. This is because after two cycles of ligand density reduction, FAPbI₃ CQDs were more exposed and, hence, more sensitive to the polarity of both the 2-pentanol and acetonitrile/toluene mixed solvent. Therefore, in the solid-state surface treatment process (third cycle), ethyl acetate (EtOAc) with a lower polarity (**Table B2.2**) was employed to rinse the FAPbI₃ CQDs film. Additionally, the shorter exposure time to antisolvent in solid-state than solution-state surface treatment further minimizes the loss of CQD integrity. Fourier-transform infrared (FTIR) spectra in **Figure 2.2B** (right) confirmed the decreased amount of the ligands in CQDs film with exposure to EtOAc. The signal intensity of C-H modes around 3000 cm⁻¹ reduced, which partially belongs to the oleyl species.⁹

2.2 Device performance of FAPbI₃ CQDs based solar cells

Photovoltaic devices were fabricated with the FAPbI₃ CQDs as a photoactive material via layer-by-layer deposition under room temperature (**Figure A2.3**). A schematic of the device structure along with the corresponding scanning electron microscopic (SEM) cross-section image of the device is shown in **Figure 2.3A**. In order to correlate the ligand density on CQDs to the photovoltaic properties of resulting devices, the devices based on FAPbI₃ CQDs with different cycles of surface treatment were fabricated. The corresponding current density-voltage (*J-V*) curves are shown in **Figure 2.3B**, where a gradual improvement in open circuit voltage (V_{oc}), short circuit current (J_{sc}),

fill factor (FF) and, consequently, the PCE was demonstrated with each step of the surface treatment process. The photovoltaic parameters are summarized in **Table B2.3**. The forward scan J-V curve of the device after a series of the surface treatments showed a high V_{OC} of 1.10 V, J_{SC} of 11.83 mA/cm² and FF of 64.42%, yielding a PCE of 8.38%. It is worth to note that the V_{OC} of the CQD device is relatively higher compared to that of the devices based on conventional chalcogenide CQDs.^{8,42} This might be attributed to the relatively higher defect tolerance of perovskite materials, which make large portion of the surface states in CQD film less detrimental to carrier transport and the resulting photovoltaic performance. The stabilized power output (SPO) of the device was measured to be 8.05% by measuring the current density, while the device was biased at 0.88 V (**Figure A2.4**). This is in good agreement with the PCE measured from the J-V scan. The histogram of solar cell efficiencies for 16 devices is shown in **Figure A2.5**, which shows the good reproducibility of the approach with an average PCE of $8.21 \pm 0.18\%$. As shown in **Figure 2.3C**, the devices showed an external quantum efficiency (EQE) onset at around 800 nm, which is correlated with the onset of absorption. The EQE onset of the devices incorporating 1- and 2-cycle-treated films shows slight blue shift compared with the one using the QD film post solid-state surface treatment. Considering that the absorption onset has hardly changed upon different surface treatment cycles (**Figure A2.6**), the EQE of the devices at longer wavelength region might be below the resolution of our measurement setup due to poor charge collection efficiency. The EQE of devices progressively increased with increasing number of ligand treatment cycle. This signifies a gradual improvement of dot-to-dot coupling as a result of decreasing ligand density, and, thus, better charge collection from the CQDs film.³¹ This proof-of-concept device without further optimization of the structure or process parameters suggests that FAPbI₃ CQDs have high potential in achieving highly efficient CQD solar cells.

2.3 Improved stability of FAPbI₃ CQDs

It is well-known that FAPbI₃ bulk materials spontaneously undergo phase transformation from black perovskite phase (α -phase) to the undesirable yellow non-perovskite polymorph (δ -phase) at room temperature. To evaluate the phase stability of our FAPbI₃ CQD film, we compared change in absorption and XRD spectra of the FAPbI₃ bulk and CQD films under ambient conditions, as shown in **Figure 2.4** (relative humidity of $\sim 35 \pm 2\%$ and temperature of 23 ± 3 °C). After exposure to ambient atmosphere for 7 days, the FAPbI₃ CQD film retained almost identical absorption spectrum without noticeable change in its color, whereas the bulk FAPbI₃ film significantly bleached with a substantial decrease in absorption over visible wavelength region (**Figure 2.4A** and **B**). The corresponding XRD pattern of the FAPbI₃ CQD film showed no change after the exposure, indicating a good phase stability of the CQD film under ambient conditions. The bulk FAPbI₃ film, on the contrary, almost completely converted to δ -phase with some hydrated form of the perovskite (indexed as h , **Figure 2.4C** and **4D**). The better phase stability of FAPbI₃ CQDs could be attributed to the quantum dot-induced size effects, in which the large contribution of the surface energy and the slight lattice contraction stabilize the α -phase of FAPbI₃.^{9,25,35} According to the phase transition thermodynamics of nanoparticles, the chemical potential is composed of the contributions from the bulk and the surface,

$$\mu = \mu^b + \mu^s \quad (1)$$

The surface chemical potential is defined as:

$$\mu^s = \left(\frac{\partial G^s}{\partial n} \right)_{T,p} = \left(\sigma \frac{\partial A}{\partial n} \right)_{T,p} \quad (2)$$

where G is Gibbs free energy, σ is the surface tension, A is the surface area, and n is the molar amount. Then the molar Gibbs free energy change of the phase transition from α -phase to δ -phase of perovskite CQDs can be expressed as:

$$\Delta_{\alpha}^{\delta}G_m = \mu_{\delta} - \mu_{\alpha} = \Delta_{\alpha}^{\delta}G_m^b + \sigma_{\beta} \left(\frac{\partial A_{\delta}}{\partial n_{\delta}} \right)_{T,p} - \sigma_{\alpha} \left(\frac{\partial A_{\alpha}}{\partial n_{\alpha}} \right)_{T,p} \quad (3)$$

$\Delta_{\alpha}^{\delta}G_m^b$ is the molar Gibbs free energy change of the phase transition for the bulk substance from α -phase to δ -phase, which can be written as $\Delta_{\alpha}^{\delta}G_m^b = \mu_{\delta}^b - \mu_{\alpha}^b$. For bulk perovskite, it undergoes spontaneous phase transition from α -phase to δ -phase due to the negative value of Gibbs free energy change of this transformation. However, in the case of perovskite CQDs, the large contribution of the terms for the surface in Equation (3) provides the chance to tune the change of Gibbs free energy to be less negative or even positive and, thus, stabilizing the α -phase of FAPbI₃. The increase in Gibbs free energy change of this phase transition can be reflected in the decrease of phase transition temperature (T_c), which is consistent with our experimental observation. The α -phase FAPbI₃ film cannot be formed until temperature is increased to 150 °C [19], whereas the α -phase FAPbI₃ CQDs are synthesized at 80 °C. From a theoretical point of view, we can derive the relationship of phase transition temperature and size effect in CQDs. By incorporating Gibbs-Helmholtz equation in Equation (3) and subsequently, performing the partial derivations of Gibbs free energy change against temperature, we can obtain the molar phase transition enthalpy $\Delta_{\alpha}^{\delta}H_m$ and molar phase transition entropy $\Delta_{\alpha}^{\delta}S_m$, as shown below:

$$\begin{aligned} \Delta_{\alpha}^{\delta}H_m &= \Delta_{\alpha}^{\delta}H_m^b + \sigma_{\delta} \left(\frac{\partial A_{\delta}}{\partial n_{\delta}} \right)_{T,p} - T \left(\frac{\partial \sigma_{\delta}}{\partial T} \right)_p \left(\frac{\partial A_{\delta}}{\partial n_{\delta}} \right)_{T,p} - T \sigma_{\delta} \left[\frac{\partial}{\partial T} \left(\frac{\partial A_{\delta}}{\partial n_{\delta}} \right)_{T,p} \right]_p \\ &- \sigma_{\alpha} \left(\frac{\partial A_{\alpha}}{\partial n_{\alpha}} \right)_{T,p} + T \left(\frac{\partial \sigma_{\alpha}}{\partial T} \right)_p \left(\frac{\partial A_{\alpha}}{\partial n_{\alpha}} \right)_{T,p} + T \sigma_{\alpha} \left[\frac{\partial}{\partial T} \left(\frac{\partial A_{\alpha}}{\partial n_{\alpha}} \right)_{T,p} \right]_p \end{aligned} \quad (4)$$

$$\Delta_{\alpha}^{\delta}S_m = \Delta_{\alpha}^{\delta}S_m^b - \left(\frac{\partial \sigma_{\delta}}{\partial T} \right)_p \left(\frac{\partial A_{\delta}}{\partial n_{\delta}} \right)_{T,p} - \sigma_{\delta} \left[\frac{\partial}{\partial T} \left(\frac{\partial A_{\delta}}{\partial n_{\delta}} \right)_{T,p} \right]_p + \left(\frac{\partial \sigma_{\alpha}}{\partial T} \right)_p \left(\frac{\partial A_{\alpha}}{\partial n_{\alpha}} \right)_{T,p} + \sigma_{\alpha} \left[\frac{\partial}{\partial T} \left(\frac{\partial A_{\alpha}}{\partial n_{\alpha}} \right)_{T,p} \right]_p$$

(5)

At equilibrium, $\Delta_{\alpha}^{\delta}G_m = 0$, and $\Delta_{\alpha}^{\delta}G_m = \Delta_{\alpha}^{\delta}H_m - T_c \Delta_{\alpha}^{\delta}S_m$, so

$$T_c = \frac{1}{\Delta_\alpha^\delta S_m^b} \left\{ \Delta_\alpha^\delta H_m^b + \sigma_\delta \left(\frac{\partial A_\delta}{\partial n_\delta} \right)_{T,p} - \sigma_\alpha \left(\frac{\partial A_\alpha}{\partial n_\alpha} \right)_{T,p} \right\} \quad (6)$$

For a spherical model,

$$\left(\frac{\partial A_\alpha}{\partial n_\alpha} \right)_{T,p} = \frac{2V_{m,\alpha}}{r_\alpha} \quad (7)$$

where $V_{m,\alpha}$ is the molar volume of α -phase FAPbI₃ perovskite and r_α is the radius of the particle.⁴⁴⁻

⁴⁶ Equation 6 shows how T_c of FAPbI₃ CQDs is directly affected by the size of the particle, surface tension and molar volumes of α -phase and δ -phase of FAPbI₃. In **Figure 2.5A-D**, a delicate XRD measurement was performed using the Bede high resolution X-ray diffractometer. The target material of the X-ray diffractometer was copper and the resulting X-rays were aligned in parallel before coming in contact with the sample of interest. The precision of the ω and 2θ motors were within 1 arcsecond (1/3600 of a degree). The both forms of the perovskite material were deposited on (001) silicon wafers. To exclude any error caused by alignment, we used characteristic peak from a silicon wafer substrate to calibrate the alignment (**Figure 2.5A and B**). As seen in **Figure 2.5A**, the peaks from the silicon wafer substrates of bulk and QD films are perfectly matched, indicating the beam alignment is identical. As can be seen in **Figure 2.5B and C**, slight shifts of characteristic XRD peaks to higher diffraction angle observed in FAPbI₃ CQDs indicate decreased lattice constant and molar volume of FAPbI₃ CQDs compared to bulk FAPbI₃. Considering the negative value of $\Delta_\alpha^\delta H_m^b$ and $\Delta_\alpha^\delta S_m^b$ in Equation (6), the decrease in $\left(\frac{\partial A_\alpha}{\partial n_\alpha} \right)_{T,p}$ term may help decrease the T_c of FAPbI₃ CQDs and, thus, stabilize the α -phase FAPbI₃ at room temperature.

Finally, we evaluated the stability of the devices under ambient and operational conditions, as shown in **Figure 2.5C and D**. Under ambient conditions, FAPbI₃ CQD device showed an excellent

stability without any degradation in PCE for 60 days. In the case of the FAPbI₃ bulk film-based device, however, the PCE significantly degraded to 29.5% of the initial PCE, which is probably due to the conversion of α -phase to δ -phase under ambient conditions. Due to phase transition, the color of the device was completely bleached after 60 days, while that of the CQD device remained unchanged (inset of **Figure 2.5C**). Light stability of the devices was further explored by exposing the encapsulated devices to a continuous illumination (90 ± 5 mW/cm²). Devices were encapsulated under nitrogen atmosphere and exposed under open-circuit condition, of which SPO was periodically measured under one sun illumination (**Figure 2.5D**). The *J-V* curves and photovoltaic parameters of the devices used for the measurement can be found in **Figure A2.7** and **Table B2.4**. The bulk FAPbI₃ device showed a rapid initial decay followed by a slower decay with almost linear profile, which is in agreement with the previous report.⁴⁷ Upon exposure for 226 h, the PCEs of the devices were degraded to 69.1% of the initial PCEs. Surprisingly, the CQD devices showed only marginal degradation (1.1% of the initial PCE) after 226 h of the exposure. The superior light stability of the CQD devices over bulk devices offers a possible approach to enhancing the operational stability of the perovskite solar cells using quantum dot approach.

2.4 Conclusion

In summary, the first FAPbI₃ CQD-based photovoltaic device has been achieved by effective control of surface ligand density using a rationally designed surface treatment process. A series of ‘Grade II’ solvents (with moderate polarity that can effectively reduce the ligand density, while maintaining the integrity of perovskite CQDs) with gradually reducing polarity were utilized in the process. Our proof-of-concept device showed a promising PCE exceeding 8% with a broad spectral response up to a near-infrared region. It is worthy to note that the FAPbI₃ CQD films and devices

have shown superior ambient and operational stability to their bulk form. We believe our strategy to regulate the ligand density on the surface of hybrid perovskites will provide an effective methodological basis for achieving highly efficient and stable perovskite CQD optoelectronic devices.

References

1. Kagan, C.R., Lifshitz, E., Sargent, E.H., and Talapin, D. V. (2016). Building devices from colloidal quantum dots. *Science* 353, aac5523.
2. McDonald, S.A., Konstantatos, G., Zhang, S., Cyr, P.W., Klem, E.J.D., Levina, L., and Sargent, E.H. (2005). Solution-processed PbS quantum dot infrared photodetectors and photovoltaics. *Nat. Mater.* 4, 138–142.
3. Nozik, A.J., Beard, M.C., Luther, J.M., Law, M., Ellingson, R.J., and Johnson, J.C. (2010). Semiconductor quantum dots and quantum dot arrays and applications of multiple exciton generation to third-generation photovoltaic solar cells. *Chem. Rev.* 110, 6873–6890.
4. Carey, G.H., Abdelhady, A.L., Ning, Z., Thon, S.M., Bakr, O.M., and Sargent, E.H. (2015). Colloidal Quantum Dot Solar Cells. *Chem. Rev.* 115, 12732–12763.
5. Brown, P.R., Kim, D., Lunt, R.R., Zhao, N., Bawendi, M.G., Grossman, J.C., and Bulovi, V. (2014). Energy Level Modification in Lead Sulfide Quantum Dot Thin Films through Ligand Exchange. 5863–5872.
6. Ning, Z., Voznyy, O., Pan, J., Hoogland, S., Adinolfi, V., Xu, J., Li, M., Kirmani, A.R., Sun, J.-P., Minor, J., *et al.* (2014). Air-stable n-type colloidal quantum dot solids. *Nat. Mater.* 13, 822–828.
7. Tang, J., Kemp, K.W., Hoogland, S., Jeong, K.S., Liu, H., Levina, L., Furukawa, M., Wang,

- X., Debnath, R., Cha, D., *et al.* (2011). Colloidal-quantum-dot photovoltaics using atomic-ligand passivation. *Nat Mater* *10*, 765–771.
8. Liu, M., Voznyy, O., Sabatini, R., García de Arquer, F.P., Munir, R., Balawi, A.H., Lan, X., Fan, F., Walters, G., Kirmani, A.R., *et al.* (2016). Hybrid organic–inorganic inks flatten the energy landscape in colloidal quantum dot solids. *Nat. Mater.* *16*, 258–263.
 9. Abhishek S., Ashley R. M., Erin M. S., Boris D. C., David T. M., Jeffrey A. C., Tamoghna C., Joseph M. L. (2016). Quantum dot-induced phase stabilization of a-CsPbI₃ perovskite for high-efficiency photovoltaics. *Science* *354*, 92-95.
 10. Liu, F., Ding, C., Zhang, Y., Ripolles, T.S., Kamisaka, T., Toyoda, T., Hayase, S., Minemoto, T., Yoshino, K., Dai, S., *et al.* (2017). Colloidal Synthesis of Air-Stable Alloyed CsSn_{1-x}Pb_xI₃ Perovskite Nanocrystals for Use in Solar Cells. *J. Am. Chem. Soc.*, *139*, 16708-16719.
 11. Hoffman, J.B., Zaiats, G., Wappes, I., and Kamat, P. V. (2017). CsPbBr₃ Solar Cells: Controlled Film Growth through Layer-by-Layer Quantum Dot Deposition. *Chem. Mater.*, *29*, 9767-9774.
 12. Sanhira, E.M., Marshall, A.R., Christians, J.A., Harvey, S.P., Ciesielski, P.N., Wheeler, L.M., Schulz, P., Lin, L.Y., Beard, M.C., and Luther, J.M. (2017). Enhanced mobility CsPbI₃ quantum dot arrays for record-efficiency, high-voltage photovoltaic cells. *Sci. Adv.*, *3*, eaao4204.
 13. Yin, W.-J., Yang, J.-H., Kang, J., Yan, Y., and Wei, S.-H. (2015). Halide perovskite materials for solar cells: a theoretical review. *J. Mater. Chem. A* *3*, 8926–8942.
 14. Wehrenfennig, C., Eperon, G.E., Johnston, M.B., Snaith, H.J., and Herz, L.M. (2014). High charge carrier mobilities and lifetimes in organolead trihalide perovskites. *Adv. Mater.* *26*,

1584–1589.

15. Yin, W.J., Shi, T., and Yan, Y. (2014). Unique properties of halide perovskites as possible origins of the superior solar cell performance. *Adv Mater* 26, 4653–4658.
16. Kovalenko, M. V, Protesescu, L., and Bodnarchuk, M.I. (2017). Properties and potential optoelectronic applications of lead halide perovskite nanocrystals. *750*, 745–750.
17. Akkerman, Q.A., Rainò, G., Kovalenko, M. V, and Manna, L. (2018). Genesis, challenges and opportunities for colloidal lead halide perovskite nanocrystals. *Nat. Mater.* 17, 394-405.
18. Tong, Y., Ehrat, F., Vanderlinden, W., Cardenas-daw, C., and Stolarczyk, J.K. (2016). Dilution-Induced Formation of Hybrid Perovskite Nanoplatelets. *ACS Nano* 10, 10936-10944.
19. Zhang, F., Huang, S., Wang, P., Chen, X., Zhao, S., Dong, Y., and Zhong, H. (2017). Colloidal Synthesis of Air-Stable $\text{CH}_3\text{NH}_3\text{PbI}_3$ Quantum Dots by Gaining Chemical Insight into the Solvent Effects. *Chem. Mater.* 29, 3793-3799.
20. Kulbak, M., Gupta, S., Kedem, N., Levine, I., Bendikov, T., Hodes, G., and Cahen, D. (2016). Cesium Enhances Long-Term Stability of Lead Bromide Perovskite-Based Solar Cells. *J. Phys. Chem. Lett.* 7, 167–172.
21. Lee, J.W., Kim, D.H., Kim, H.S., Seo, S.W., Cho, S.M., and Park, N.G. (2015). Formamidinium and cesium hybridization for photo- and moisture-stable perovskite solar cell. *Adv. Energy Mater.* 5. 1501310.
22. Zhu, H., Miyata, K., Fu, Y., Wang, J., Joshi, P.P., Niesner, D., Williams, K.W., Jin, S., and Zhu, X.-Y. (2016). Screening in crystalline liquids protects energetic carriers in hybrid perovskites. *Science.* 353, 1409–1413.
23. Bian, H., Bai, D., Jin, Z., Wang, K., Liang, L., Wang, H., Zhang, J., Wang, Q., and Liu, S.

- (Frank) (2018). Graded Bandgap CsPbI_{2+x}Br_{1-x} Perovskite Solar Cells with a Stabilized Efficiency of 14.4%. *Joule*, 1–11.
24. Eperon, G.E., Patemo, G.M., Sutton, R.J., Zampetti, A., Haghighirad, A.A., Cacialli, F., and Snaith, H.J. (2015). Inorganic caesium lead iodide perovskite solar cells. *J. Mater. Chem. A* 3, 19688–19695.
 25. Eperon, G.E., Stranks, S.D., Menelaou, C., Johnston, M.B., Herz, L.M., and Snaith, H.J. (2014). Formamidinium lead trihalide: a broadly tunable perovskite for efficient planar heterojunction solar cells. *Energy Environ. Sci.* 7, 982.
 26. Lee, J.W., Seol, D.J., Cho, A.N., and Park, N.G. (2014). High-efficiency perovskite solar cells based on the black polymorph of HC(NH₂)₂PbI₃. *Adv. Mater.* 26, 4991–4998.
 27. Jeon, N.J., Noh, J.H., Yang, W.S., Kim, Y.C., Ryu, S., Seo, J., and Seok, S. Il (2015). Compositional engineering of perovskite materials for high-performance solar cells. *Nature* 517, 476–480.
 28. Protesescu, L., Yakunin, S., Kumar, S., Bär, J., Bertolotti, F., Masciocchi, N., Guagliardi, A., Grotevent, M., Shorubalko, I., Bodnarchuk, M.I., *et al.* (2017). Dismantling the “red Wall” of Colloidal Perovskites: Highly Luminescent Formamidinium and Formamidinium-Cesium Lead Iodide Nanocrystals. *ACS Nano* 11, 3119–3134.
 29. Imran, M., Caligiuri, V., Wang, M., Goldoni, L., Prato, M., Krahne, R., Trizio, L. De, and Manna, L. (2018). Benzoyl Halides as Alternative Precursors for the Colloidal Synthesis of Lead-Based Halide Perovskite Nanocrystals. *J. Am. Chem. Soc.* 140, 2656–2664.
 30. Lee, J., Dai, Z., Lee, C., Lee, H.M., Han, T., Marco, N. De, Lin, O., Choi, C.S., Dunn, B.S., Carlo, D., Jeong Ho., Heather D. M., and Yang Y. (2018). Tuning Molecular Interactions for Highly Reproducible and Efficient Formamidinium Perovskite Solar Cells via Adduct

- Approach. *J. Am. Chem. Soc.* *140*, 6317-6324.
31. Kagan, C.R., and Murray, C.B. (2015). Charge transport in strongly coupled quantum dot solids. *Nat. Nanotechnol.* *10*, 1013–1026.
 32. De Roo, J., Ibáñez, M., Geiregat, P., Nedelcu, G., Walravens, W., Maes, J., Martins, J.C., Van Driessche, I., Kovalenko, M. V., and Hens, Z. (2016). Highly Dynamic Ligand Binding and Light Absorption Coefficient of Cesium Lead Bromide Perovskite Nanocrystals. *ACS Nano* *10*, 2071–2081.
 33. Anderson, N.C., Hendricks, M.P., Choi, J.J., and Owen, J.S. (2013). Ligand exchange and the stoichiometry of metal chalcogenide nanocrystals: Spectroscopic observation of facile metal-carboxylate displacement and binding. *J. Am. Chem. Soc.* *135*, 18536–18548.
 34. Boles, M.A., Ling, D., Hyeon, T., and Talapin, D. V (2016). The surface science of nanocrystals. *15*, 141–154.
 35. Bekenstein, Y., Koscher, B.A., Eaton, S.W., Yang, P., and Alivisatos, A.P. (2015). Highly Luminescent Colloidal Nanoplates of Perovskite Cesium Lead Halide and Their Oriented Assemblies. *J. Am. Chem. Soc.* *137*, 16008–16011.
 36. Reichardt, C. (2003). Solvents and solvent effects in organic chemistry .
 37. Hansen, C.M. (2007). Hansen Solubility Parameters: A User's Handbook, Second Edition, 2 edn (CRC Press).
 38. Wang, J., Giacomo, F. Di, Brüls, J., Gortler, H., Katsouras, I., Groen, P., Janssen, A.J., Andriessen, R., and Galagan, Y. (2017). Highly Efficient Perovskite Solar Cells Using Non-Toxic Industry Compatible Solvent System. *1700091*, 1–9.
 39. Gardner, K.L., Tait, J.G., Merckx, T., Qiu, W., Paetzold, U.W., Kootstra, L., Jaysankar, M., Gehlhaar, R., Cheyns, D., and Heremans, P. (2016). Nonhazardous Solvent Systems for

Processing Perovskite Photovoltaics. *Adv. Energy Mater.* *6*, 1600386.

40. Li, J., Xu, L., Wang, T., Song, J., Chen, J., Xue, J., Dong, Y., Cai, B., Shan, Q., Han, B., and Zeng, H. (2017). 50-Fold EQE Improvement up to 6.27% of Solution-Processed All-Inorganic Perovskite CsPbBr₃ QLEDs via Surface Ligand Density Control. *Adv. Mater.* *29*, 1603885.
41. Smith, A.M., Johnston, K.A., Crawford, S.E., Marbella, L.E., and Millstone, J.E. (2017). Ligand density quantification on colloidal inorganic nanoparticles. *Analyst* *142*, 11–29.
42. Carey, G.H., Abdelhady, A.L., Ning, Z., Thon, S.M., Bakr, O.M., and Sargent, E.H. (2015). Colloidal Quantum Dot Solar Cells. *Chem. Rev.* *115*, 12732-12763.
43. Zheng, X., Wu, C., Jha, S.K., Li, Z., Zhu, K., and Priya, S. (2016). Improved Phase Stability of Formamidinium Lead Triiodide Perovskite by Strain Relaxation. *ACS Energy Lett.* *1*, 1014–1020.
44. Carter, C.B., and Norton, M.G. (2007). *Solid-State Phase Transformations and Reactions*. Book, 444–462.
45. Zhang, W., Xue, Y., Fu, Q., Cui, Z., and Wang, S. (2017). Size dependence of phase transition thermodynamics of nanoparticles: A theoretical and experimental study. *Powder Technol.* *308*, 258–265.
46. Cui, Z.-X., Zhao, M.-Z., Lai, W.-P., and Xue, Y.-Q. (2011). Thermodynamics of Size Effect on Phase Transition Temperatures of Dispersed Phases. *J. Phys. Chem. C* *115*, 22796–22803.
47. Domanski, K., Roose, B., Matsui, T., Saliba, M., Turren-Cruz, S.-H., Correa-Baena, J.-P., Carmona, C.R., Richardson, G., Foster, J.M., De Angelis, F., *et al.* (2017). Migration of cations induces reversible performance losses over day/night cycling in perovskite solar

cells. *Energy Environ. Sci.* *10*, 604–613.

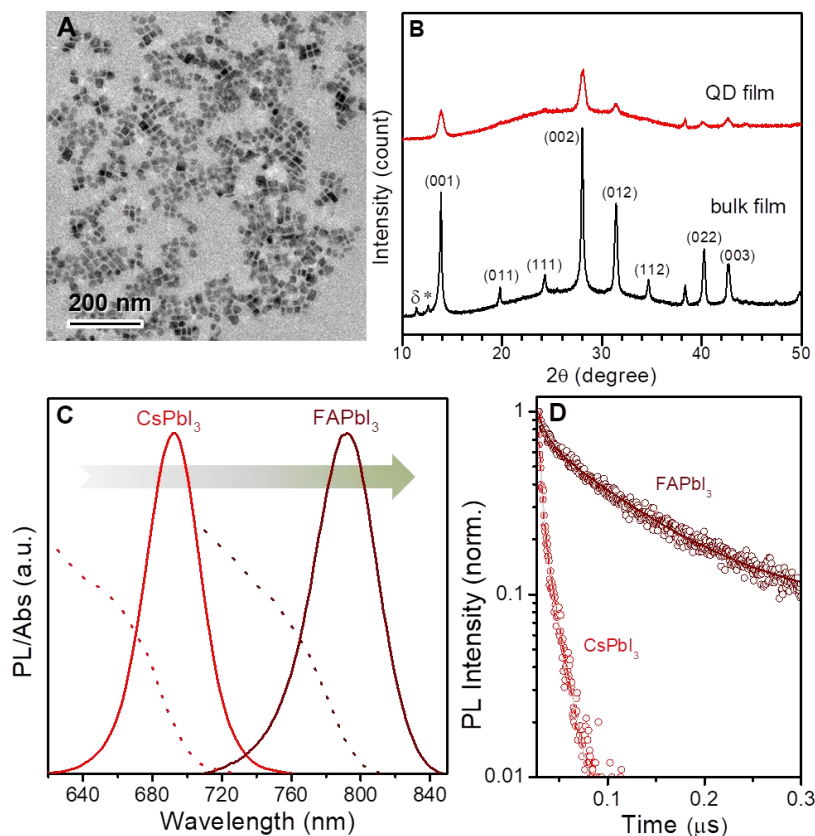


Figure 2.1 (A) Transmission electron microscopic (TEM) image and (B) X-ray diffraction (XRD) patterns of as-synthesized FAPbI₃ CQDs and bulk films; δ and * indicate hexagonal non-perovskite phase and PbI₂, respectively. (C) UV-visible absorption (broken lines), steady-state photoluminescence (PL, solid lines) and (D) time-resolved PL spectra of CsPbI₃ CQDs (red) and FAPbI₃ CQDs (dark red). Open circles indicate measured data while solid lines are fitted curves.

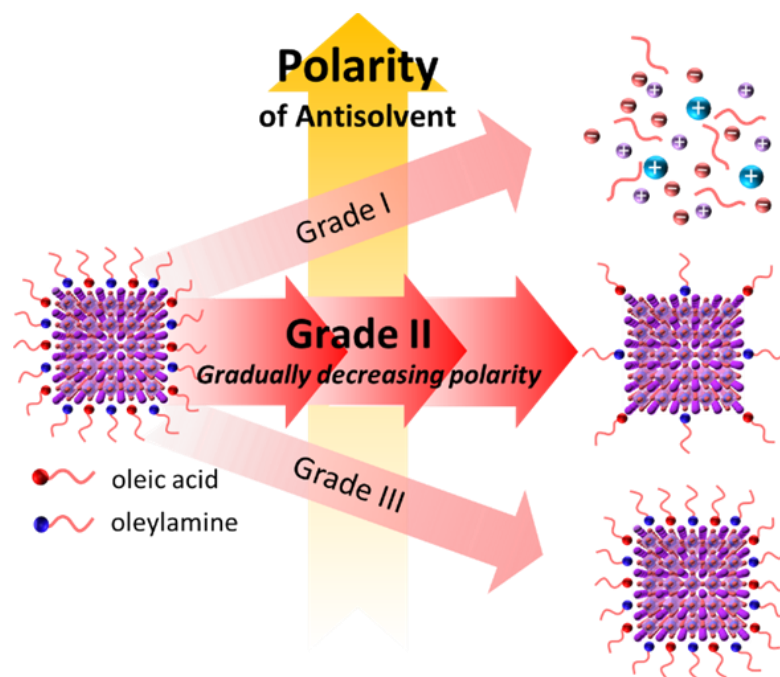


Figure 2.2 The strategy for designing rational solvent-treatment routes to manage surface ligands of FAPbI₃ CQDs.

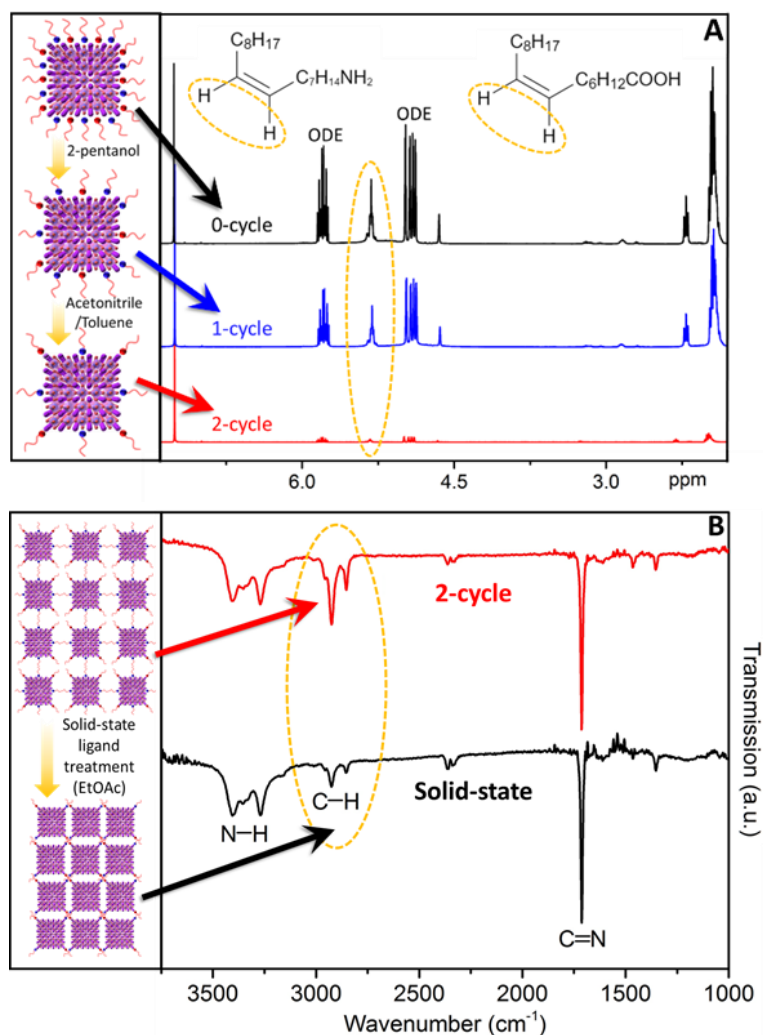


Figure 2.3 (A) Nuclear magnetic resonance (NMR) spectra of FAPbI₃ CQDs with increasing number of surface treatment cycles in solution, indicating a gradual decrease of the oleyl species (right) and schematic illustration of the ligand density control during solution-state surface treatment (left); (B) Fourier transform infrared (FTIR) spectra of FAPbI₃ CQDs before and after solid-state surface treatment (right) and a schematic illustration of the ligand density change and inter-dot coupling during the solid-state surface treatment (left).

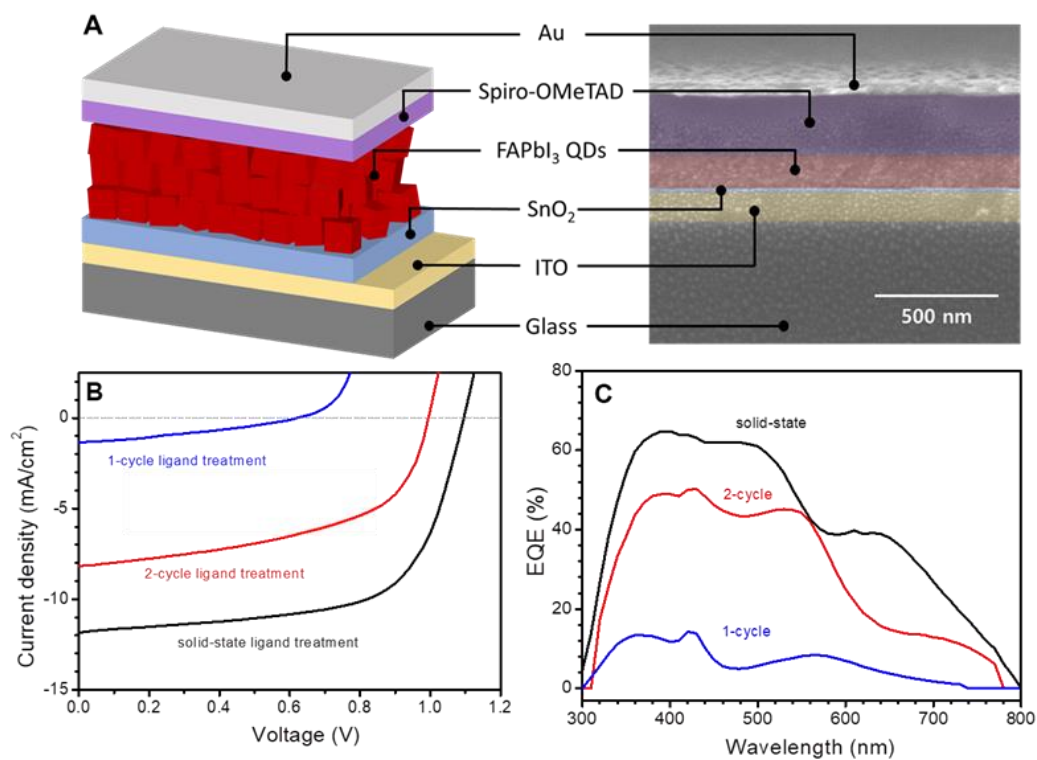


Figure 2.4 (A) A Schematic device structure and cross sectional scanning electron microscopic (SEM) image of the FAPb₃ CQDs solar cell; (B) current density-voltage (*J-V*) curves and (C) External quantum efficiency (EQE) of the devices based on FAPb₃ CQDs with increasing cycles of surface treatment.

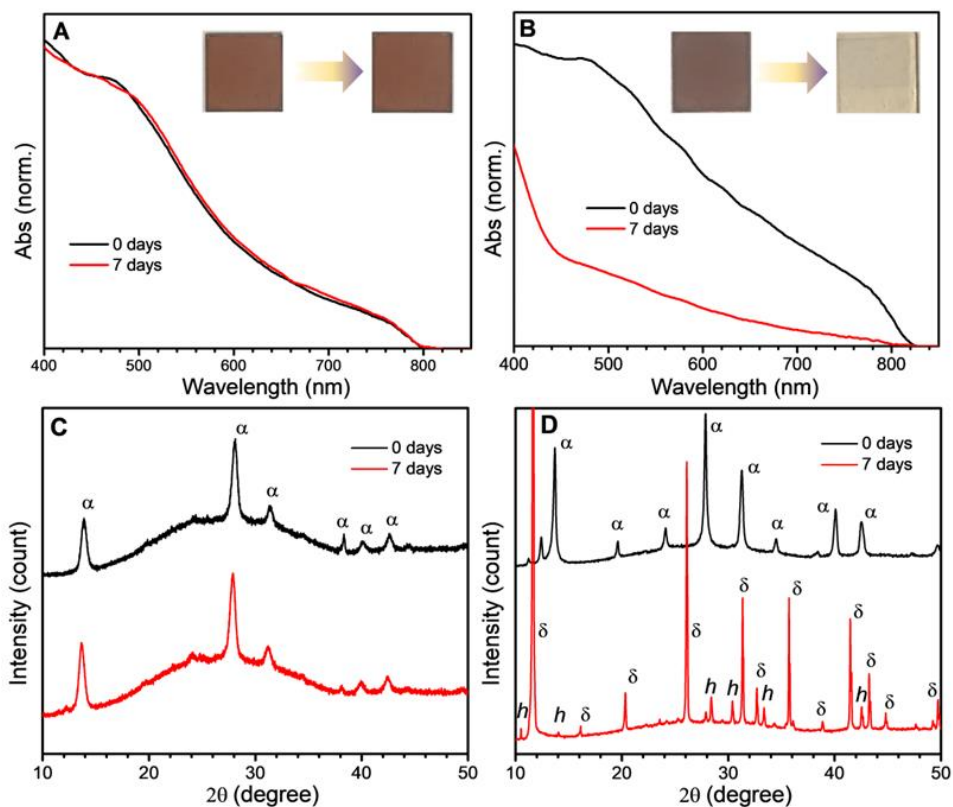


Figure 2.5 (A, B) UV-vis absorption spectra of (A) FAPbI₃ CQDs and (B) bulk FAPbI₃ stored under ambient condition (relative humidity $\sim 35 \pm 2\%$ and temperature 23 ± 3 °C). Inset of (A) and (B) shows corresponding photos of the films. (C, D) X-ray diffraction (XRD) patterns of (C) FAPbI₃ CQDs and (D) bulk FAPbI₃ films measured before and after the exposure. α : cubic perovskite phase, δ : hexagonal non-perovskite phase, h : hydrated perovskite phase.

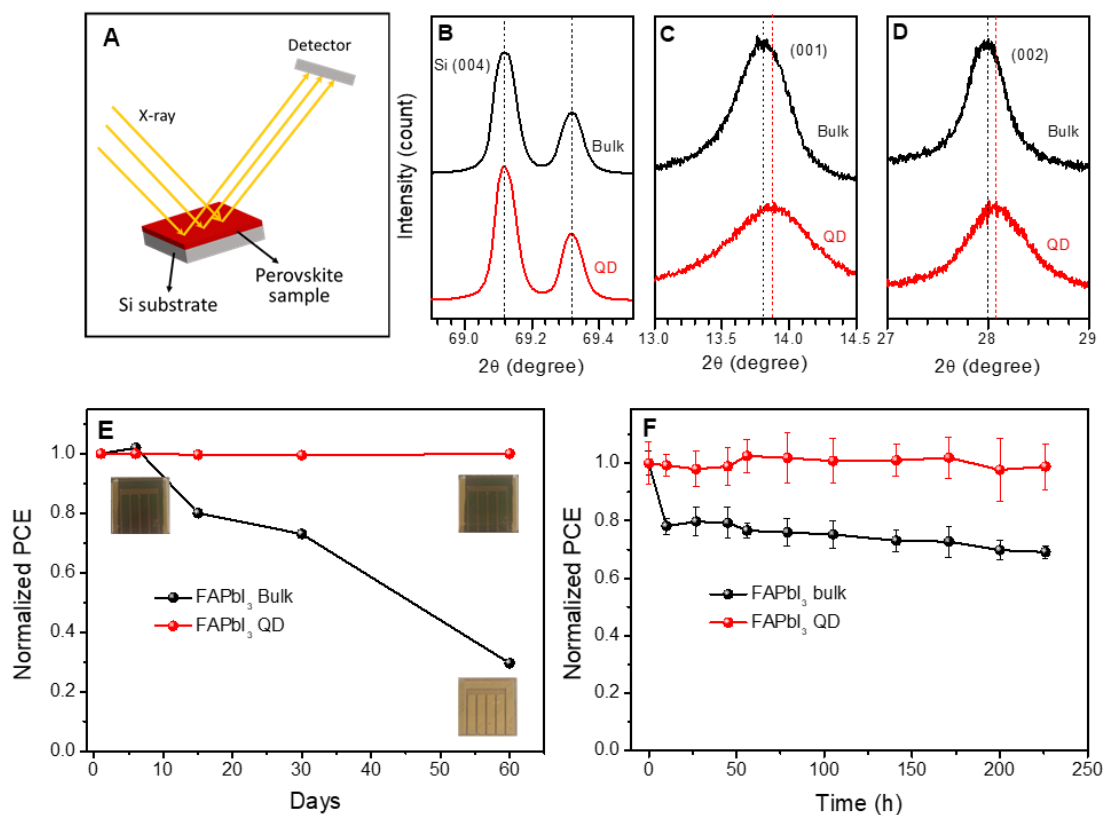


Figure 2.6 (A) A schematic showing XRD measurement. Characteristic XRD peaks of (B) silicon substrate at plane (004), (C) at plane (001) and (D) at plane (002) of bulk FAPbI₃ and FAPbI₃ CQD films. (E) Evolution of power conversion efficiency (PCE) of photovoltaic devices based on bulk FAPbI₃ and FAPbI₃ CQDs stored under ambient condition without encapsulation. Inset of (E) shows photos of the device before and after the exposure. (F) Change in PCE of the encapsulated device under continuous illumination (90 ± 5 mW/cm²). The devices were maintained under open-circuit condition at room temperature (ca. 30 ± 3 °C).

Table 2.1 The summary of size and ligand density of FAPbI₃ CQDs after different number of surface treatment cycles in solution phase

Purification times	0-cycle	1- cycle	2- cycle
Size (nm)	12.8	16.3	17.7
Concentration of CQD (μM)	14.7	12.4	9.3
Concentration of oleyl species (a.u.)	52.5	39.6	21.2
Ligand density (a.u./nm ²)	3.6	2.0	1.2

Chapter 3 Small Molecule ‘Charge Driver’ Enables Perovskite Quantum Dot Solar Cells with Efficiency Approaching 13%

Colloidal quantum dots (CQDs) have attracted significant attention for photovoltaic application in recent decades due to their unique properties. Not only their immense tunability in bandgap, electronic states, and surface chemistry enable them to be good candidates for new generation solar cells,^[1–4] but also the multiple exciton generation phenomenon, specific to CQDs, opens an avenue to make full utilization of solar radiation.^[5–7] Recently, halide perovskite CQDs have emerged as a new class of CQDs for photovoltaics, offering compelling combination of the advantages of traditional CQDs and exceptional properties of halide perovskite materials, such as the desirable bandgap, high absorption coefficient, and defect tolerance.^[8–10] Furthermore, the perovskite CQDs, such as CsPbI₃ and formamidinium lead iodide (FAPbI₃), were reported to show superior phase stability over their bulk form owing to the size-induced lattice strain and enhanced contribution from the surface energy.^[11,12] Accordingly, the CQD solar cells based on the perovskite material have demonstrated a great potential with a record power conversion efficiency (PCE) as high as 13% along with excellent operational stability.^[12,13]

Although perovskite materials display superior optoelectronic properties to the conventional semiconductors, the low charge carrier separation efficiency, which is one of the critical obstacles towards higher performance of traditional CQD devices, still remains in the perovskite CQD solar cells.^[14] While exciton binding energies (E_b) of bulk perovskite materials were measured to be as low as few millielectronvolts, facilitating spontaneous generation of free carriers at room

temperature,^[15] the E_b of the perovskite CQD was estimated to be significantly higher (up to ten times) than that of the bulk counterparts.^[9,16] As a result, the photo-generated charge carriers in the CQD films are subjected to be lost through recombination before being extracted to selective contact layers.^[17] Therefore, promoting effective charge separation to reduce recombination becomes a crucial factor for boosting the PCE of the perovskite CQD solar cells.

In order to facilitate such charge separation process and thus reduce the charge recombination in conventional CQD solar cells, a lot of efforts have been developed, such as core-shell structural design, surface ligand modification and device structure engineering.^[18–23] These available strategies employed in the traditional CQDs devices, however, are still not compatible with perovskite CQD system owing to their vulnerable structural stability as well as absence of well-established synthetic routes.^[3,8] For example, in contrast to various colloidal structures in chalcogenide quantum dots like type-II core-shell CdS/CdSe^[24] and CdTe/CdSe^[25] enabling spatial charge separation, no synthetic route has been developed yet for core shell structured perovskite CQDs yet. Moreover, different from the versatile organic and inorganic surface functionalization of metal chalcogenide CQDs, the employed ligands in perovskite CQDs are limited to long-alkyl-chain acids and amines and hence, restrict the opportunity to tailor the electronic properties of CQDs via fine tuning of surface states as commonly achieved in traditional CQDs.^[2,4,26,27] Therefore, we were motivated to develop a new strategy for facilitating efficient charge carrier collection in perovskite CQD solar cells. Here, we developed a facile strategy that takes advantage of conjugated small molecules and perovskite CQD hetero-interface and, as a result, provides an additional driving force for effective charge separation in FAPbI₃ perovskite CQD solar cells. The champion CQD solar cell with a small molecule acting as a ‘charge driver’ showed a promising

PCE of 12.7%, the highest efficiency reported for FAPbI₃ CQD based photovoltaics, demonstrating a great potential of this strategy for enhancing the efficiency of perovskite CQD solar cells.

3.1 The effect of ITIC on the photovoltaic performance of CQDs based device

APbI₃ CQDs based photovoltaic devices were fabricated using a layer-by-layer deposition method as previously reported.^[12] Ethyl acetate (EtOAc) was employed as an anti-solvent to remove the ligands on the surface of CQDs during the solid state film treatment. A conjugated small molecule 2,2'-[[6,6,12,12-Tetrakis(4-hexylphenyl)-6,12-dihydrodithieno[2,3-d:2',3'-d']-s-indaceno[1,2-b:5,6-b']dithiophene-2,8-diyl]bis[methyldiylidene(3-oxo-1H-indene-2,1(3H)-diylidene)]]bis[propanedinitrile] (ITIC), chemical structure of which is shown in the insert of **Figure 3.1**, was introduced into EtOAc that was used to rinse the CQD film (illustrated in **Figure 3.1**). While EtOAc removed the excess ligands of perovskite CQDs, ITIC in EtOAc remained in the CQD film forming a heterostructure. Based on this strategy, photovoltaic devices were fabricated with a structure of ITO/SnO₂/CQDs/Spiro-OMeTAD/Ag, cross-sectional scanning electron microscopic (SEM) image of which is shown in **Figure 3.2a**. A dense and uniform CQD film with a thickness of approximately 300 nm was clearly observed. Current density-voltage (*J-V*) curves of the CQDs devices without and with introduction of ITIC were compared in **Figure 3.2b**. The best device without ITIC showed a PCE of 10.4% with an open-circuit voltage (*V*_{OC}) of 1.03 V, short-circuit current density (*J*_{SC}) of 14.3 mA cm⁻², and fill factor (FF) of 70.9% (**Figure 3.2b**). Upon incorporation of the ITIC, the device PCE increased to 12.7% with *V*_{OC} of 1.10 V, *J*_{SC} of 15.4 mA cm⁻², and FF of 74.8%, indicating a large improvement in device performance with ITIC. Notably, the device showed negligible current-voltage hysteresis as demonstrated in **Figure A3.1**. The stabilized power output (SPO) of the device was measured to be 12.7% by measuring the

current density, while the device was biased at 0.90 V (**Figure 3.2c**). This is in good agreement with the PCE measured from the J - V scan. The external quantum efficiency (EQE) of the device with ITIC (shown in **Figure A3.2**) showed an obvious improvement compared to that of the reference device, which is consistent with the improved J_{SC} of the one with ITIC. The histogram of solar cell efficiencies for 40 devices is shown in **Figure 3.2d**, which confirms good reproducibility of the performance improvement with ITIC (21% improvement in an average PCE from $9.9\pm 0.3\%$ to $12.0\pm 0.4\%$ with incorporation of the ITIC).

3.2 Properties and carrier dynamics of CQDs thin films

Figure 3.3A shows the transmission electron microscopic (TEM) image of the as-synthesized FAPbI₃ CQDs using a modified hot-injection method previously reported.^[12] The CQDs were nearly monodispersed with an average size of 14 nm. High-resolution transmission electron microscopic (HRTEM) shows the cubic structure of the as-synthesized CQDs. (Figure A3.3) X-ray diffraction (XRD) measurement of FAPbI₃ CQDs films with and without ITIC confirmed the cubic phase of the film in both cases (Figure A3.4). The as-fabricated films exhibited a superior phase stability compared with their bulk counterparts due to the surface effects in CQDs ^[11,13,28]. Over a course of 5 days under ambient condition, the perovskite CQD film maintained its cubic phase, showing almost identical absorption spectrum before and after storage (Figure A3.5a). In contrast, perovskite bulk film underwent an almost complete phase transformation to a ‘yellow’ phase, showing a substantial decrease in absorption over visible wavelength region (Figure A3.5b). UV-vis absorption spectrum of FAPbI₃ CQDs film incorporated with ITIC was almost identical to that of pure FAPbI₃ CQDs film, suggesting that ITIC had negligible effect on the total absorbance of the film (**Figure 3.3B**). Thus, we speculated that the large improvement of device performance is

related to a reduced charge recombination and/or enhanced charge collection efficiency instead of light harvesting.

To understand the carrier dynamics and ascertain the role of ITIC, photo-physical properties of CQDs films were further investigated. As shown in **Figure 3.3C**, CQDs film with ITIC showed strong steady state photoluminescence (PL) quenching compared with the reference sample. Correspondingly, the time-resolved photoluminescence (TRPL) decay profile of FAPbI₃ CQDs with ITIC exhibited nearly biexponential decay characteristics with much shorter relaxation time of 2.5 ns (**Figure 3.3D**) than that of the bare FAPbI₃CQDs (17.2 ns). The significantly quenched PL intensity and faster PL decay profile indicated the electron transfer from FAPbI₃ CQDs to ITIC which is commonly known as an acceptor in organic photovoltaic (OPV) devices.^[27,29] We posit that ITIC played a crucial role in charge carrier dynamics of CQDs film enhancing charge separation and reducing the charge recombination rate.^[30,31]

The charge transfer dynamics in FAPbI₃ CQDs/ITIC system were further studied by measuring the broadband femtosecond time-resolved transient absorption (TA) spectra. Generally, the TA signal consists of ground-state bleaching (GSB, $\Delta T/T > 0$), excited-state absorption (ESA, $\Delta T/T < 0$), and stimulated emission (SE, $\Delta T/T > 0$). **Figure 3.4a** and **4b** shows the broadband TA of FAPbI₃ CQD films with and without ITIC, respectively. By Comparing the dynamics at bleaching peak at around 770 nm (**Figure 3.4c**), it was found that the decay of the bleaching signal from the CQDs/ITIC sample was much faster than that of pure CQDs, which featured a similar trend with the result of TRPL. Increasing the amount of ITIC further accelerated the decay profile, indicating that the faster decay is due to added ITIC (Figure A3.6). Differential transmission spectra ($\Delta T/T$) at different time

delays of pure FAPbI₃ CQDs nearly matched with the one with ITIC after normalization to the maximum, suggesting that the TA signal of pure FAPbI₃ CQDs originated only from the recombination of excited carriers in CQDs (Figure A3.7a). In contrast, a bleaching signal around 670 nm appeared in the sample of FAPbI₃ CQD with ITIC, overlapping with the ESA (Figure A3.7b). This bleaching signal became more obvious in CQD/ITIC sample with increasing amount of ITIC (Figure A3.7c), which could be assigned to the GSB of ITIC.^[32] Generally, this bleaching might originate from direct excitation of ITIC, energy transfer from CQDs to ITIC, or charge transfer from CQDs to ITIC. Since the pumping wavelength was designed to be 532 nm to avoid the absorption range of ITIC (550 nm-750 nm), and the $\Delta T/T$ spectra of the samples with and without ITIC exhibited almost the same profile right after the excitation (1ps) while the GSB signal of ITIC rose relatively late, the bleaching signal could hardly come from direct excitation of ITIC (Figure A3.8). Besides, the bandgap of ITIC is larger compared to that of FAPbI₃ CQD, hence the possibility of energy transfer from the CQD to ITIC could also be excluded. In addition, both direct excitation and energy transfer process would excite the electron-hole pair in ITIC, which has a relatively short lifetime.^[32,33] Contrary to this, the ITIC GSB signal in our CQD/ITIC system was sustained for over 10 ns. Therefore, we attributed this dynamics to a charge-transfer state which generally features long lifetime.^[34] Using ultra-violet photoelectron spectroscopy (UPS) measurement (Figure A3.9), the conduction band edge of FAPbI₃ CQD was determined to be -3.70 eV relative to vacuum level, which was shallower than that of ITIC (-3.83 eV versus vacuum level), which further confirmed the electron transfer from CQD to ITIC (**Figure 3.4d**).^[29,31]

Transient photovoltage (TPV) and photocurrent (TPC) measurements were carried out to further investigate the charge recombination and collection dynamics in devices. The TPV measurements

were performed at open-circuit condition, where majority of the photo-generated charges recombine, and the TPC measurement were performed under short circuit condition, where majority of the photo-generated charges are extracted. Pulsed photocurrent was generated by illuminating the devices with a 532 nm pulsed laser, and the data were fitted using a biexponential decay function. As shown in **Figure 3.4e**, the devices with ITIC exhibited an average photovoltage decay time constant of 754 μs , which was longer than that of the reference devices without ITIC (502 μs). We attributed the prolonged decay time to the presence of ITIC in CQD film that facilitated the charge separation at CQD/ITIC hetero-interface and thus reduced the carrier recombination. This observation was consistent with the phenomenon observed in photovoltaic devices showing a higher V_{oc} with ITIC. In TPC measurement (**Figure 3.4f**), the device with ITIC had a much shorter decay time constant of 3.2 μs compared to that of the reference device (6.4 μs), suggesting a faster carrier collection with ITIC.^[4,19] As shown in atomic force microscopic (AFM) images in Figure A3.9a and Figure A3.9d, CQD films with ITIC had similar morphology with that of reference sample, indicating that the effect of morphology on device performance was negligible. On the other hand, from the conductive AFM images shown in Figure A3.9, the CQD film showed higher conductivity after incorporation of ITIC under both room light (Figure A3.10b and e) and moderate illumination (Figure A3.10c and f). The increase in conductivity could be a result of the enhanced dot-to-dot coupling after the replacement of original insulating oleylamine and oleic acid ligands with the conjugated structured ITIC. This enabled better electron delocalization and thus improved transport within the CQD film increasing the charge collection efficiency of the device.^[26,35]

It is worth mentioning that our device configuration was carefully designed to maximize the function of ITIC in charge dynamics. Taking advantage of the layer-by-layer deposition process of CQD film, the distribution of ITIC in CQD film could be easily controlled, where ITIC was selectively incorporated into the part of CQD layers in the vicinity of the electron transporting layer (Figure A3.11a) rather than in the entire CQD layers (Figure A3.11b). For the device configuration where ITIC was added to all of the CQD layers, due to the direct contact of n-type ITIC with the p-type hole transporting layer, carriers extracted towards spiro-MeOTAD were more likely to recombine with electrons transferred to the ITIC, resulting in a much lower V_{oc} of 1.0 V, J_{sc} of 13.2 mA/cm², FF of 71.8%, PCE of 9.5% (Figure A3.11c).^[30,36] In contrast, with a controlled configuration shown in Figure A3.11a, ITIC was not distributed in the top layers that were close to hole transporting layer. Therefore, unfavorable contact between the spiro-MeOTAD and ITIC and thus carrier recombination could be strategically avoided, resulting in a much better device performance. The decrease in PCE of the device with ITIC only located at hole transporting layer side further supported this hypothesis (Figure A3.12). This also provides another indication of the role of ITIC as a ‘charge driver’ enabling the charge transfer from CQD to ITIC.

3.3 Conclusion

In conclusion, we have developed an effective strategy using a conjugated small molecule ITIC serving as a ‘charge driver’ designed to enhance the charge separation and as a result, improve the carrier dynamics and boost the device performance in FAPbI₃ CQDs solar cells. The ITIC was introduced into the FAPbI₃ CQDs film simultaneously while removing the original insulating surface ligands of the FAPbI₃ CQD. Taking advantage of the layer-by-layer deposition techniques in CQD photovoltaics fabrication, the distribution of ITIC in CQD film was strategically controlled

to boost the device efficiency up to 12.7%. Photo-physical studies unraveled that the formation of ITIC/FAPbI₃ CQD hetero-interface induce an effective charge transfer from the CQDs to ITIC, which in turn facilitated the charge separation, and thus reduced the carrier recombination and improved the carrier collection efficiency. Our results have provided a new route to improve the performance of perovskite CQD photovoltaic devices and shed light on the development of other CQD-based electronic devices.

Reference

- [1] G. H. Carey, A. L. Abdelhady, Z. Ning, S. M. Thon, O. M. Bakr, E. H. Sargent, *Chem Rev* **2015**, *115*, 12732.
- [2] B. Sun, O. Voznyy, H. Tan, P. Stadler, M. Liu, G. Walters, A. H. Proppe, M. Liu, J. Fan, T. Zhuang, J. Li, M. Wei, J. Xu, Y. Kim, S. Hoogland, E. H. Sargent, *Adv. Mater.* **2017**, *1700749*, 1700749.
- [3] C. R. Kagan, E. Lifshitz, E. H. Sargent, D. V. Talapin, *Science*. **2016**, *353*, aac5523.
- [4] Y. Wang, K. Lu, L. Han, Z. Liu, G. Shi, H. Fang, S. Chen, T. Wu, F. Yang, M. Gu, S. Zhou, X. Ling, X. Tang, J. Zheng, M. A. Loi, W. Ma, *Adv. Mater.* **2018**, *1704871*, 1704871.
- [5] O. E. Semonin, J. M. Luther, S. Choi, H. Y. Chen, J. Gao, A. J. Nozik, M. C. Beard, *Science*. **2011**, *334*, 1530.
- [6] M. C. Beard, *J Phys Chem Lett* **2011**, *2*, 1282.
- [7] Y. Yan, R. W. Crisp, J. Gu, B. D. Chernomordik, G. F. Pach, A. R. Marshall, J. A. Turner, M. C. Beard, *Nat. Energy* **2017**, *2*, 17052.
- [8] Q. A. Akkerman, G. Rainò, M. V Kovalenko, L. Manna, *Nat. Mater.* **2018**, *17*, 394.
- [9] M. V Kovalenko, L. Protesescu, M. I. Bodnarchuk, **2017**, *750*, 745.

- [10] H. Bian, D. Bai, Z. Jin, K. Wang, L. Liang, H. Wang, J. Zhang, Q. Wang, S. (Frank) Liu, *Joule* **2018**, 1.
- [11] A. Swamkar, A. R. Marshall, E. M. Sanehira, B. D. Chernomordik, D. T. Moore, J. A. Christians, T. Chakrabarti, J. M. Luther, *Science*. **2016**, 354, 92.
- [12] J. Xue, J. W. Lee, Z. Dai, R. Wang, S. Nuryyeva, M. E. Liao, S. Y. Chang, L. Meng, D. Meng, P. Sun, O. Lin, M. S. Goorsky, Y. Yang, *Joule* **2018**, 2, 1866.
- [13] E. M. Sanehira, A. R. Marshall, J. A. Christians, S. P. Harvey, P. N. Ciesielski, L. M. Wheeler, P. Schulz, L. Y. Lin, M. C. Beard, J. M. Luther, *Sci. Adv.* **2017**, 3, eaao4204.
- [14] G. Xing, N. Mathews, S. Sun, S. S. Lim, Y. M. Lam, M. Grätzel, S. Mhaisalkar, T. C. Sum, *Science*. **2013**, DOI 10.1126/science.1243167.
- [15] A. Miyata, A. Mitioglu, P. Plochocka, O. Portugall, J. T. W. Wang, S. D. Stranks, H. J. Snaith, R. J. Nicholas, *Nat. Phys.* **2015**, 11, 582.
- [16] H. C. Woo, J. W. Choi, J. Shin, S.-H. Chin, M. H. Ann, C.-L. Lee, *J. Phys. Chem. Lett.* **2018**, 9, 4066.
- [17] M. A. Faist, S. Shoaee, S. Tuladhar, G. F. A. Dibb, S. Foster, W. Gong, T. Kirchartz, D. D. C. Bradley, J. R. Durrant, J. Nelson, *Adv. Energy Mater.* **2013**, 3, 744.
- [18] Z. Yang, J. Z. Fan, A. H. Proppe, F. P. G. De Arquer, D. Rossouw, O. Voznyy, X. Lan, M. Liu, G. Walters, R. Quintero-Bermudez, B. Sun, S. Hoogland, G. A. Botton, S. O. Kelley, E. H. Sargent, *Nat. Commun.* **2017**, 8, 1.
- [19] Z. Sun, G. Sitbon, T. Pons, A. A. Bakulin, Z. Chen, *Sci. Rep.* **2015**, 5.
- [20] D. M. Balazs, M. A. Loi, *Adv. Mater.* **2018**, 30.
- [21] H. Aqoma, M. Al Mubarak, W. T. Hadmojo, E. H. Lee, T. W. Kim, T. K. Ahn, S. H. Oh, S. Y. Jang, *Adv Mater* **2017**, 29.

- [22] Y. Zhang, C. Ding, G. Wu, N. Nakazawa, J. Chang, Y. Ogomi, T. Toyoda, S. Hayase, K. Katayama, Q. Shen, *J. Phys. Chem. C* **2016**, *120*, 28509.
- [23] P. R. Brown, D. Kim, R. R. Lunt, N. Zhao, M. G. Bawendi, J. C. Grossman, V. Bulović, *ACS Nano* **2014**, *8*, 5863.
- [24] P. K. Santra, P. V. Kamat, *J. Am. Chem. Soc.* **2012**, *134*, 2508.
- [25] J. Wang, I. Mora-Seró, Z. Pan, K. Zhao, H. Zhang, Y. Feng, G. Yang, X. Zhong, J. Bisquert, *J. Am. Chem. Soc.* **2013**, *135*, 15913.
- [26] C. R. Kagan, C. B. Murray, *Nat. Nanotechnol.* **2015**, *10*, 1013.
- [27] M. Liu, O. Voznyy, R. Sabatini, F. P. García de Arquer, R. Munir, A. H. Balawi, X. Lan, F. Fan, G. Walters, A. R. Kirmani, S. Hoogland, F. Laquai, A. Amassian, E. H. Sargent, *Nat. Mater.* **2017**, *16*, 258.
- [28] L. M. Wheeler, E. M. Sanehira, A. R. Marshall, P. Schulz, M. Suri, N. C. Anderson, J. A. Christians, D. Nordlund, D. Sokaras, T. Kroll, S. P. Harvey, J. J. Berry, L. Y. Lin, J. M. Luther, *J. Am. Chem. Soc.* **2018**, *140*, 10504-10513.
- [29] Y. Lin, J. Wang, Z.-G. Zhang, H. Bai, Y. Li, D. Zhu, X. Zhan, *Adv. Mater.* **2015**, *27*, 1170.
- [30] Y. Wu, X. Yang, W. Chen, Y. Yue, M. Cai, F. Xie, E. Bi, A. Islam, L. Han, *Nat. Energy* **2016**, *1*, 1.
- [31] T. Niu, J. Lu, R. Munir, J. Li, D. Barrit, X. Zhang, H. Hu, Z. Yang, A. Amassian, K. Zhao, S. F. Liu, *Adv. Mater.* **2018**, *30*, 1.
- [32] H. Bin, L. Gao, Z. G. Zhang, Y. Yang, Y. Zhang, C. Zhang, S. Chen, L. Xue, C. Yang, M. Xiao, Y. Li, *Nat. Commun.* **2016**, *7*, 13651.
- [33] Y. Lin, F. Zhao, S. K. K. Prasad, J. De Chen, W. Cai, Q. Zhang, K. Chen, Y. Wu, W. Ma, F. Gao, J. X. Tang, C. Wang, W. You, J. M. Hodgkiss, X. Zhan, *Adv. Mater.* **2018**, *30*,

1706363.

- [34] J. Liu, S. Chen, D. Qian, B. Gautam, G. Yang, J. Zhao, J. Bergqvist, F. Zhang, W. Ma, H. Ade, O. Inganäs, K. Gundogdu, F. Gao, H. Yan, *Nat. Energy* **2016**, *1*, 16089.
- [35] Q. Wang, Z. Jin, D. Chen, D. Bai, H. Bian, J. Sun, G. Zhu, G. Wang, S. F. Liu, *Adv. Energy Mater.* **2018**, *1800007*, 1800007.
- [36] P. Cheng, R. Wang, J. Zhu, W. Huang, S.-Y. Chang, L. Meng, P. Sun, H.-W. Cheng, M. Qin, C. Zhu, X. Zhan, Y. Yang, *Adv. Mater.* **2018**, *30*, 1705243.

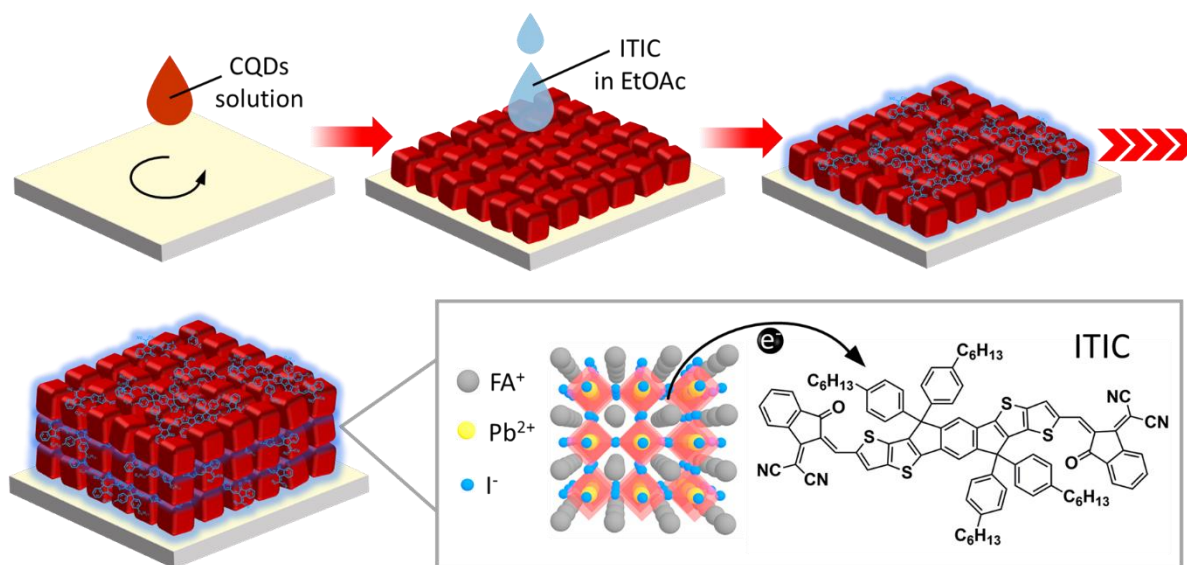


Figure 3.1 Schematic diagram of FAPbI₃CQD/ITIC film fabrication (insert: chemical structure of ITIC)

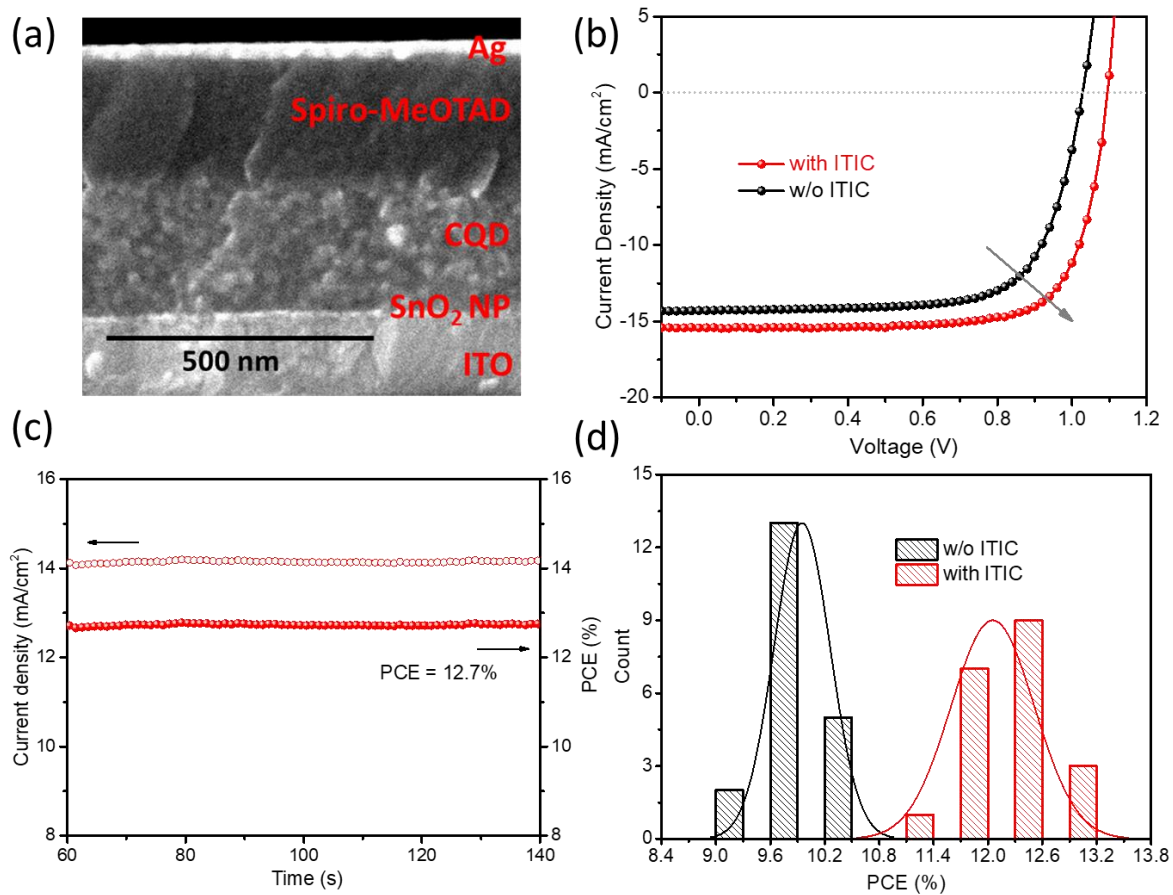


Figure 3.2 a) A cross-sectional SEM image of the device structure. b) *J-V* curves of the devices based on FAPbI₃ CQDs with and without ITIC. c) Steady-state power conversion efficiency measurement of the device with ITIC. d) Distribution of PCEs measured from 40 solar cell devices.

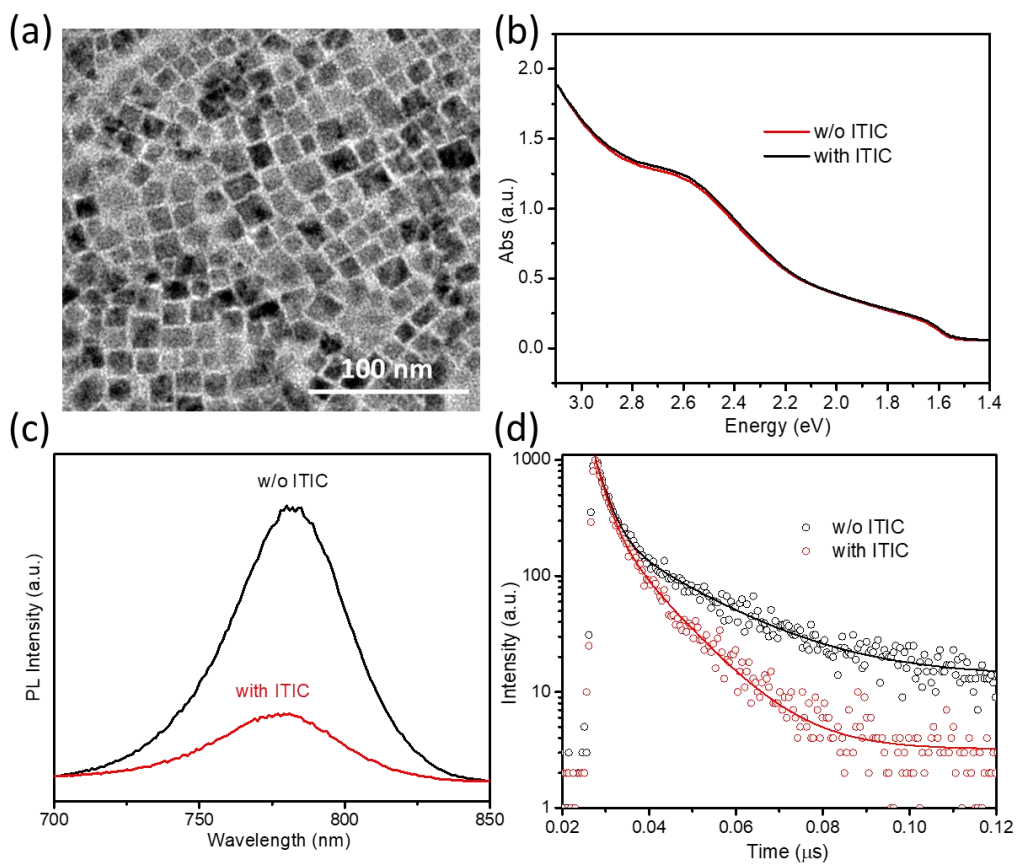


Figure 3.3 a) Transmission electron microscopic (TEM) image of as-synthesized FAPbI₃ CQDs. b) UV-visible absorption, c) steady-state photoluminescence (open circles indicate measured data while solid lines are fitted curves), and d) TRPL spectra of FAPbI₃ CQDs with (red) and without (black) ITIC.

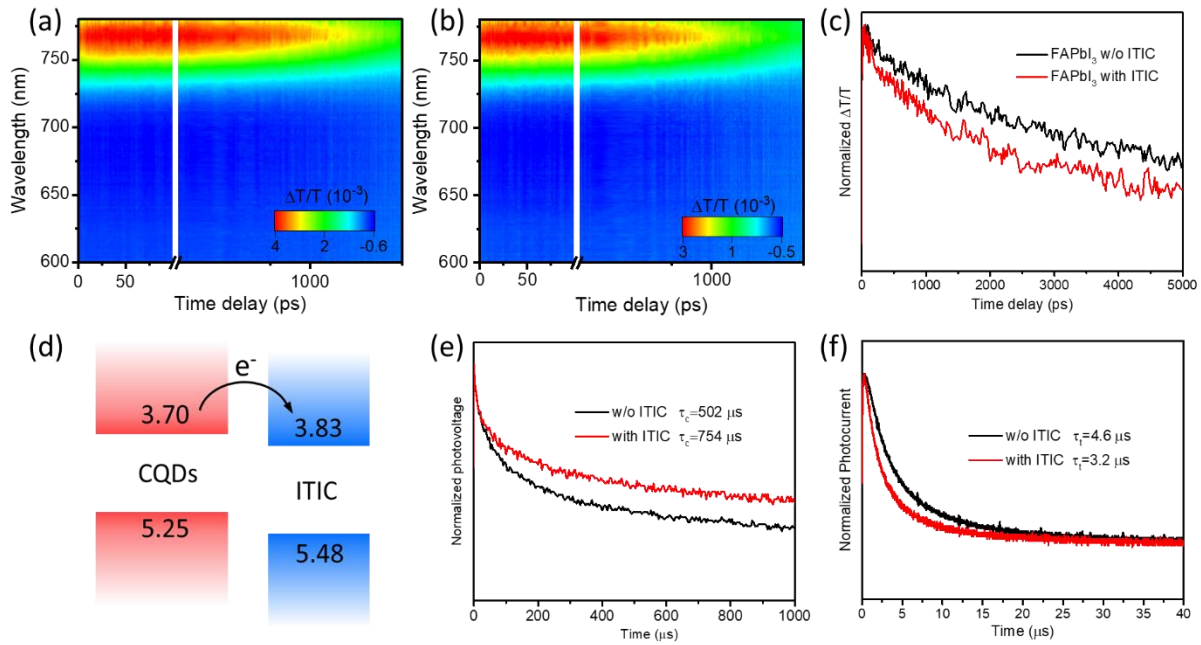


Figure 3.4 TA spectra of FAPbI₃ CQD film a) without and b) with ITIC (excitation power was 4 μ J/cm²). c) The dynamic of bleaching peak probed at ~770 nm of FAPbI₃ CQDs with and without ITIC. d) Schematic energy diagram showing charge transfer between FAPbI₃ CQDs and ITIC. e) TPV and f) TPC measurements of devices with and without ITIC.

Chapter 4 Crystalline Liquid-like Behavior: Surface-Induced Secondary Grain Growth of Photovoltaic Perovskite Thin Film

Surface effects play a dominant role in regulating the properties of a solid when the size reaches the nanoscale regime¹⁻⁴. For micron or submicron thin films, which are the most commonly employed thicknesses in microelectronics industry, the surface effect on the internal properties of the entire film will usually be negligible. However, for “soft” matters such as polymers, or taking the extreme, liquids, due to their highly deformable or flowable character, they can be highly responsive to an external field, upon which the depth scale affected by the surface can dramatically increase to the microscale or even larger⁵⁻⁷. Halide perovskite semiconductor materials were recently reported to be inherently “soft”-structured⁸⁻¹¹, which can be described as a crystalline liquid with both crystalline solid and liquid-like behaviors. The soft nature of halide perovskites offers the possibility of regulating their micron-scale thin film behavior via a simple tuning of surface features. Among typical industrial electronic device fabrication techniques, secondary grain growth is a powerful strategy for the fabrication of polycrystalline thin films with grain sizes much larger than the film thickness or even towards single crystal thin films¹²⁻¹⁶. The resulting reduced grain boundaries not only improve the electronic or photoelectronic behavior but also suppress device degradation pathways resulting from grain boundaries¹⁷⁻²⁰. The driving force (ΔF) of secondary grain growth stems from the existence of one or a set of crystallographic textures that minimize the surface free energy such that the grains will grow larger along the orientation to minimize the free energy of the system, which is shown below¹³:

$$\Delta F = F_f - F_i = -\frac{2(\Delta\gamma)}{h} + \frac{\beta\gamma_{gb}}{r}$$

where F_i and F_f is the energy per unit volume before and after the secondary grain growth, respectively; $\Delta\gamma$ is defined as surface energy anisotropy ($\bar{\gamma} - \gamma_{min}$); h is the film thickness; β is a geometric factor (typically equals to 0.85 when using a cylinder geometry model); γ_{gb} is an average grain boundary energy per unit area. The state-of-art techniques for secondary grain growth commonly involve harsh and complicated conditions, such as elevated and/or cyclic temperature annealing, chemical doping, and high-pressure plastic straining, to obtain the driving force to trigger grain boundary migration²¹⁻²⁵. The “soft” liquid-like nature of perovskite offers a way to take advantage of the surface effect on the inner film properties for secondary grain growth. Hence, here we demonstrate a surface-induced secondary grain growth (SISG) technique, where surface modification induces post-crystallization grain growth in the entire perovskite thin film. This strategy sheds light on a new perspective for the perovskite research community, offering a novel methodology for property manipulation of perovskite thin films: changing the surface can induce the property evolution of the perovskite thin film as a whole.

4.1 Theoretical modeling of the driving force

For investigation of SISG in perovskite thin films, we chose the CsPbI₂Br perovskite as a model compound, since it is a relatively pure and simple system that contains only inorganic components. Organic components were left out because they will interfere with the elemental analysis and add complexity to the study of chemical interactions in the system, which will obfuscate the investigation of the underlying mechanism. Furthermore, compared with the pure iodine-based CsPbI₃ perovskite, CsPbI₂Br shows an enhanced phase stability rendering it more promising towards commercialization. For surface manipulation, we chose three organic ammoniums with

varying carbon lengths, i.e. n-butylammonium (BA), octyl ammonium (OCA), and oleylammonium (OLA), all of which potentially can lower the surface energy of the perovskite (100) plane when anchored to the void of the corner-sharing PbI_6^{4-} octahedron. I first used density functional theory (DFT) to examine the surface energies of the organic ammonium terminated low-index planes of the perovskite based on a slab model (**Fig. 4.1** and Table B4.1. The detailed calculation method can be found in the Supporting Information). The surface free energies of the Cs, BA, OCA, and OLA-terminated (111) planes were found to be similar, while those of (100) plane were determined to be 4.30, 3.23, 2.14, and 1.97 eV/nm², respectively. The surface energy differences between (100) and (111) planes are summarized in Fig. A4.1, demonstrating an increasing surface energy anisotropy in the following order: Cs, BA, OCA, and OLA. This indicated a corresponding increasing driving force for the secondary grain formation.

4.2 Characterizations of the grain growth and film properties

Following theoretical predictions, the three organic ammoniums were evaluated in the preparation of perovskite films via a sequential two-step procedure. CsPbI_2Br perovskite film was fabricated using a one-step method consisting of spin-coating $\text{PbI}_2/\text{PbBr}_2/\text{CsI}$ mixed perovskite precursors on the substrate followed by annealing at 300 °C for 10 min. The substrate was then cooled down to room temperature, yielding black perovskite thin film, which indicates the formation of the CsPbI_2Br cubic phase. For the targeted film, an ammonium iodide isopropanol solution was subsequently spin-coated onto the crystallized perovskite thin film followed by heating to 100 °C for 5 min to remove the excess solvent. For the reference film, pure isopropanol was spin-coated onto perovskite film followed by the same annealing process as the organic ammoniums to examine the effect of isopropanol and heat. The scanning electron microscopy (SEM) images of the

fabricated films are shown in **Fig. 4.2A**. Crystal grains in the reference film were of almost the same size as the ones in the as-fabricated film without any post treatment (Fig. A4.2), indicating that isopropanol and heat did not induce the grain growth of perovskite. However, films that underwent surface treatment using organic ammoniums showed much enlarged grains. The average grain sizes of films with different post-treatment conditions shown in Fig. 4.2B are 769 nm, 1277 nm, 1287 nm, and 1846 nm for reference, BA, OCA and OLA, respectively. I attribute this secondary grain growth process to the decrease in surface energy of a crystal facet that provides the driving force of surface anisotropy $\Delta\gamma$. On the one hand, the grain had an orientation, *i.e.* plane (100), that could minimize the surface energy of the film due to the existence of the organic ammonium on the surface. On the other hand, the low activation barrier of ion diffusion in perovskite facilitated by soft lattice modes can facilitate the grain boundaries rearrangement during the out-of-plane crystalline reorientation process (the orientation will be further discussed in detail)¹⁰. From another aspect, the highly anharmonic lattice with low-frequency modes and small elastic modulus renders the perovskite highly “flowable” and, thus, highly responsive to the influence from the surface^{10,26}. Thus, the original perovskite grains were able to grow further in that favorable direction to reduce the energy of the whole system (Fig. 4.2C). The lower the surface energy, the larger the grain could grow. As a result, OLA, which gave the lowest surface energy, induced secondary grain growth with the largest resulting average grain size of up to 4 μm (Fig. A4.3). Multi-phase field model was also employed to simulate the grain growth for the film with and without OLA, which showed a significant increase of the grain size for the film with OLA (Fig. A4.4). This demonstrates that SISG is a powerful strategy towards precise control of perovskite grain size or even perovskite single crystal thin film given that the surface energy is rationally manipulated.

In situ real time Grazing-Incidence Wide-Angle X-ray Scattering (GIWAXS) was performed to obtain an in-depth insight into the SISG of the perovskite thin film. The X-ray diffraction signal measurement was initiated once the organic ammonium isopropanol solution was drop-cast onto the pristine perovskite thin film triggering the SISG (Fig. A4.5). **Fig. 4.3A** shows the time-dependent diffraction peak evolution at q_z value of around 10 nm^{-1} , which is a characteristic peak corresponding to the (100) plane of the cubic phase of perovskite ²⁷. During the SISG process, the peak position gradually shifted to a lower q_z value, indicating a gradual decrease in lattice constant that possibly results from the strain relaxation during the grain growth. The initial peak splitting phenomenon can be attributed to the partial halide segregation in perovskite, which was commonly observed in the CsPbI₂Br film ²⁸. At a later stage, the dual-peak behavior gradually disappeared, suggesting that the SISG that caused the strain relaxation, as well as, better crystallinity of the secondary perovskite grains, might also suppress the halide segregation, which could be beneficial to the long-term stability of the perovskite device (more details will be provided in the device description part) ²⁸. Such phenomenon was not observed in the reference film eliminating the effect of solvent and heat on the grain size growth in the perovskite film (Fig. A4.6). Fig 4.3B and 4.3C show the two-dimensional GIWAXS patterns of the perovskite film with and without SISG, respectively. The azimuth angle plots in Fig. 4.3D were obtained from the patterns by cutting along the (100) plane of the perovskite films. At the azimuth angle of 90° , the perovskite film with SISG showed a very sharp peak with a half peak width of 9.30° , much lower than that of the reference film (10.66°), demonstrating that SISG produced a more preferred out-of-plane orientation of the secondary perovskite grains. This is consistent with the growth mechanism we proposed earlier suggesting that the presence of organic ammonium on the surface lowers the surface energy of the

(100) plane of perovskite and generates a driving force for the grain growth in that direction to minimize the energy of the system. High-resolution X-ray photoelectron spectroscopy (XPS) patterns of the Pb 4f of the reference and targeted films are shown in Fig. 4.3E. For the targeted film, two main peaks located at 138.14 and 143.00 eV were observed corresponding to the Pb 4f_{7/2} and Pb 4f_{5/2}, respectively. For comparison, the reference film showed two main peaks at 138.76 and 143.42 eV. The peaks from Pb 4f shifted to higher binding energies in the film after the SISG process based on OLA, indicating the interaction between organic ammonium on the surface and the Pb in the perovskite lattice²⁹. The spatial distribution of OLA in the perovskite film with SISG was characterized by time-of-flight secondary-ion mass spectrometry (TOF-SIMS) with a device structure of ITO/SnO₂/perovskite/MoO_x/Au. As shown in Fig. 4.3F, the C and N profiles, which are the characteristic signals of OLA, exhibited a very narrow distribution (similar to the depth profile of Mo) with little overlap with the depth profile of Pb, which is a representative signal of perovskite. This signifies the existence of OLA only on the surface of the perovskite. The resulting organic ammonium-terminated perovskite film with SISG was further confirmed to have a lower surface energy (38.38 mN/m) than the reference film (59.78 mN/m) via contact angle measurements (Fig. A4.7, and Table B4.2). In order to further evaluate the perovskite film quality, the X-ray diffraction patterns of the perovskite film after the SISG process based on OLA were obtained (Fig. A4.8). They exhibited much higher peak intensity than that of the reference, suggesting enhanced crystallinity of the secondary perovskite grains. UV-Vis absorption spectrum (Fig. A4.9) demonstrates that the perovskite film with SISG showed higher absorption than the reference, which can be attributed to the enlarged grain sizes and thus enhanced light scattering³⁰. The perovskite film after the SISG process exhibits much improved film quality necessary for enhancing the device performance.

4.3 Device performance and stability

I further assessed the photovoltaic performance of the perovskite films prepared with and without the SISG process by fabricating devices with the ITO/SnO₂/perovskite/PTAA/Au configuration, wherein PTAA refers to poly[bis(4-phenyl)(2,4,6-trimethylphenyl) amine]. Current density-voltage (*J-V*) curves of the photovoltaic devices with and without SISG are compared in **Fig. 4.4A**, in which the highest power conversion efficiency (PCE) of the target device reached 16.58% with negligible hysteresis (open circuit voltage (*V*_{OC}): 1.23 V, short circuit current (*J*_{SC}): 16.85 mA cm⁻², fill factor (FF): 0.80), while a PCE of only 13.09% was achieved with the control device (*V*_{OC}: 1.11 V, *J*_{SC}: 15.32 mA cm⁻², FF: 0.77). To the best of our knowledge, this is the highest PCE reported in the CsPbI₂Br system. External quantum efficiency (EQE) spectra of the devices were compared in Fig. A4.10A. An integrated *J*_{SC} of 16.44 mA cm⁻² from the target device matched well with the value measured from the *J-V* scan (<5% discrepancy), while a control device showed an integrated *J*_{SC} of 14.98 mA cm⁻². A stabilized PCE of 16.04% was achieved with the target device when biased at 1.06 V, while that of the control device was 12.36% when biased at 0.94 V (Fig. A4.10B). The remarkably enhanced *V*_{OC} (by up to 0.12 V) in the device based on SISG can be attributed to the enlarged grain size and, thus, decreased grain boundaries, which usually provide a non-radiative recombination pathway for the carriers due to trap states^{20,31}. This is consistent with the transient photovoltage measurements (TPV) under open circuit condition. As shown in Fig. 4.4B, the device based on SISG exhibited a photovoltage decay time constant of 2.16 ms, which was longer than that of the reference device (1.31 ms), indicating less non-radiative recombination sites³². In addition, electrochemical impedance spectroscopy (EIS) characterization was performed to demonstrate the carrier transport processes under illumination at the interface (Fig. 4.4C). The middle frequency zone of the EIS semicircle should be dominated by the junction capacitance and

recombination resistance related to the interfaces between the transport materials and the perovskite. According to Fig. 4.4C, the SISG-based device has a smaller impedance than that of the reference, signifying a substantial suppressed recombination at the interface, which most probably originates from the preferred orientation of the perovskite secondary grains that enable improved carrier flow between perovskites and carrier transport layers³³. Moreover, the hydrophobic tails of the OLAs on the surface of the perovskite could enhance the compatibility of the surface with the upper layer, PTAA, resulting in a better interfacial contact. The improved carrier dynamics can also be reflected in the measurement of transient photocurrent decay. As shown in Fig. 4.4D, the device with SISG had a shorter decay time constant of 0.91 μs compared to that of the reference device (1.23 μs), suggesting a faster carrier collection efficiency, which is consistent with the improved J_{SC} in the targeted device³².

Not only does the photovoltaic efficiency significantly benefit from the SISG strategy, but also the device stability showed remarkable improvement in all aspects, including thermal stability, phase stability and, thus, operational stability. In Fig. 4.4E, the changes in PCE of the unencapsulated devices in a nitrogen atmosphere at 85 °C were tracked over time to test the long-term thermal stability. While the reference device degraded by 30% in 500 h, the target device maintained 90% of its initial efficiency during this time. Although the all-inorganic perovskite has been reported to show superior thermal and light stability to that of their organic-inorganic counterparts, it is well-known to suffer from a rapid phase transition to the non-perovskite phase, especially when exposed to moisture in ambient atmosphere²⁸. However, the phase stability of the device based on SISG was noticeably enhanced, maintaining over 90% of its original PCE when stored under ambient conditions with 20-30% humidity at 25 °C for 4000 h. In contrast, the reference device lost >50%

of its initial efficiency within 900 h (Fig. 4.4F). The operational stability of the devices was also compared in Fig. 4G. The reference device underwent fast degradation, while the device based on SISG maintain >90% of its initial efficiency over the course of 1000 h. Generally, we attribute the dramatically improved stability to two factors resulting from the SISG processing. On the one hand, high-quality perovskite films with reduced grain boundaries and higher crystallinity suppresses the degradation pathways either through grain boundaries or ion migration, which is also one of the motivations towards single crystal perovskite thin films³⁴. On the other hand, the hydrophobic nature of the small molecules shields the interface from moisture. Therefore, the SISG strategy demonstrates a good example of the possibility to affect and regulate the properties of the entire thin film by tuning of surface states. The surface agents can play a dual functional role of enabling the evolution of the underlying film properties and regulating the interface at the same time to produce improved interfacial contact with the upper layer and thus enabling improvement in both device performance and stability.

To demonstrate the universality of this strategy, we further applied it to the organic-inorganic hybrid perovskite system. As shown in Fig. A4.11, the post-treatment of OLA can induce the secondary grain growth in the formamidinium (FA)-based perovskite thin film as well. The surface energies of the low-index planes of FA-based perovskite with and without OLA were investigated computationally to confirm that the (100) plane became more energy favorable after the surface treatment (Fig. A4.12). The resulted photovoltaic devices showed an improved PCE from 20.04% to 22.13% (Fig. A4.13).

4.4 Conclusion

The demonstration of surface-state-tuning enabling secondary grain growth over the entire perovskite thin film sheds light on a new research angle in the area of perovskite thin films in regard to surface states by taking advantage of the unique soft nature of perovskites. In contrast to the widely reported strategies of regulating the properties of perovskite thin films via composition tuning, additive incorporation, solvent engineering and so on, a new methodology basis is proposed: changing the surface is a powerful tool to induce the property evolution of the entire perovskite thin film. Since the surface treatment process is after the formation of the perovskite film, it strategically avoids the limitation of conventional methods in choosing agents/additives that are appropriate with high annealing temperatures of crystallization. Additionally, many of the additives incorporated into perovskite precursors to control the nucleation/growth kinetics, which is often a requirement for high quality films, always serve as a carrier recombination or degradation centers due to the heterogeneous microstructure. In contrast, the surface agents that did not penetrate into the perovskite bulk film will not induce the formation of these undesirable centers within the perovskite film. Furthermore, the surface agents provide a versatile platform to tune the interface between the perovskite film and the top layer, which can be regarded as a bi-functional interfacial agent. On the one hand, they induce the evolution of the perovskite layer at the bottom, and on the other hand, they serve as an interconnecting layer that improves the contact with the upper layer. Moreover, the utilization of our methodology does not have to be limited to mechanical properties, in which perovskites exhibit low elastic modulus as a reflection of their “soft” nature as demonstrated in this report. I expect the reach of this strategy to extend to the properties in all aspects, such as electronic properties, in which perovskites exhibit low electric modulus rendering them highly vulnerable to an electric field ³⁵. A possible example might be introducing surface

dipoles to modify the internal electric field and, thus, change the energy levels/band structures of the thin films as a whole. Hence, we hope this strategy will provide a new direction towards high-quality perovskite thin films with tunable and desirable properties and pave the way to the commercialization of perovskite photoelectric devices.

References

1. Boles, M. A., Ling, D., Hyeon, T. & Talapin, D. V. The surface science of nanocrystals. *Nature Materials* **15**, 141–153 (2016).
2. Carey, G. H. *et al.* Colloidal Quantum Dot Solar Cells. *Chem Rev* **115**, 12732–12763 (2015).
3. Milliron, D. J. Quantum dot solar cells: The surface plays a core role. *Nat. Mater.* **13**, 772–773 (2014).
4. Diao, J., Gall, K. & Dunn, M. L. Surface-stress-induced phase transformation in metal nanowires. *Nat. Mater.* **2**, 656–660 (2003).
5. Ding, Y., Niu, X. R., Wang, G. F., Feng, X. Q. & Yu, S. W. Surface effects on nanoindentation of soft solids by different indenters. *Mater. Res. Express* **3**, (2016).
6. Thomas Brunet, Jacques Leng, O. M.-M. Soft Acoustic Metamaterials. *Science (80-.)*. **342**, 323–324 (2013).
7. Xu, X. *et al.* Gravity and surface tension effects on the shape change of soft materials. *Langmuir* **29**, 8665–8674 (2013).
8. Zhu, H. *et al.* Screening in crystalline liquids protects energetic carriers in hybrid perovskites. *Science (80-.)*. **353**, 1409–1413 (2016).

9. Joshi, P. P., Maehrlein, S. F. & Zhu, X. Dynamic Screening and Slow Cooling of Hot Carriers in Lead Halide Perovskites. *Adv. Mater.* **1803054**, 1–10 (2019).
10. Lai, M. *et al.* Intrinsic anion diffusivity in lead halide perovskites is facilitated by a soft lattice. *Proc. Natl. Acad. Sci.* **115**, 201812718 (2018).
11. Miyata, K., Atallah, T. L. & Zhu, X. Y. Lead halide perovskites: Crystal-liquid duality, phonon glass electron crystals, and large polaron formation. *Science Advances* **3**, e1701469 (2017).
12. Omori, T. *et al.* Abnormal grain growth induced by cyclic heat treatment. *Science* (80-.). **341**, 1500–1502 (2013).
13. Thompson, C. V. Secondary grain growth in thin films of semiconductors: Theoretical aspects. *J. Appl. Phys.* (1985). doi:10.1063/1.336194
14. Ye, Z. G. *Handbook of Advanced Dielectric, Piezoelectric and Ferroelectric Materials: Synthesis, Properties and Applications. Handbook of Advanced Dielectric, Piezoelectric and Ferroelectric Materials: Synthesis, Properties and Applications* (2008). doi:10.1533/9781845694005
15. Thompson, C. V. Grain Growth in Thin Films. *Annu. Rev. Mater. Sci.* (1990). doi:10.1146/annurev.ms.20.080190.001333
16. Kang, S.-J. L. *Sintering: Densification, Grain Growth, and Microstructure. Sintering* (2005). doi:http://dx.doi.org/10.1016/B978-075066385-4/50009-1
17. Adam W. Tsen, Lola Brown, Mark P. Levendorf, Fereshte Ghahari, Pinshane Y. Huang, Robin W. Havener, Carlos S. Ruiz-Vargas, David A. Muller, Philip Kim, J. P. Tailoring

- Electrical Transport Across Grain Boundaries in Polycrystalline Graphene. *Science*. **336**, 1143–1146 (2012).
18. Seager, C. H. & Ginley, D. S. Passivation of grain boundaries in polycrystalline silicon. *Appl. Phys. Lett.* **34**, 337–340 (1979).
 19. Liu, Y. *et al.* Thinness- and Shape-Controlled Growth for Ultrathin Single-Crystalline Perovskite Wafers for Mass Production of Superior Photoelectronic Devices. *Adv. Mater.* **28**, 9204–9209 (2016).
 20. Son, D. Y. *et al.* Self-formed grain boundary healing layer for highly efficient CH₃NH₃PbI₃ perovskite solar cells. *Nat. Energy* **1**, 16081 (2016).
 21. Thompson, C. V. Structure Evolution During Processing of Polycrystalline Films. *Annu. Rev. Mater. Sci.* (2000). doi:10.1146/annurev.matsci.30.1.159
 22. Miller, D. L. *et al.* Giant secondary grain growth in Cu films on sapphire. *AIP Adv.* (2013). doi:10.11646/phytotaxa.311.2.4
 23. Palmer, J. E., Thompson, C. V. & Smith, H. I. Grain growth and grain size distributions in thin germanium films. *J. Appl. Phys.* (1987). doi:10.1063/1.339460
 24. Ciulik, J. & Taleff, E. M. Dynamic abnormal grain growth: A new method to produce single crystals. *Scr. Mater.* **61**, 895–898 (2009).
 25. Omori, T. *et al.* Abnormal grain growth induced by cyclic heat treatment. *Science* (80-.). **341**, 1500–1502 (2013).
 26. Ferreira, A. C. *et al.* Elastic Softness of Hybrid Lead Halide Perovskites. *Phys. Rev. Lett.* **121**, (2018).

27. Nam, J. K., Chun, D. H., Rhee, R. J. K., Lee, J. H. & Park, J. H. Methodologies toward Efficient and Stable Cesium Lead Halide Perovskite-Based Solar Cells. *Advanced Science* **5**, 1800509 (2018).
28. Zeng, Q. *et al.* Inorganic CsPbI₂Br Perovskite Solar Cells: The Progress and Perspective. *Sol. RRL* **3**, 1800239 (2018).
29. Liu, L. *et al.* Grain-Boundary “Patches” by In Situ Conversion to Enhance Perovskite Solar Cells Stability. *Adv. Mater.* **30**, 1800544 (2018).
30. Im, J. H., Jang, I. H., Pellet, N., Grätzel, M. & Park, N. G. Growth of CH₃NH₃PbI₃ cuboids with controlled size for high-efficiency perovskite solar cells. *Nat. Nanotechnol.* **9**, 927–932 (2014).
31. Niu, T. *et al.* Stable High-Performance Perovskite Solar Cells via Grain Boundary Passivation. *Adv. Mater.* **30**, 1706576 (2018).
32. Meng, L. *et al.* Tailored phase conversion under conjugated polymer enables thermally stable perovskite solar cells with efficiency exceeding 21%. *J. Am. Chem. Soc.* (2018). doi:10.1021/jacs.8b10520
33. Zheng, G. *et al.* Manipulation of facet orientation in hybrid perovskite polycrystalline films by cation cascade. *Nat. Commun.* **9**, 2793 (2018).
34. Shao, Y. *et al.* Grain boundary dominated ion migration in polycrystalline organic-inorganic halide perovskite films. *Energy Environ. Sci.* **9**, 1752–1759 (2016).
35. Huang, J., Yuan, Y., Shao, Y. & Yan, Y. Understanding the physical properties of hybrid perovskites for photovoltaic applications. *Nature Reviews Materials* **2**, (2017).

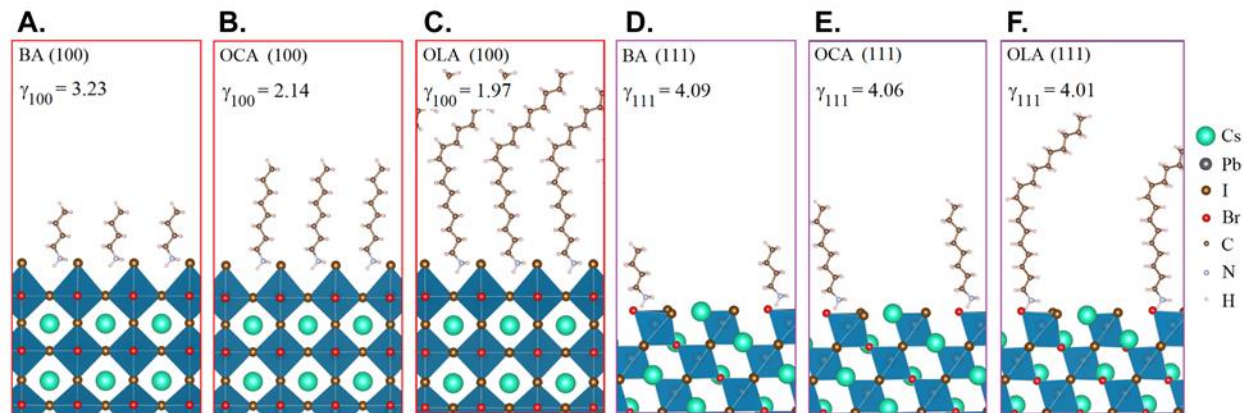


Fig. 4.1 The effect of organic ammoniums on surface servicing as the driving force of surface induced secondary grain growth.

Optimized (100) slab model of perovskite with (A) BA, (B) OCA, (C) OLA termination by DFT-D3 method; Optimized (111) slab model of perovskite with (D) BA, (E) OCA, (F) OLA termination by DFT-D3 method.

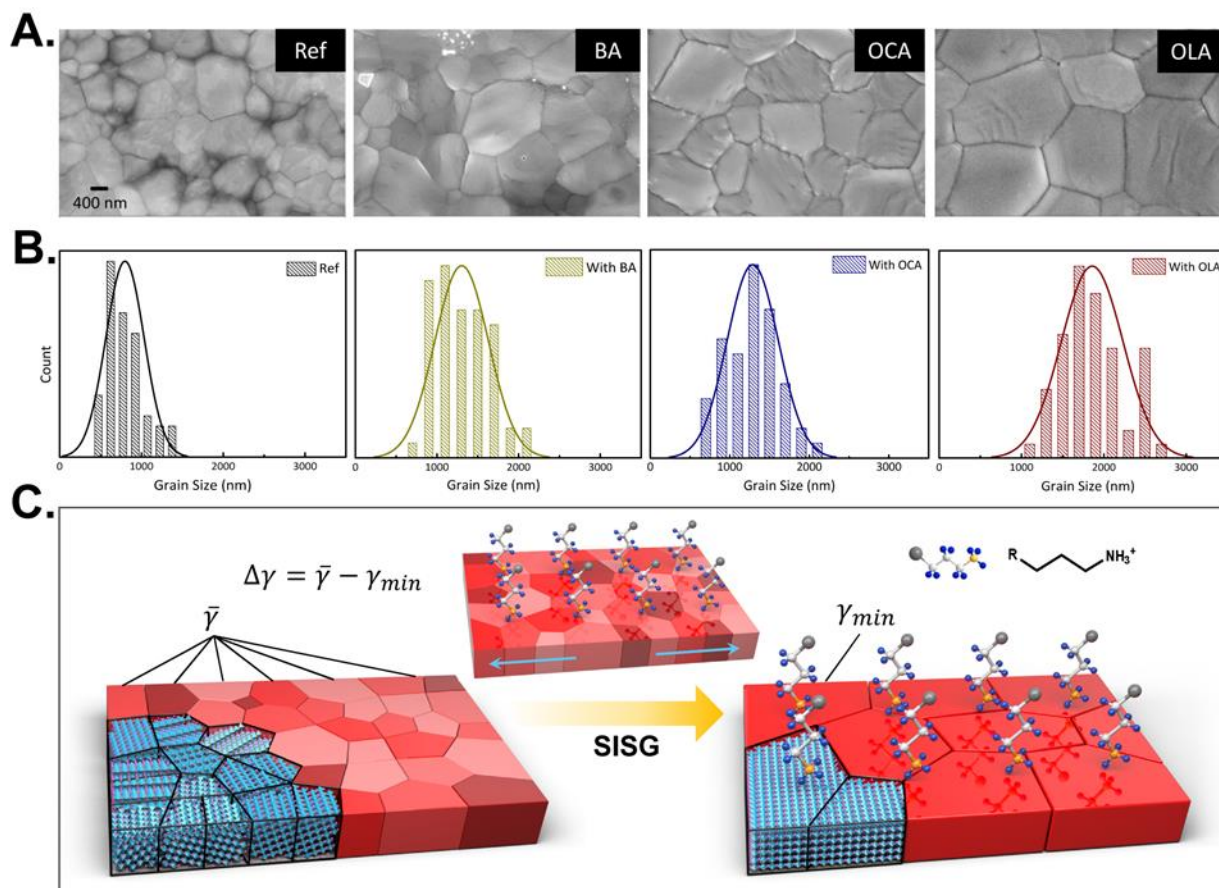


Fig. 4.2 Demonstration of the surface induced secondary grain growth.

- (A) Top-view SEM images of perovskite film with various treatments (IPA, BA, OCA and OLA).
 (B) Grain size statistical distribution of perovskite films with various treatments (IPA, BA, OCA and OLA).
 (C) Schematic demonstration of the process of surface induced secondary grain growth.

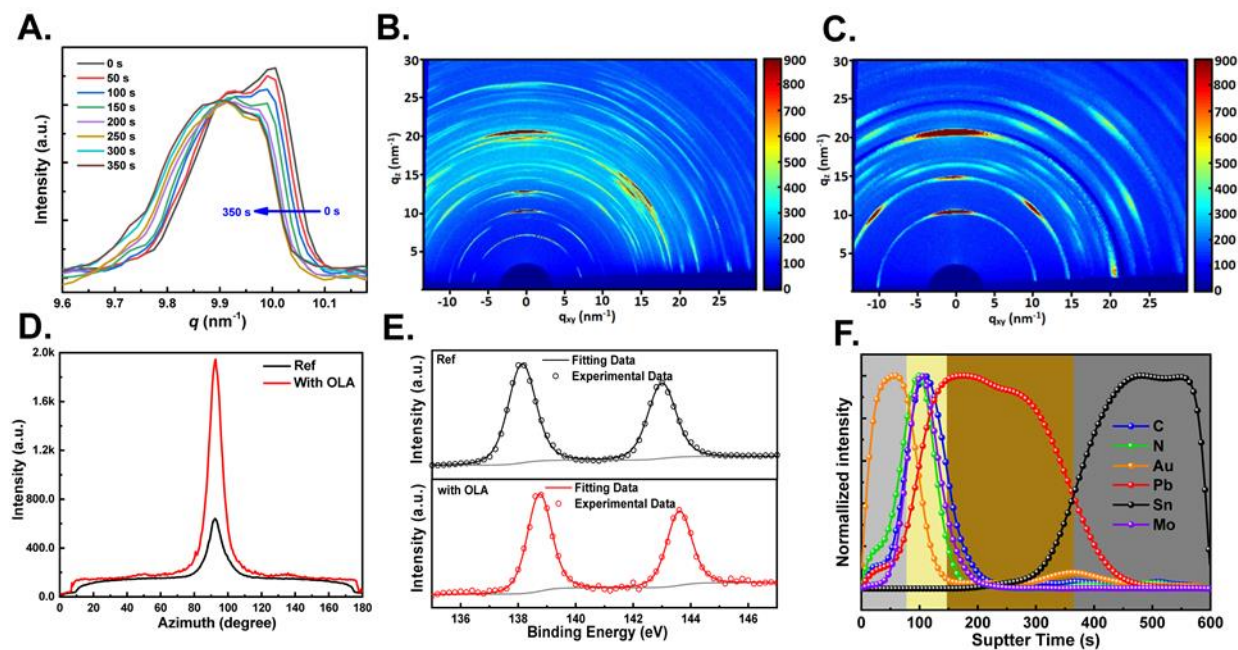


Fig. 4.3 Characterization of Perovskite film with the surface induced secondary grain growth by OLA.

(A) Evolution of the (100) peak position of perovskite film with OLA extracted from real-time in-situ GIWAXS measurement. (B and C) 2D GIWAXS patterns of perovskite films (B) without OLA treatment and (C) with OLA treatment. (D) Radially integrated intensity plots along (100) crystal plane from the 2D GIWAXS patterns in perovskite films with or without OLA treatment. (E) XPS data for Pb 4f 7/2 and Pb 4f 5/2 core level spectra in perovskite films with or without OLA treatment. (F) Time-of-flight secondary ion mass spectroscopy (TOF-SIMS) depth profile of perovskite film with OLA treatment.

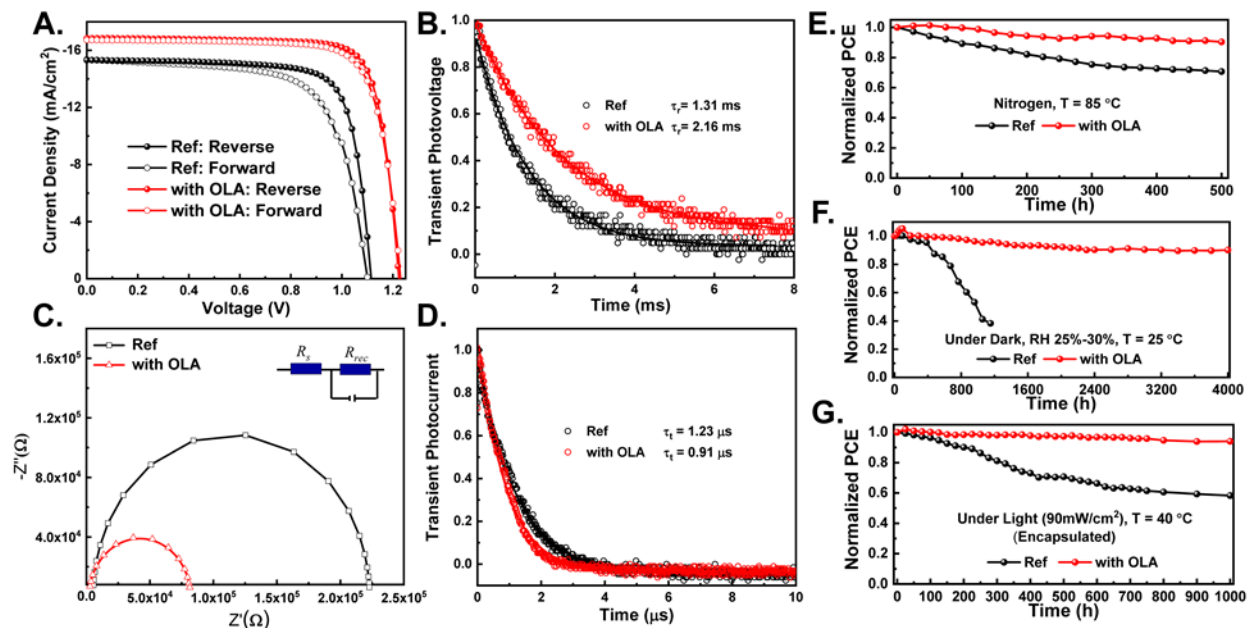


Fig. 4.4 Enhanced photovoltaic performance and long-term stability of perovskite film with surface induced secondary grain growth by OLA.

(A) Current density–voltage (J – V) curves of perovskite solar cells with or without OLA treatment. (B) Normalized transient photovoltage decay of perovskite solar cells with or without OLA treatment. (C) Nyquist plots of perovskite solar cells with or without OLA treatment measured in the dark and at corresponding open-circuit voltages. (D) Normalized transient photocurrent decay of perovskite solar cells with or without OLA treatment. (E) Evolution of power conversion efficiency (PCE) of perovskite solar cells with or without OLA treatment. The devices were stored under nitrogen with controlled temperature (85 °C). (F) Evolution of power conversion efficiency (PCE) of perovskite solar cells with or without OLA treatment. The devices were stored under dark with controlled humidity. (G) Evolution of the PCEs measured from the encapsulated perovskite solar cells with or without OLA treatment exposed to continuous light ($90 \pm 5 \text{ mW cm}^{-2}$) under open-circuit condition.

Chapter 5 Constructive molecular configurations for surface-defect passivation of perovskite photovoltaics

Metal-halide perovskite has emerged as a promising photovoltaic absorber due to its intriguing optoelectronic properties.^(1–5) The long standing efforts towards the power conversion efficiency (PCE) enhancement have witnessed the significance of effective defect passivation in the reduction of the charge recombination in polycrystalline perovskite thin film photovoltaics.^(6–11) The ionic nature of the perovskite lattice gives rise to unique passivation approaches such as molecular passivation through coordinate binding based on Lewis acid-base chemistry.^(12–15) A variety of organic molecules containing functional groups interacting with the defects have been reported to enhance the PCE and stability of perovskite solar cells *via* defect passivation.^(16–18) However, selection of the correct configuration within a tremendously large molecule pool and the lack of in-depth understanding of the corresponding passivation mechanism pose a significant challenge to perovskite research community: the dire need for molecular design rules for effective defect passivation.⁽¹⁹⁾ For instance, molecules containing the carbonyl group, well-known as a Lewis base, have been reported as effective passivation agents in perovskites.^(20, 21) However, while the rich chemistry in organic molecules enables the structural tunability, it also adds up to the complexity to finding the most effective passivating molecules.⁽²²⁾ A problem arises that there are a variety of molecules containing carbonyl groups, but what kind of molecular structure will show the most effectiveness is often difficult to judge. This brings out the significance of investigation on the chemical environment of the effective functional groups and its effect on defect passivation.

Herein, we demonstrate high efficiencies for $\text{FA}_x\text{MA}_{1-x}\text{PbI}_x\text{Br}_{3-x}$ perovskite photovoltaic devices *via* rational design and comprehensive investigation of the chemical environment around the active functional group for defect passivation. A set of small molecules sharing the identical functional groups but with strategically varying chemical structure were designed: namely theophylline, caffeine and theobromine, which are the commonly found components in tea, coffee and chocolate, respectively. These molecules are easily accessible and therefore it is another step towards perovskite commercialization. The chemical structures of the molecules are shown in **Fig. 5.1A**. In order to investigate the properties of defect passivation, defect identification is the prerequisite.(23) After intensive studies, the interior defects of perovskite have become negligible compared to the surface ones due to now available high-quality perovskite polycrystalline thin film fabrication of monolayered perovskite grains.(24-26) Utilizing the first-principles density-functional theory calculations, we first compared the formation energies of selected native defects that form on the perovskite surface. Pb and I involving point defects, Pb vacancy (V_{Pb}), I vacancy (V_{I}) and Pb-I antisite (Pb_{I} and I_{Pb} , corresponding to I site substitution by Pb, and Pb site substitution by I, respectively) were particularly taken into consideration because the band edges of perovskite were reported to be composed of Pb and I orbitals.(27, 28) As confirmed by X-ray photoelectron spectroscopy (XPS), the surface of the as-fabricated perovskite thin film using a two-step method was Pb-rich. (Fig. A5.1) Therefore, we focused on the (100) surface with PbI_2 termination in a Pb-rich condition. The types of surface defects studied, and their corresponding top layer view of atomic structures are shown in Fig. 5.1B. The formation energies of the defects were calculated using PDE-D3 method and are summarized in Table B5.1. The defect formation energies (DFE) of V_{Pb} , V_{I} , Pb_{I} , and I_{Pb} on the surface were calculated to be 3.20 eV, 0.51 eV, 0.57 eV and 3.15 eV, respectively. Compared to the values reported in bulk perovskite, V_{Pb} , V_{I} and I_{Pb} defects show

similar DFE,(29) while the Pb_I antisite defect exhibited particularly lower formation energy than that in the bulk. This indicated that Pb_I antisite defect is more easily formed and becomes more dominant when it is on the surface. V_I was not considered even though the DFE is as low as Pb_I , because the interaction of molecules with the V_I turned out to be not energy favorable. (Fig. B5.2) Based on that, we focused on the interaction between the surface Pb_I antisite defect and candidate molecules for defect passivation.

I incorporated theophylline onto the surface of perovskite thin film using a post-treatment method, and a PCE enhancement from 21.02% to 23.48% was observed in the photovoltaic devices with ITO/SnO₂/perovskite/Spiro-OMeTAD/Ag structure. The current density-voltage (J - V) curves of the photovoltaic devices with and without theophylline treatment are compared in Fig. 5.1C and Table B5.2, in which the control device showed an open circuit voltage (V_OC) of 1.164 V, a short circuit current (J_SC) of 24.78 mA cm⁻², a fill factor (FF) of 72.88%, while the target device showed a V_OC of 1.191 V, a J_SC of 25.24 mA cm⁻², a FF of 78.11%. The significant enhancement in the V_OC is attributed to the surface passivation by theophylline *via* the Lewis base-acid interaction between C=O group and the antisite Pb. As shown in the surface structure model of perovskite with theophylline (Fig 5.1B), the C=O group on theophylline showed a strong interaction with the antisite Pb. Noticeably, the neighboring N-H on the imidazole ring also interact with the I of PbI_6^{2-} octahedron through a hydrogen bond, which strengthened the absorption of theophylline onto the Pb_I defect, resulting in an interaction energy (defined as $E_\text{molecule-perovskite} - E_\text{perovskite} - E_\text{molecule}$) as strong as -1.7 eV. This observation suggested that the neighboring hydrogen bond between the xanthene molecule and the PbI_6^{2-} octahedron can contribute to the defect passivation. A methyl group was added to the N on the imidazole ring of theophylline (resulting in caffeine) to eliminate the effect

from hydrogen bond between the N-H and I. The interaction of caffeine with surface Pb_1 defect is shown in Fig 5.1B. While the C=O of caffeine still interacted with the Pb antisite, as in the case of theophylline, the missing hydrogen bond between N-H and PbI_6^{2-} octahedron resulted in a weakened interaction resulting in a less favorable interaction energy of -1.3 eV. This leads to a lesser PCE enhancement with caffeine-treated perovskite photovoltaic device compared to that of the theophylline (Fig 5.1C). A lower PCE of 22.32% along with a lower V_{OC} of 1.178 V, J_{SC} of 25.04 mA cm^{-2} , FF of 75.76% was observed due to less effective surface defect passivation. As comparison, when the N-H is located next to the C=O group on the same six-membered ring, producing a shorter distance between the C=O and the N-H (i.e. theobromine), the spatially effective interaction between the N-H and I was disabled as C=O is bound to antisite Pb, resulting in an even weaker interaction energy of -1.1 eV (Fig. 5.1B). Although both C=O and N-H are coexisting, the lack of appropriate coordination of I to the molecule leads to ‘spatially destructive’ molecular configuration. In this configuration, the theobromine-treated devices showed a decrease in PCE to 20.24% with a lower V_{OC} of 1.163 V, J_{SC} of 24.27 mA cm^{-2} and FF of 71.58% compared with the reference device. This emphasizes the significance of not only the co-existence of N-H with C=O, but also the constructive configuration of the relative position of them to enable the cooperative multi-site interaction and synergistic passivation effect.

The variation in the C=O and the PbI_2 -terminated perovskite surface interaction with different molecular configurations was further studied using Fourier Transform Infrared Spectroscopy (FTIR). As shown in **Fig. 5.2A**, the C=O in pure theophylline showed a typical stretching vibration mode at 1660 cm^{-1} , while it shifted to 1630 cm^{-1} upon binding to PbI_2 . The downwards shift of 30 cm^{-1} of the C=O stretching vibration frequency resulted from the electron delocalization in C=O

when a Lewis base-acid adduct was formed, demonstrating a strong interaction between PbI_2 and $\text{C}=\text{O}$ in theophylline. The atomic distance between the O in $\text{C}=\text{O}$ and the Pb in PbI_2 based on theoretical modeling was as low as 2.28 Å. When the H was replaced by a methyl group on the N of imidazole to eliminate the effect of a hydrogen bond, the vibration frequency of $\text{C}=\text{O}$ in caffeine showed a shift of only 10 cm^{-1} upon addition of PbI_2 , indicating a weakened interaction between the $\text{C}=\text{O}$ and PbI_2 (Fig. 5.2B). The atomic distance between the corresponding O and Pb also increased to 2.32 Å, further confirming the weakened interaction due to the missing assistance of hydrogen bonding. In the case of theobromine, when the N-H was in a closer position to $\text{C}=\text{O}$, the interaction between the molecule and PbI_2 became comparable to that in theophylline, as evidenced by the large shift of $\text{C}=\text{O}$ stretching vibration frequency from 1655^{-1} to 1620 cm^{-1} and the short distance between O and Pb (Fig. 5.2C). However, this strong interaction is enabled by the free rotation of PbI_2 , which results in a different configuration than that in theophylline and caffeine. Hence, when the configuration of PbI_2 is fixed and shows a 90° angle between Pb and I atom as that on perovskite surface, i.e. PbI_6^{2-} octahedron, the N-H in a ‘wrong’ position becomes unfavorable for the interaction with I. This would either cause weakened interaction between the molecule and the perovskite surface or distorted PbI_6^{2-} octahedron, resulting in the ineffectiveness of defect passivation and perhaps causing even more defects due to the lattice distortion (Fig. A5.3). The surface passivation effects of the three molecules with different configuration were further studied by photoluminescence (PL). As shown in Fig. 5.2D, the PL intensity increased noticeably with the treatment by theophylline, implying the suppressed non-radiative charge recombination sites from defects.(20) With the caffeine treatment, an enhancement of PL intensity was also observed, but not as strong as that with the theophylline, suggesting a less effective passivation effect when the hydrogen bond between N-H and PbI_6^{2-} octahedron is missing. In the case of theobromine, however,

a decrease in PL intensity was observed compared with the reference one, which can be attributed to the destructive molecular configuration of the passivation agents causing more charge recombination sites. The trap density of states (t DOS) of the as-fabricated devices were also deduced from the angular frequency dependent capacitance. As shown in Fig. 5.2E, the t DOS as a function of the defect energy demonstrated a reduction in trap states for theophylline- and caffeine-treated perovskite compared with the reference device. In contrast, theobromine treatment induced more trap states, which is consistent with the decrease in PCE. The change in t DOS with different surface treatments was also confirmed by theoretical modeling (Fig. A5.4). In addition, electrochemical impedance spectroscopy (EIS) characterization was performed to demonstrate the carrier transport processes under illumination at the interface. The middle frequency zone of EIS semicircle should be dominated by junction capacitance and recombination resistance related to the interfaces between transport materials and perovskite. According to Fig. 5.2F, the device with theophylline surface treatment has the smallest impedance, signifying a substantially suppressed charge recombination at the interface, which originated from the reduced surface defect states. A larger impedance was observed in caffeine-treated device and an even larger impedance was measured in theobromine-treated device demonstrated the significance of the co-existing N-H bond and its constructive configuration to enable effective defect passivation.

Further characterizations were performed to better understand the perovskite interface with theophylline and gain more insights on the device behavior. High-resolution XPS patterns of the Pb 4*f* of the reference and theophylline-treated films are shown in **Fig. 5.3A** for surface chemistry comparison. For the theophylline-treated film, two main peaks located at 138.48 and 143.38 eV were observed corresponding to the Pb 4*f* 7/2 and Pb 4*f* 5/2, respectively. The reference film, on the

other hand, showed two main peaks at 138.27 and 143.13 eV. The peaks from Pb 4*f* shifted to higher binding energies in the film with theophylline surface treatment, indicating the interaction between the theophylline and the Pb on perovskite surface. The Ultraviolet photoelectron spectroscopy (UPS) was employed to measure the surface band structure with and without the theophylline surface treatment. As shown in Fig. 5.3B, the work function was determined to be -4.77 eV and -4.96 eV with the valance band maximum (VBM) of -5.66 eV and -5.73 eV for reference and theophylline, respectively, indicating a less n-type surface after theophylline treatment, which might be beneficial for the hole extraction of the device. Atomic Force Microscopy combined with Kelvin Probe Force Microscopy (KPFM) was further applied to probe the effect of theophylline on the surface morphology and surface potential. As shown in Fig. 5.3C, the theophylline-treated surface exhibited a higher electronic chemical potential than that of reference film, while keeping the surface morphology unchanged. The transient photoluminescence (TRPL) of the perovskite films with hole transporting layer was compared in Fig. 5.3D to delineate the carrier dynamics of the devices. The perovskite film with theophylline treatment showed a slightly longer carrier lifetime than the reference film, while a faster decay profile was observed when adding the hole transporting layer on top of the perovskite film. This demonstrated a better hole extraction with theophylline treatment,⁽²⁵⁾ most likely arising from lesser recombination sites at the interface and the slightly shallower work function of the perovskite film with theophylline. The improved carrier dynamics originating from the effective surface passivation by theophylline was further characterized by cross-sectional electron-beam-induced current (EBIC) measurement. In EBIC measurement, the e-beam excited carriers were collected based on the collection probability $CP(x, L_d)$, where x is the distance between junction and incident beam position, and L_d is the diffusion length of the carriers (Fig. A5.5). As shown in Fig. 5.3E, the device with

theophylline treatment exhibits higher EBIC current as compared to the reference device. The average intensity extracted from these EBIC maps demonstrates a general increase in the EBIC signal after treated with theophylline (Fig. A5.6), indicating an enhanced carrier collection efficiency.⁽³⁰⁾ Specifically in Fig. 5.3E, a representative EBIC line profile of the reference device shows a current decay from the HTL/perovskite to the SnO₂/perovskite interface. The decay indicates that carrier collection is limited by the hole diffusion length as the beam position moves away from the HTL/perovskite interface. In contrast, the device with theophylline treatment displays minimal decay within the perovskite layer in the EBIC line profile. This suggests that a longer diffusion length of holes is present in theophylline-treated sample and balanced electron and hole charge transport and collection is achieved, which is likely due to the reduced recombination sites at the surface of perovskite (Fig. 5.3E).

Further assessment of the performance of the photovoltaic devices based on the theophylline surface passivation was performed. As shown in **Fig. 5.4A**, the devices showed a negligible hysteresis (4.1%) due to the balanced charge collection originated from the effective surface passivation via rational molecule design, while the reference device showed a large hysteresis up to 7.6% (Table B5.3). External quantum efficiency (EQE) spectra of the devices were compared in Fig. 5.4B. An integrated J_{SC} of 24.42 mA cm⁻² from the target device matched well with the value measured from the J - V scan (<5% discrepancy), while control device showed an integrated J_{SC} of 23.56 mA cm⁻². A stabilized PCE of 22.64% was achieved with the target device when biased at 1.00 V while that of control device was 20.36% when biased at 0.98 V (Fig. 5.4C). The histogram of solar cell efficiencies for 40 devices is shown in Fig. 5.4D, which confirms good reproducibility of the performance improvement with theophylline (11.1% improvement in an average PCE from

20.36±0.53% to 22.61±0.58% with the incorporation of the theophylline). In Fig. 5.4E, the changes in PCE of the encapsulated devices at a relative humidity of 30-40% and temperature of 40 °C were tracked over time to test the long-term operational stability. While the reference device degraded by more than 80% in 500 h, the target device maintained over 90% of its initial efficiency during this time. Also, as shown in Fig. A5.7, the shelf stability of the device based on theophylline treatment was noticeably enhanced, maintaining over 95% of its original PCE when stored under ambient conditions with 20-30% humidity at 25 °C for 60 days. In contrast, the reference device lost over 35% of its initial efficiency. The improvement in the operational stability could be attributed to the strong interaction between the theophylline and the surface defects. This stabilized the perovskite surface and suppressed the ion migration, which usually emanates from the defect sites.^(31–33)

In conclusion, we demonstrated the so far largely ignored chemical environment around the effective functional group for defect passivation in perovskite surfaces. The hydrogen bond formation between N-H and I was investigated to be secondary assistance with the primary C=O binding with Pb to maximize the surface defect passivation in perovskite. This synergistic effect can be enabled only when the N-H and C=O are in a constructive configuration in the molecular structure: the sole influence of C=O is insufficient, a neighboring N-H is needed; the co-existence of C=O and N-H is insufficient, a constructive structural configuration is needed. This provides new insights on the molecular design of effective defect passivation strategy for achieving highly efficient and stable perovskite optoelectronics.

References

1. H. S. Kim, C. R. Lee, J. H. Im, K. B. Lee, T. Moehl, A. Marchioro, S. J. Moon, R. Humphry-Baker, J. H. Yum, J. E. Moser, M. Grätzel, N. G. Park, Lead iodide perovskite sensitized all-solid-state submicron thin film mesoscopic solar cell with efficiency exceeding 9%. *Sci. Rep.* **2**, 591 (2012).
2. S. D. Stranks, H. J. Snaith, Metal-halide perovskites for photovoltaic and light-emitting devices. *Nat. Nanotechnol.* **10**, 391–402 (2015).
3. H. Zhu, K. Miyata, Y. Fu, J. Wang, P. P. Joshi, D. Niesner, K. W. Williams, S. Jin, X. Y. Zhu, Screening in crystalline liquids protects energetic carriers in hybrid perovskites. *Science.* **353**, 1409–1413 (2016).
4. M. Xiao, F. Huang, W. Huang, Y. Dkhissi, Y. Zhu, J. Etheridge, A. Gray-Weale, U. Bach, Y. B. Cheng, L. Spiccia, A fast deposition-crystallization procedure for highly efficient lead iodide perovskite thin-film solar cells. *Angew. Chemie - Int. Ed.* **53**, 9898–9903 (2014).
5. W. Nie, H. Tsai, R. Asadpour, J. C. Blancon, A. J. Neukirch, G. Gupta, J. J. Crochet, M. Chhowalla, S. Tretiak, M. A. Alam, H. L. Wang, A. D. Mohite, High-efficiency solution-processed perovskite solar cells with millimeter-scale grains. *Science.* **347**, 522–525 (2015).
6. J. Tong, Z. Song, D. H. Kim, X. Chen, C. Chen, A. F. Palmstrom, P. F. Ndione, M. O. Reese, S. P. Dunfield, O. G. Reid, J. Liu, F. Zhang, S. P. Harvey, Z. Li, S. T. Christensen, G. Teeter, D. Zhao, M. M. Al-Jassim, M. F. A. M. Van Hest, M. C. Beard, S. E. Shaheen, J. J. Berry, Y. Yan, K. Zhu, Carrier lifetimes of $>1 \mu\text{s}$ in Sn-Pb perovskites enable efficient all-perovskite tandem solar cells. *Science.* **364**, 475–479 (2019).
7. H. Tan, A. Jain, O. Voznyy, X. Lan, F. P. G. De Arquer, J. Z. Fan, R. Quintero-Bermudez,

- M. Yuan, B. Zhang, Y. Zhao, F. Fan, P. Li, L. N. Quan, Y. Zhao, Z. H. Lu, Z. Yang, S. Hoogland, E. H. Sargent, Efficient and stable solution-processed planar perovskite solar cells via contact passivation. *Science*. **355**, 722–726 (2017).
8. X. Zheng, B. Chen, J. Dai, Y. Fang, Y. Bai, Y. Lin, H. Wei, X. C. Zeng, J. Huang, Defect passivation in hybrid perovskite solar cells using quaternary ammonium halide anions and cations. *Nat. Energy*. **2**, 17102 (2017).
 9. J. J. Yoo, S. Wieghold, M. Sponseller, M. Chua, S. N. Bertram, N. T. P. Hartono, J. Tresback, E. Hansen, J.-P. Correa-Baena, V. Bulovic, T. Buonassisi, S. S. Shin, M. G. Bawendi, An Interface Stabilized Perovskite Solar Cell with High Stabilized Efficiency and Low Voltage Loss. *Energy Environ. Sci.* **12**, 2192–2199 (2019).
 10. Q. Jiang, Y. Zhao, X. Zhang, X. Yang, Y. Chen, Z. Chu, Q. Ye, X. Li, Z. Yin, J. You, Surface passivation of perovskite film for efficient solar cells. *Nat. Photonics*. **13**, 460–466 (2019).
 11. N. Li, S. Tao, Y. Chen, X. Niu, C. K. Onwudinanti, C. Hu, Z. Qiu, Z. Xu, G. Zheng, L. Wang, Y. Zhang, L. Li, H. Liu, Y. Lun, J. Hong, X. Wang, Y. Liu, H. Xie, Y. Gao, Y. Bai, S. Yang, G. Brocks, Q. Chen, H. Zhou, Cation and anion immobilization through chemical bonding enhancement with fluorides for stable halide perovskite solar cells. *Nat. Energy*. **4**, 408–415 (2019).
 12. J. S. Manser, J. A. Christians, P. V Kamat, Intriguing Optoelectronic Properties of Metal Halide Perovskites. *Chem. Rev.* **116**, 12956–13008 (2016).
 13. H. Zhang, H. Chen, C. C. Stoumpos, J. Ren, Q. Hou, X. Li, J. Li, H. He, H. Lin, J. Wang, F. Hao, M. G. Kanatzidis, Thiazole-Induced Surface Passivation and Recrystallization of

- CH₃NH₃PbI₃ Films for Perovskite Solar Cells with Ultrahigh Fill Factors. *ACS Appl. Mater. Interfaces*. **10**, 42436–42443 (2018).
14. J. W. Lee, H. S. Kim, N. G. Park, Lewis Acid-Base Adduct Approach for High Efficiency Perovskite Solar Cells. *Acc. Chem. Res.* **49**, 311–319 (2016).
 15. Y. Zong, Y. Zhou, Y. Zhang, Z. Li, L. Zhang, M. G. Ju, M. Chen, S. Pang, X. C. Zeng, N. P. Padture, Continuous Grain-Boundary Functionalization for High-Efficiency Perovskite Solar Cells with Exceptional Stability. *Chem.* **4**, 1404–1415 (2018).
 16. D. Bi, C. Yi, J. Luo, J. D. Décoppet, F. Zhang, S. M. Zakeeruddin, X. Li, A. Hagfeldt, M. Grätzel, Polymer-templated nucleation and crystal growth of perovskite films for solar cells with efficiency greater than 21%. *Nat. Energy*. **1**, 16142 (2016).
 17. B. Chen, P. N. Rudd, S. Yang, Y. Yuan, J. Huang, Imperfections and their passivation in halide perovskite solar cells. *Chem. Soc. Rev.* **48**, 3842–3867 (2019).
 18. T. Wu, Y. Wang, X. Li, Y. Wu, X. Meng, D. Cui, X. Yang, L. Han, Efficient Defect Passivation for Perovskite Solar Cells by Controlling the Electron Density Distribution of Donor- π -Acceptor Molecules. *Adv. Energy Mater.* **9**, 1803766 (2019).
 19. W. Xu, Q. Hu, S. Bai, C. Bao, Y. Miao, Z. Yuan, T. Borzda, A. J. Barker, E. Tyukalova, Z. Hu, M. Kawecki, H. Wang, Z. Yan, X. Liu, X. Shi, K. Uvdal, M. Fahlman, W. Zhang, M. Duchamp, J. M. Liu, A. Petrozza, J. Wang, L. M. Liu, W. Huang, F. Gao, Rational molecular passivation for high-performance perovskite light-emitting diodes. *Nat. Photonics*. **13**, 418–424 (2019).
 20. R. Wang, J. Xue, L. Meng, J. W. Lee, Z. Zhao, P. Sun, L. Cai, T. Huang, Z. Wang, Z. K. Wang, Y. Duan, J. L. Yang, S. Tan, Y. Yuan, Y. Huang, Y. Yang, Caffeine Improves the

- Performance and Thermal Stability of Perovskite Solar Cells. *Joule*. **3**, 1464–1477 (2019).
21. T. Niu, J. Lu, R. Munir, J. Li, D. Barrit, X. Zhang, H. Hu, Z. Yang, A. Amassian, K. Zhao, S. F. Liu, Stable High-Performance Perovskite Solar Cells via Grain Boundary Passivation. *Adv. Mater.* **30**, 1706576 (2018).
 22. H. Zhang, M. K. Nazeeruddin, W. C. H. Choy, Perovskite Photovoltaics: The Significant Role of Ligands in Film Formation, Passivation, and Stability. *Adv. Mater.* **31**, 1805702 (2019).
 23. W. J. Yin, T. Shi, Y. Yan, Unusual defect physics in $\text{CH}_3\text{NH}_3\text{PbI}_3$ perovskite solar cell absorber. *Appl. Phys. Lett.* **104**, 063903 (2014).
 24. W. S. Yang, B. W. Park, E. H. Jung, N. J. Jeon, Y. C. Kim, D. U. Lee, S. S. Shin, J. Seo, E. K. Kim, J. H. Noh, S. Il Seok, Iodide management in formamidinium-lead-halide-based perovskite layers for efficient solar cells. *Science*. **356**, 1376–1379 (2017).
 25. N. J. Jeon, H. Na, E. H. Jung, T. Y. Yang, Y. G. Lee, G. Kim, H. W. Shin, S. Il Seok, J. Lee, J. Seo, A fluorene-terminated hole-transporting material for highly efficient and stable perovskite solar cells. *Nat. Energy*. **3**, 682–689 (2018).
 26. E. H. Jung, N. J. Jeon, E. Y. Park, C. S. Moon, T. J. Shin, T. Y. Yang, J. H. Noh, J. Seo, Efficient, stable and scalable perovskite solar cells using poly(3-hexylthiophene). *Nature*. **567**, 511–515 (2019).
 27. M. A. Green, A. Ho-Baillie, H. J. Snaith, The emergence of perovskite solar cells. *Nat. Photonics*. **8**, 506–514 (2014).
 28. Z. Xiao, Z. Song, Y. Yan, From Lead Halide Perovskites to Lead-Free Metal Halide

Perovskites and Perovskite Derivatives. *Adv. Mater.*, 1803792 (2019).

29. N. Liu, C. Y. Yam, First-principles study of intrinsic defects in formamidinium lead triiodide perovskite solar cell absorbers. *Phys. Chem. Chem. Phys.* **20**, 6800–6804 (2018).
30. E. Edri, S. Kirmayer, S. Mukhopadhyay, K. Gartsman, G. Hodes, D. Cahen, Elucidating the charge carrier separation and working mechanism of $\text{CH}_3\text{NH}_3\text{PbI}_{3-x}\text{Cl}_x$ perovskite solar cells. *Nat. Commun.* **5**, 3461 (2014).
31. R. Wang, M. Mujahid, Y. Duan, Z. K. Wang, J. Xue, Y. Yang, A Review of Perovskites Solar Cell Stability. *Adv. Funct. Mater.*, 1808843 (2019).
32. J. A. Christians, P. Schulz, J. S. Tinkham, T. H. Schloemer, S. P. Harvey, B. J. Tremolet De Villers, A. Sellinger, J. J. Berry, J. M. Luther, Tailored interfaces of unencapsulated perovskite solar cells for >1,000 hour operational stability. *Nat. Energy.* **3**, 68–74 (2018).
33. Y. Hou, X. Du, S. Scheiner, D. P. McMeekin, Z. Wang, N. Li, M. S. Killian, H. Chen, M. Richter, I. Levchuk, N. Schrenker, E. Spiecker, T. Stubhan, N. A. Luechinger, A. Hirsch, P. Schmuki, H. P. Steinrück, R. H. Fink, M. Halik, H. J. Snaith, C. J. Brabec, A generic interface to reduce the efficiency-stability-cost gap of perovskite solar cells. *Science.* **358**, 1192–1197 (2017).

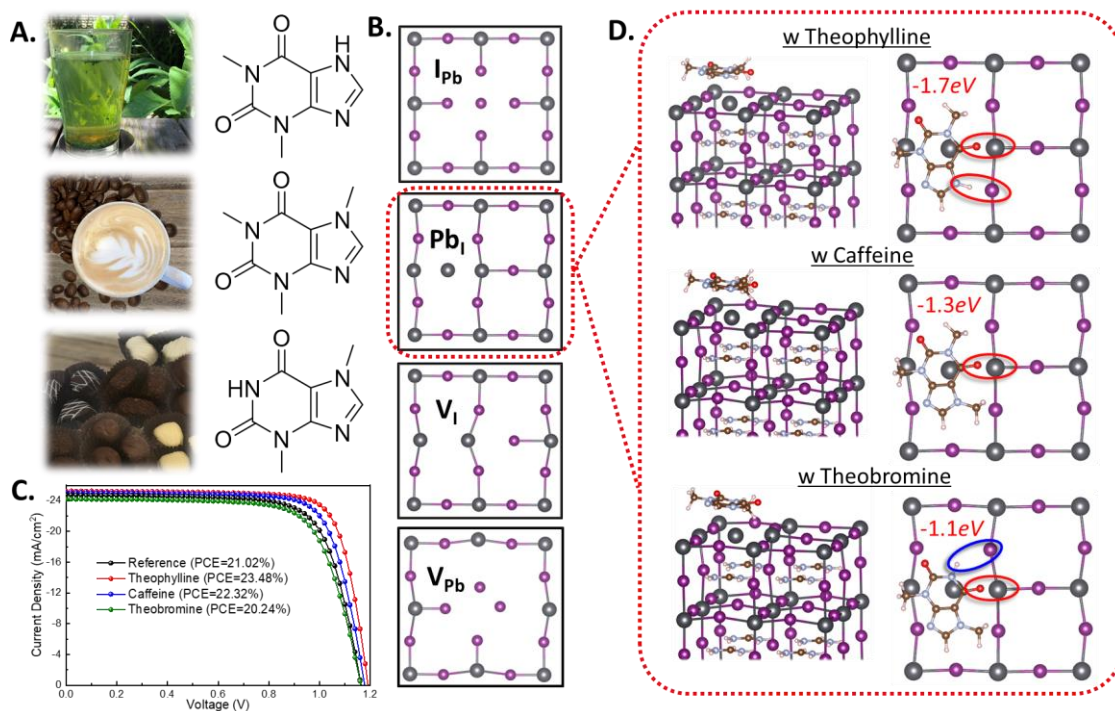


Fig. 5.1 Surface defect identification and constructive configuration of the C=O group in three different chemical environments.

(A) Chemical structures of three different passivation molecules. (top to bottom: Theophylline, Caffeine and Theobromine) (B) Top view of the various types of surface defects. (C) *J-V* curves of perovskite solar cells with or without small molecules treatment under reverse scan direction. (D) Theoretical models of perovskite with molecular surface passivation of Pb_I antisite.

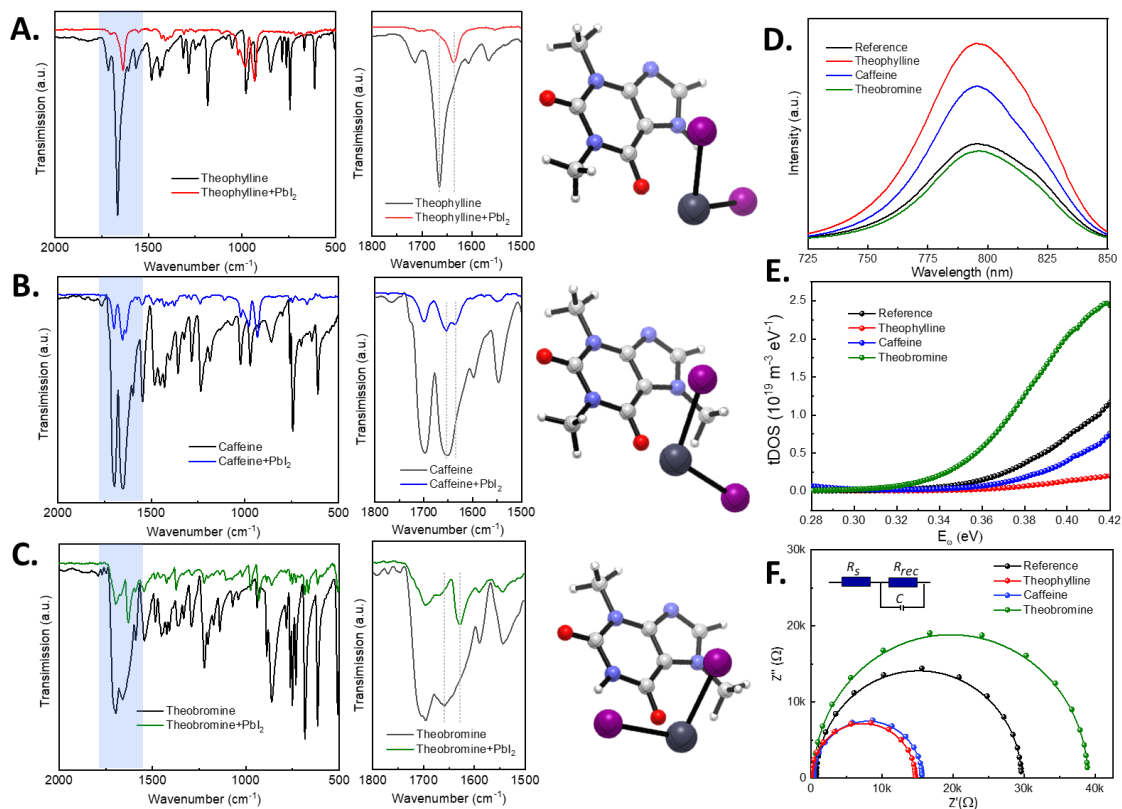


Fig. 5.2 Investigation of the interactions between surface defects and the small molecules.

FTIR spectra of (A) pure theophylline and theophylline-PbI₂ films; (B) pure caffeine and caffeine-PbI₂ films; (C) pure theobromine and theobromine-PbI₂ films. (D) PL spectra of perovskite films without and with small molecules treatment. (E) Trap density of states (*t*DOS) in perovskite solar cells with or without small molecules treatment. (F) Nyquist plots of perovskite solar cells with or without small molecules treatment measured in the dark and at corresponding open-circuit voltages.

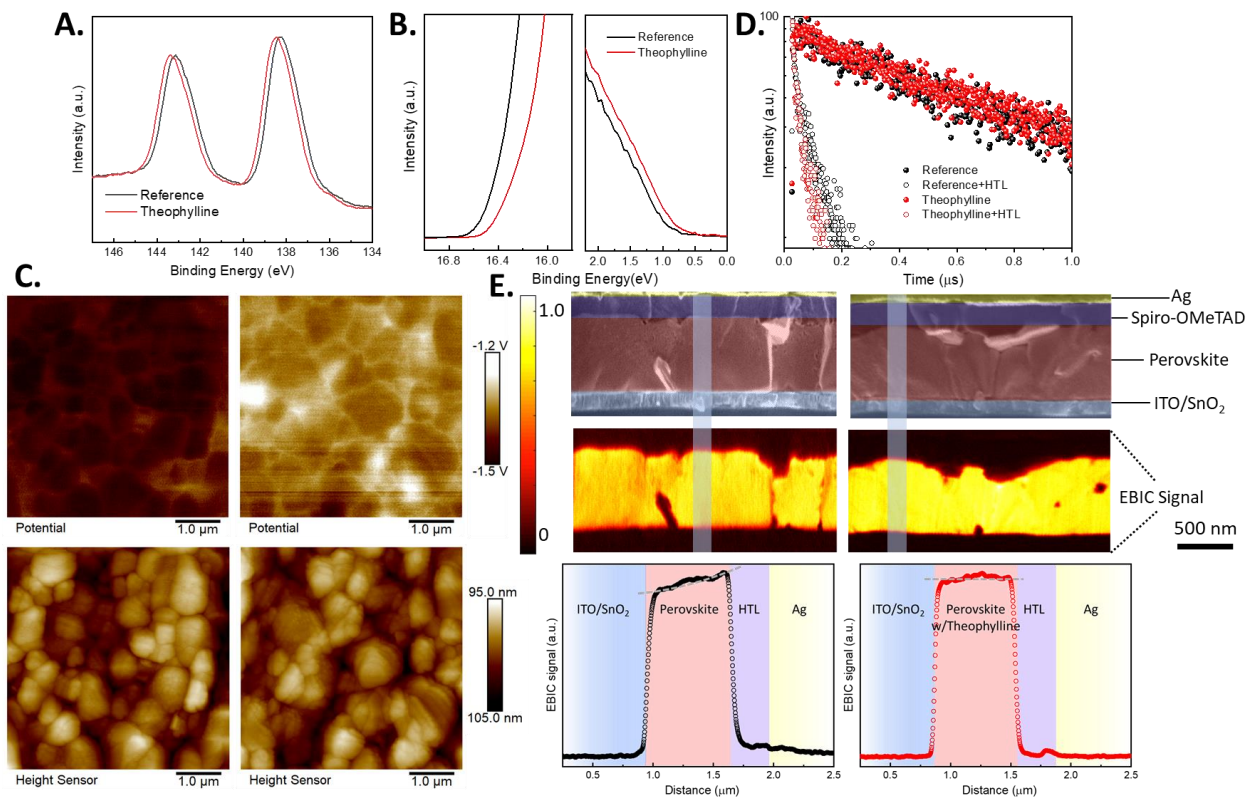


Fig. 5.3 Characterization of perovskite films and interfaces with theophylline treatment.

(A) XPS data for Pb 4f 7/2 and Pb 4f 5/2 core level spectra in perovskite films with or without theophylline treatment. (B) UPS spectra of perovskite films with or without theophylline treatment. (C) AFM and KPFM images of perovskite films with (right) or without (left) theophylline treatment. (D) Time-resolved PL spectra of perovskite films before and after depositing Spiro-OMeTAD without and with theophylline treatment. (E) Cross-section SEM images and the corresponding EBIC images and line profile of the perovskite solar cells with (right) or without (left) theophylline treatment.

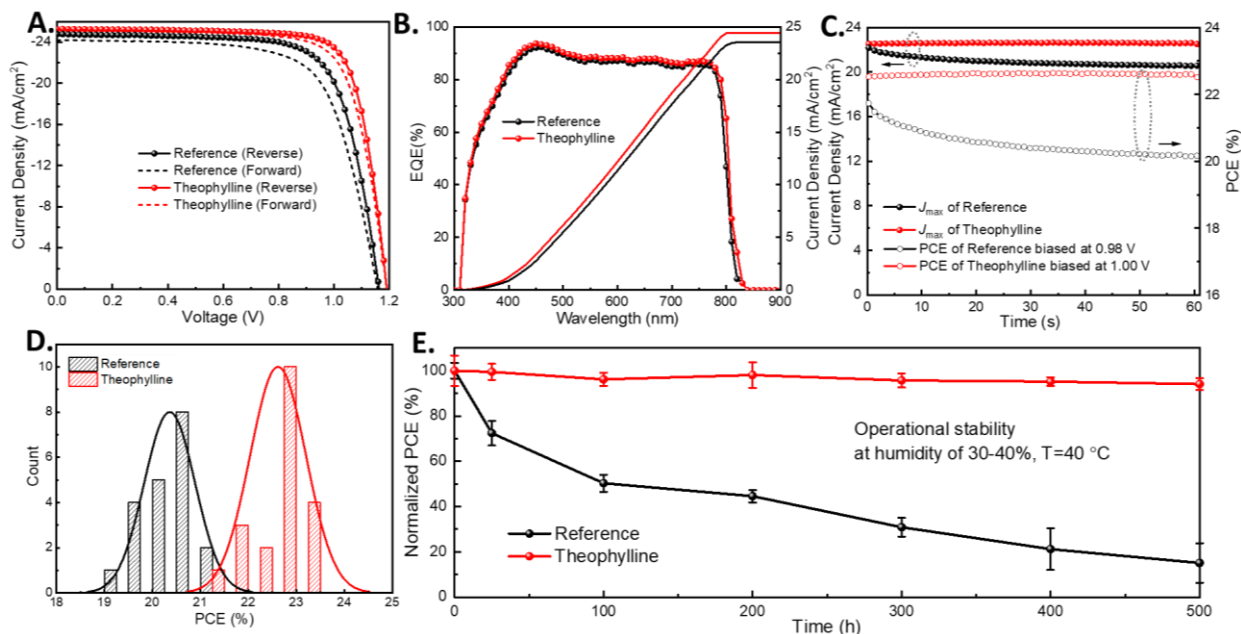


Fig. 5.4 Enhanced photovoltaic performance and long-term stability of perovskite solar cells with theophylline treatment.

(A) Current density–voltage (J – V) curves of perovskite solar cells with or without theophylline treatment. (B) EQE curves of perovskite solar cells with or without theophylline treatment. (C) Stabilized maximum power output and the photocurrent density at maximum power point as a function of time for the best performing perovskite solar cells with or without theophylline treatment, as shown in Fig. 4A, recorded under simulated one-sun AM1.5G illumination. (D) PCE distribution of perovskite solar cells with or without theophylline treatment. (E) Evolution of the PCEs measured from the encapsulated perovskite solar cells with or without theophylline treatment exposed to continuous light ($90 \pm 10 \text{ mW cm}^{-2}$) under open-circuit condition.

Appendix A

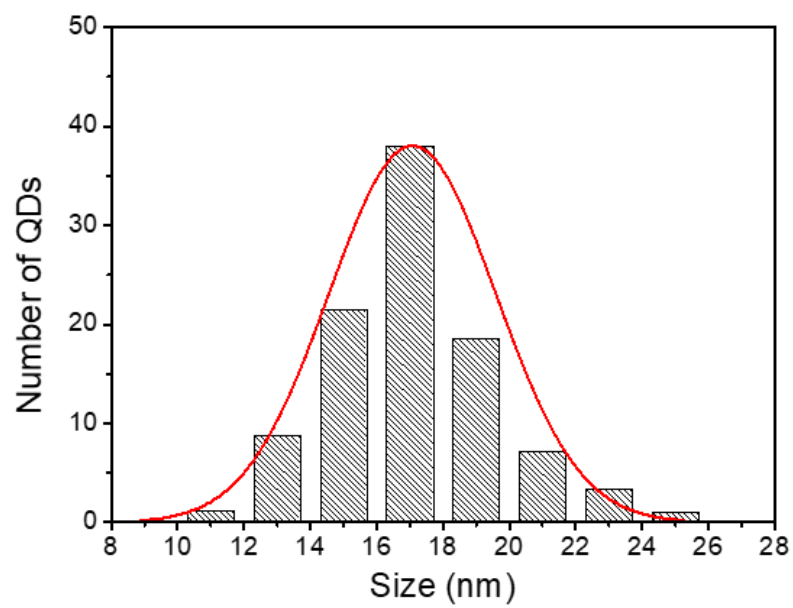


Figure A2.1 Size distribution of FAPbI₃ CQDs measured from Figure 2.1 A.

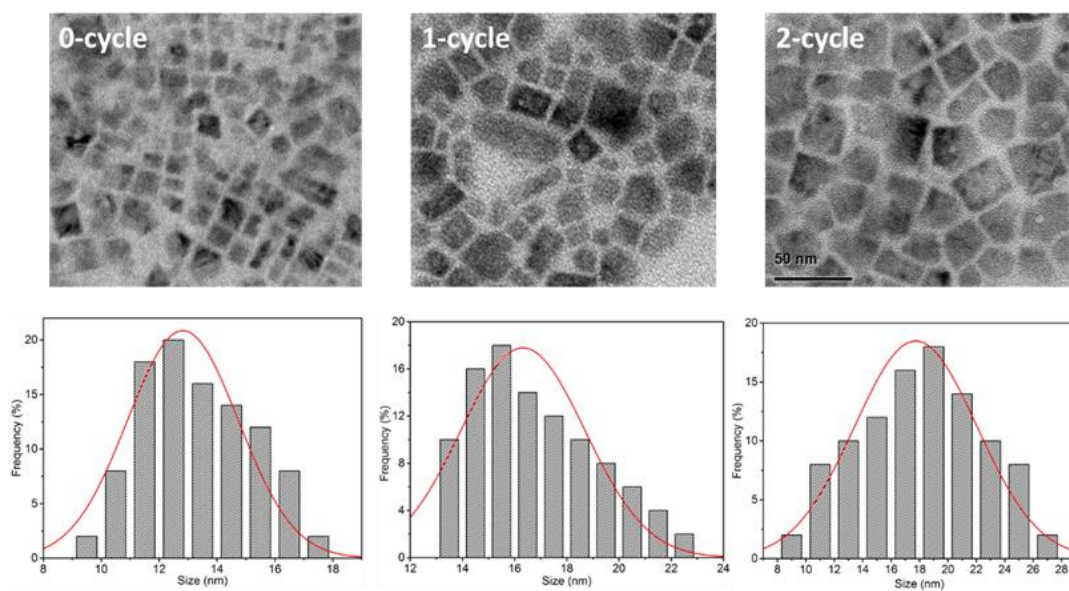


Figure A2.2. Transmission electron microscopy (TEM) images of FAPbI₃ CQDs with different cycles of ligand treatment and corresponding size distributions.

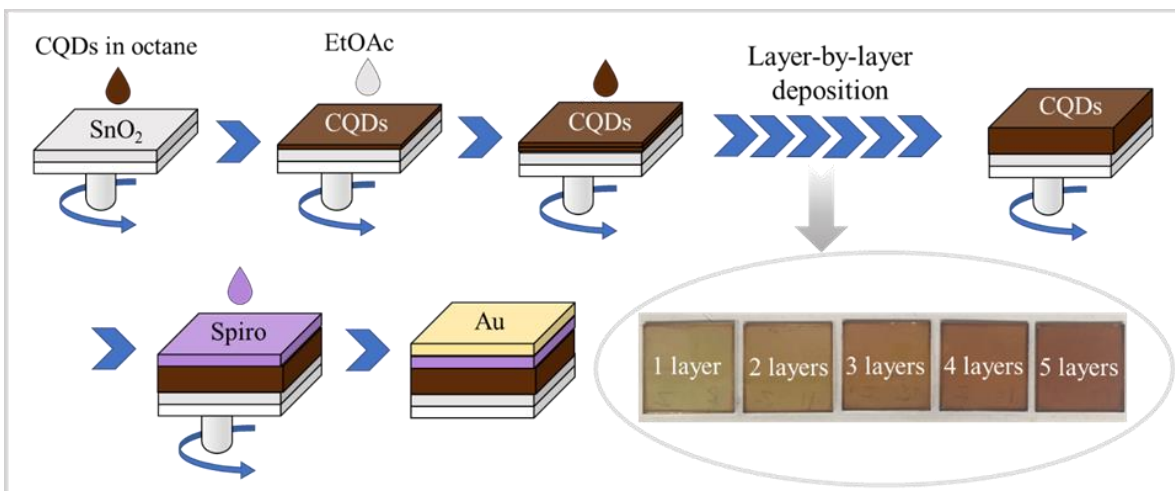


Figure A2.3 Schematic representation of device fabrication process (inset: photographs of CQDs film with the increasing number of layers).

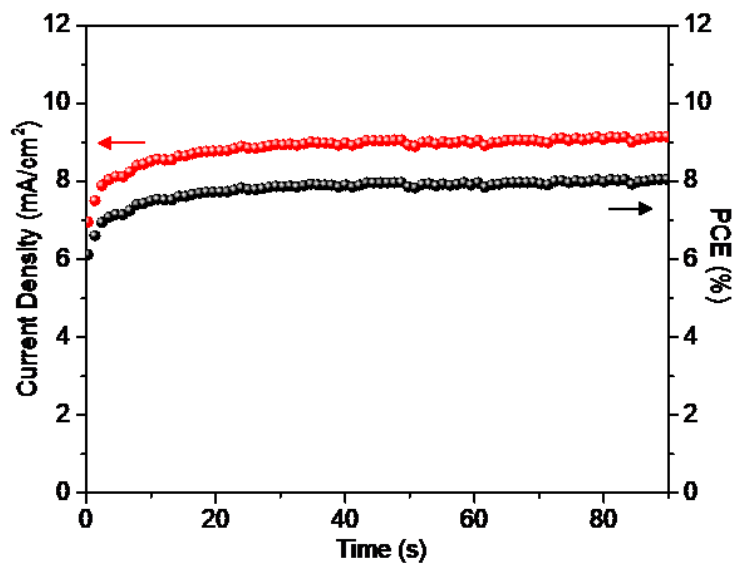


Figure A2.4 Stabilized power output (SPO) of the device obtained by measuring the current density while the device is biased at 0.88 V.

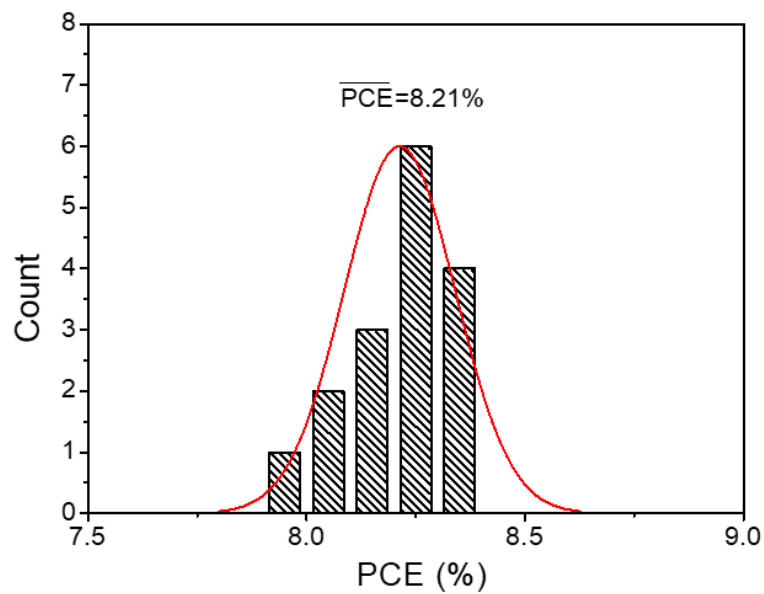


Figure A2.5 Distribution of power conversion efficiency (PCE) measured from 16 FAPbI₃ CQD solar cell devices.

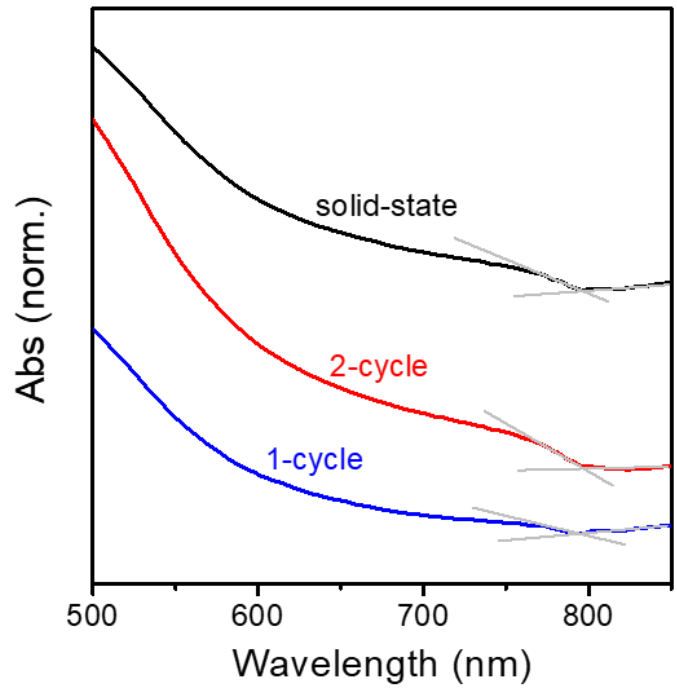


Figure A2.6 UV-vis spectra of FAPbI₃ CQD films with different cycles of surface treatment.

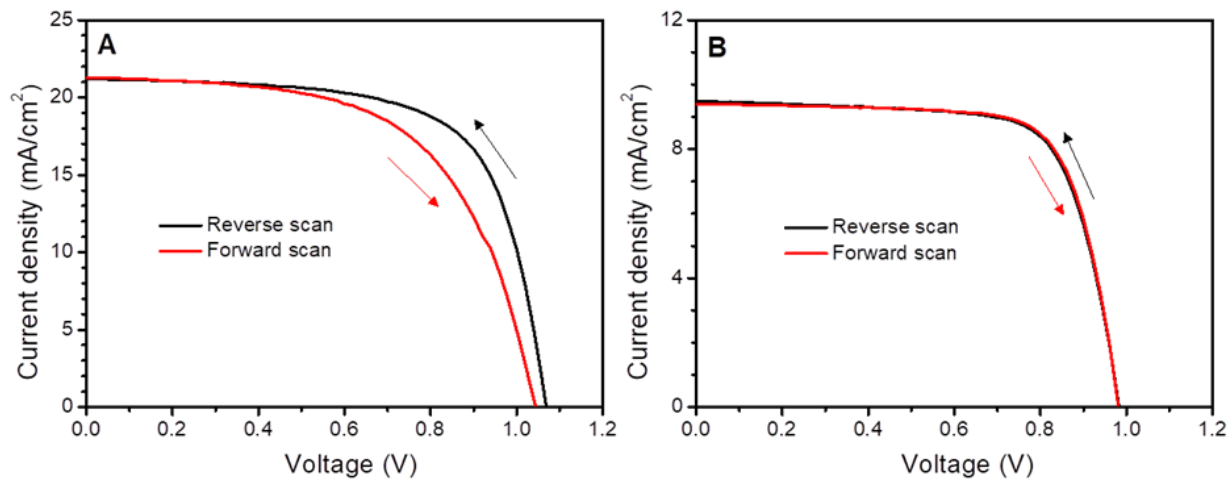


Figure A2.7 Current density-voltage (J-V) curves of FAPbI₃ perovskite solar cells based on (A) bulk and (B) CQD thin films.

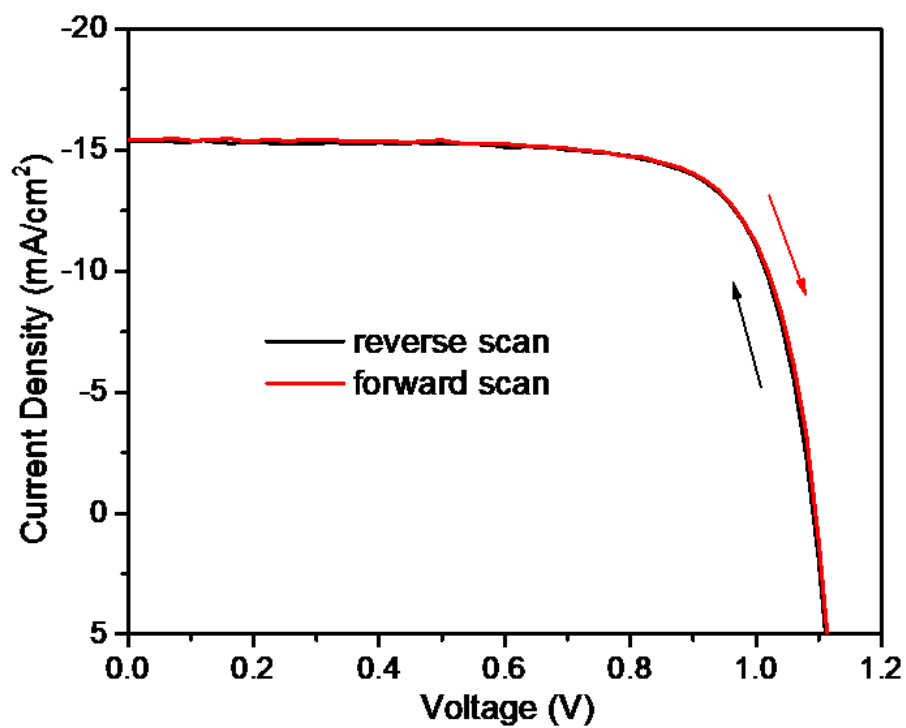


Figure A3.1 Current density-voltage ($J-V$) curves of FAPbI₃ CQDs/ITIC based solar cells with forward and reverse scan.

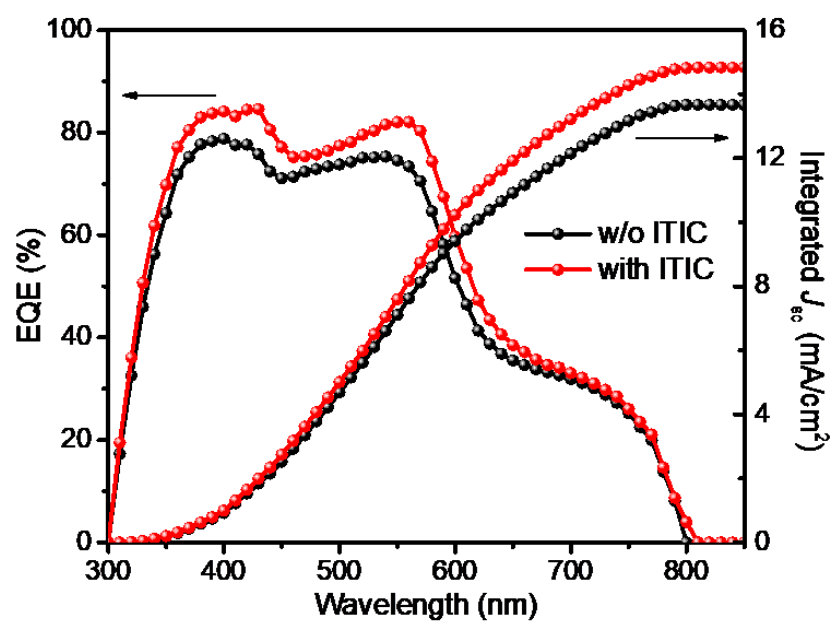


Figure A3.2. EQE spectra together with EQE data-based integrated J_{sc} of the devices based on FAPbI₃ CQDs with and without ITIC.

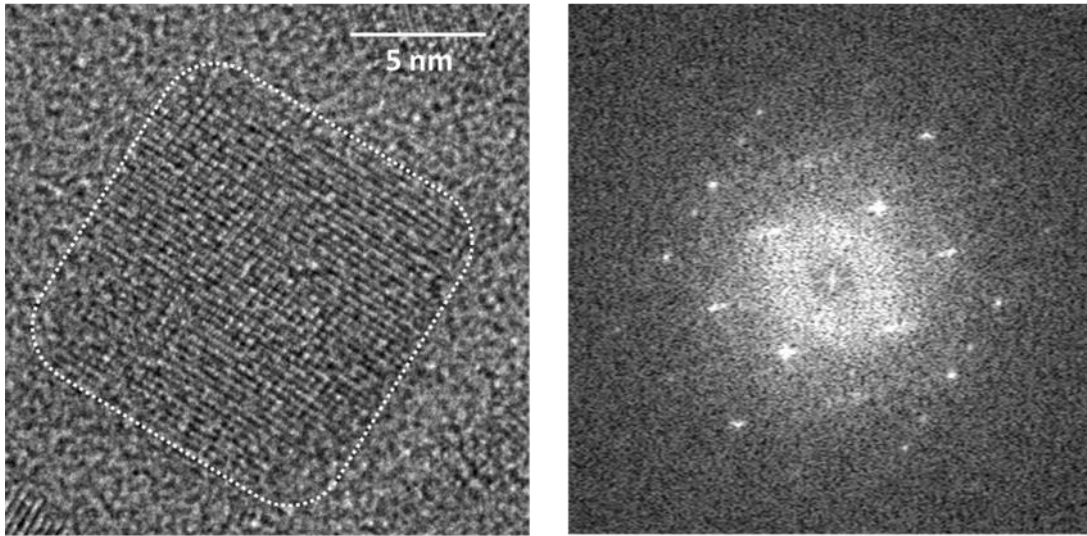


Figure A3.3. HRTEM image (left) and the fast Fourier transform (FFT) image (right).

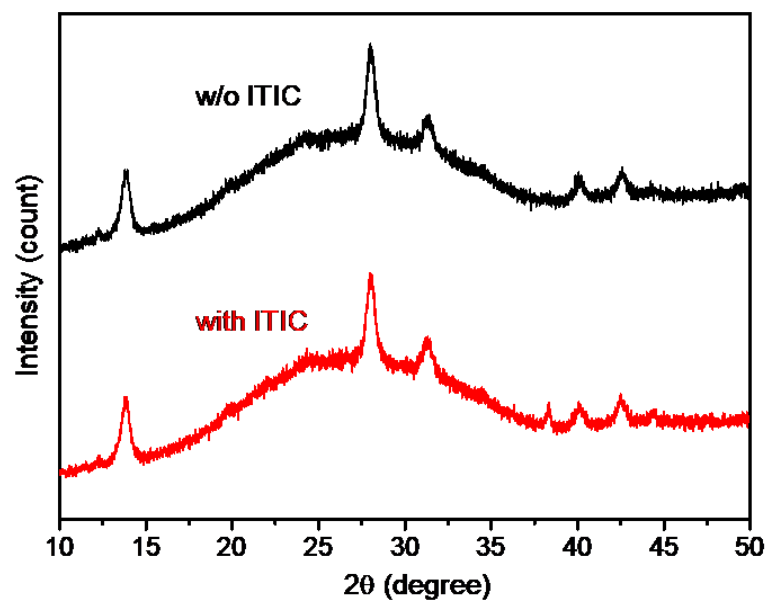


Figure A3.4. X-ray diffraction (XRD) patterns of FAPbI₃ CQDs films with and without ITIC.

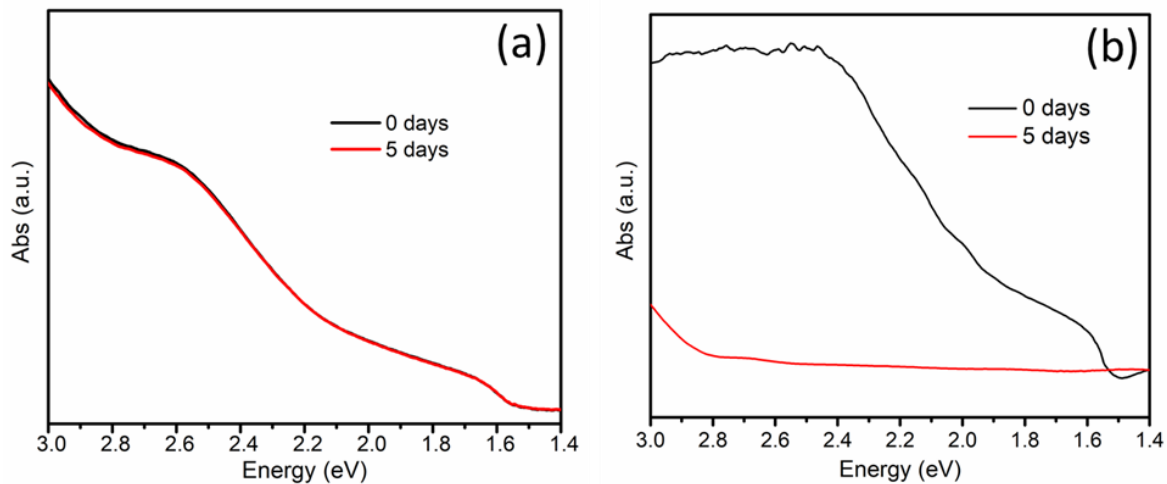


Figure A3.5. UV-vis absorption spectra of a) perovskite QDs thin film and b) perovskite bulk film stored under ambient condition.

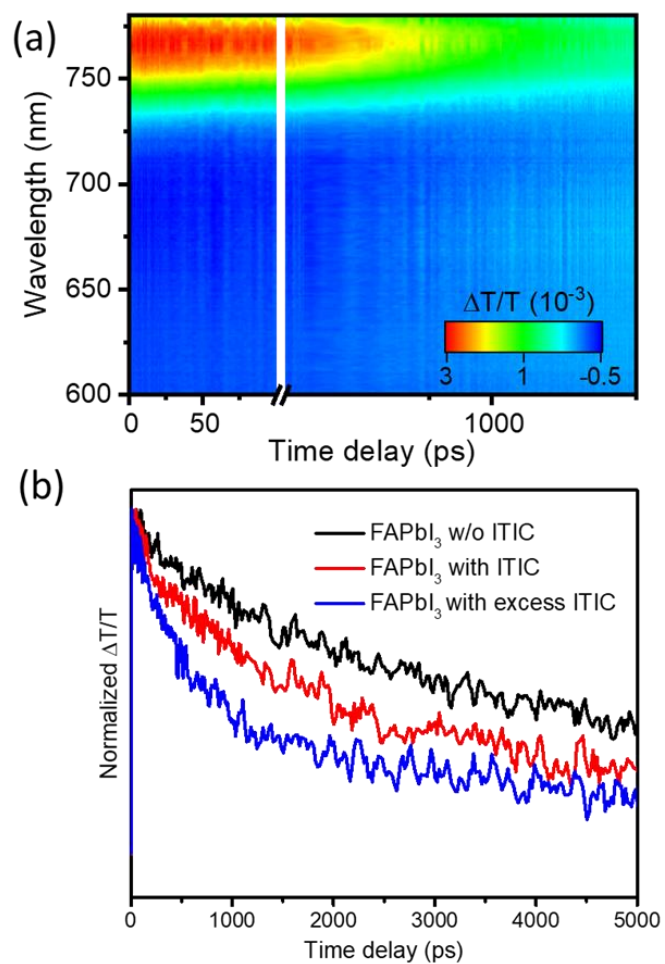


Figure A3.6. a) TA spectra of FAPbI₃ CQD film with excess amount of ITIC. b) The dynamic of bleaching peak probed at ~770 nm of FAPbI₃ CQDs film with different amounts of ITIC.

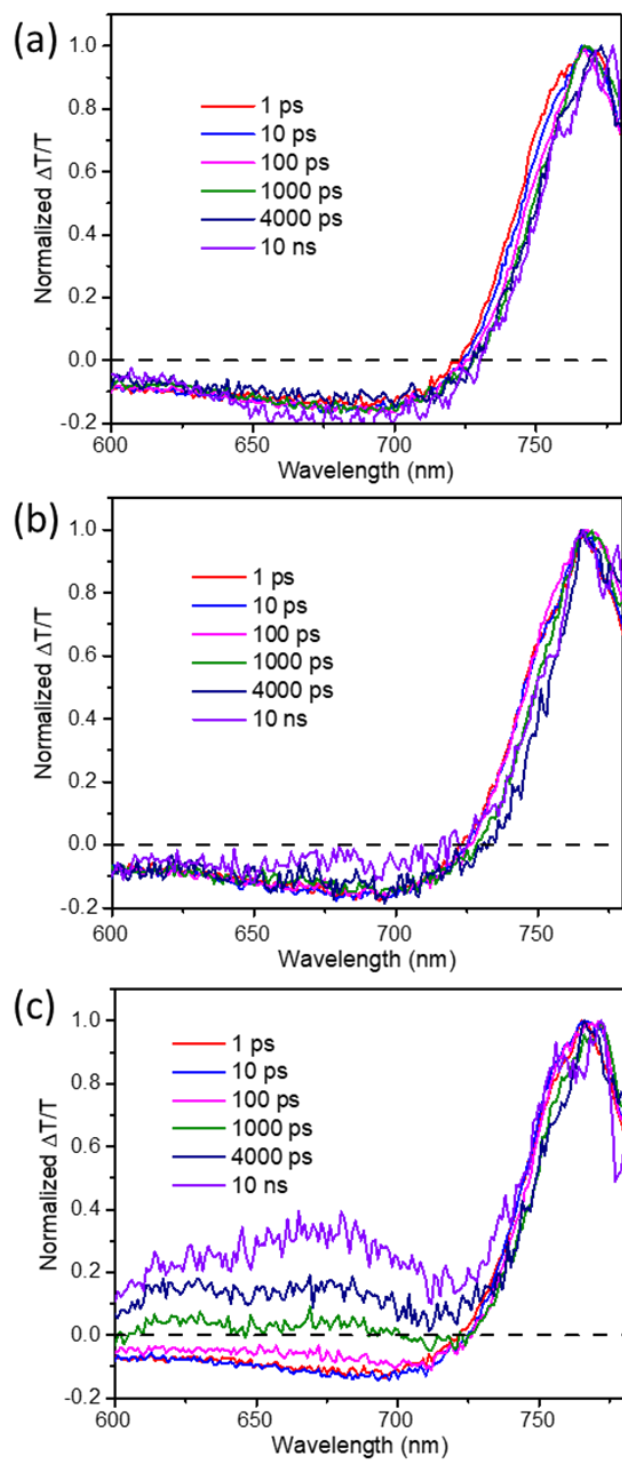


Figure A3.7. The differential transmission spectra ($\Delta T/T$) of a) pure FAPbI₃ CQDs, b) FAPbI₃ CQDs with ITIC, and c) FAPbI₃ CQDs with excess amount of ITIC.

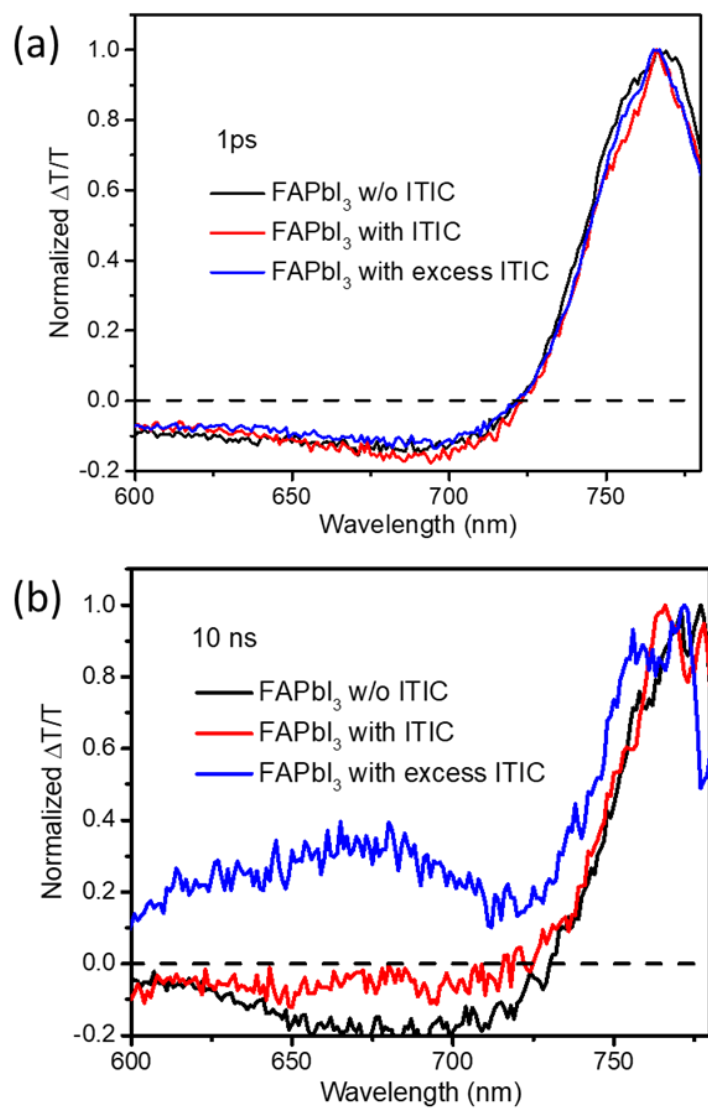


Figure A3.8 The comparison of $\Delta T/T$ spectra of FAPbI₃ CQDs with different amount of ITIC at a) 1 ps and b) 10 ns.

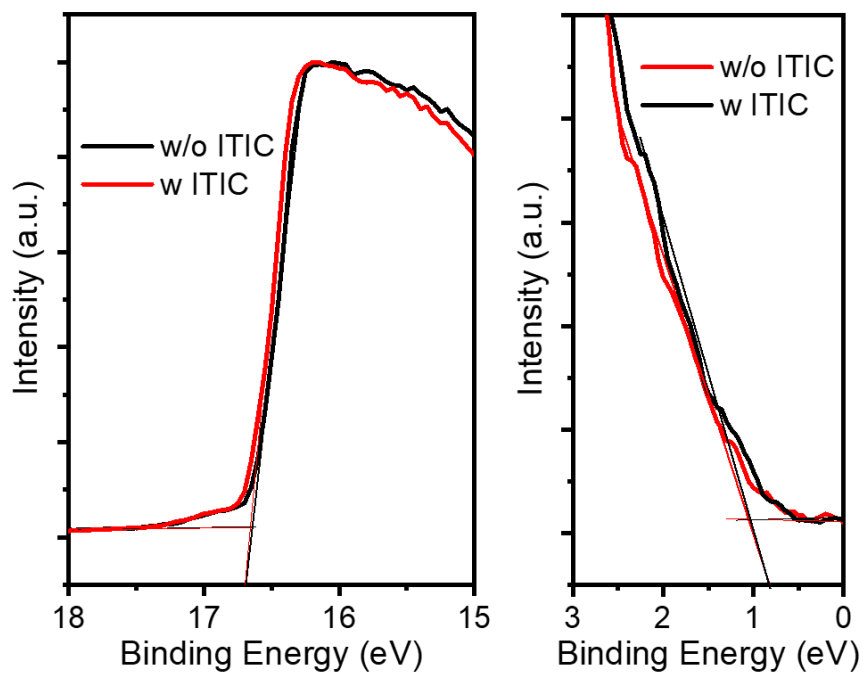


Figure A3.9. Ultraviolet photoelectron spectroscopy (UPS) determination of energy levels of fermi level and valence band maximum of FAPbI₃ CQDs.

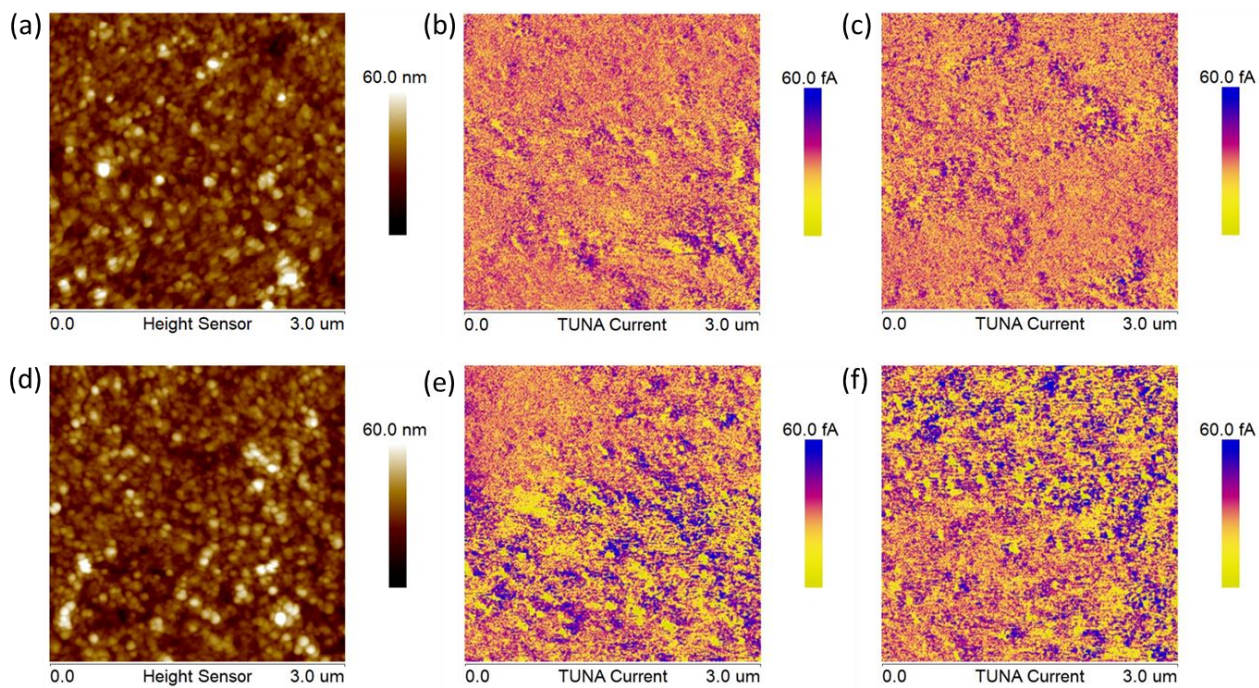


Figure A3.10 a, d) AFM and b, c, e, f) corresponding conductive AFM images under b, e) room light and c, f) low intensity light illumination provided by the AFM setup of a-c) pure FAPbI₃ CQDs film and d-f) FAPbI₃ CQDs film with ITIC, respectively.

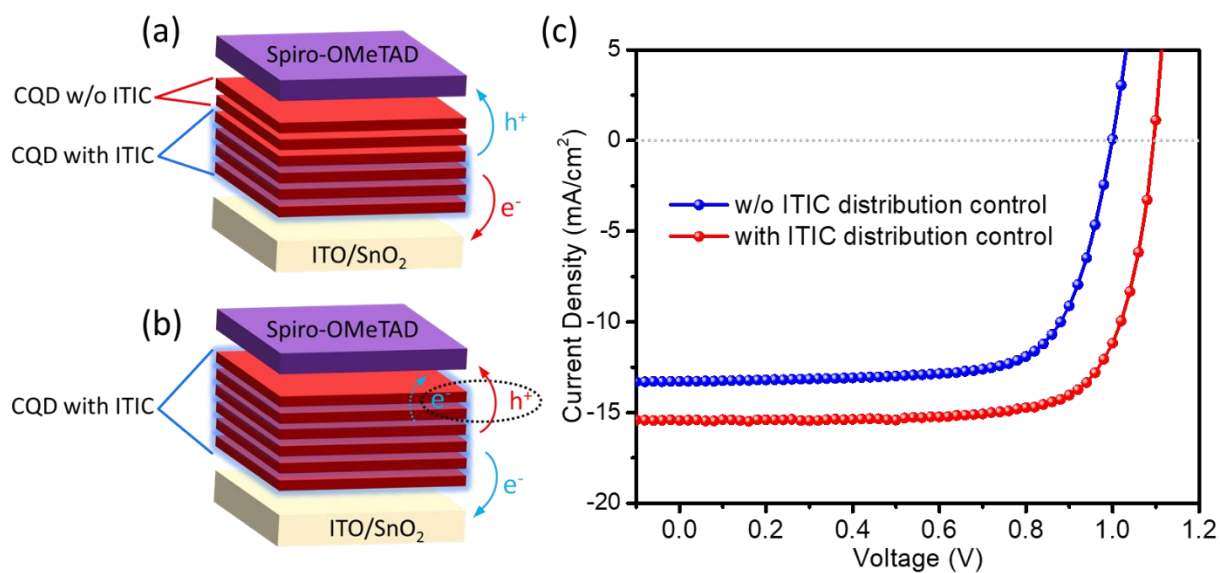


Figure A3.11 Schematic diagrams of FAPbI₃ CQDs-based solar cell devices a) with and b) without the control of ITIC distribution. c) *J-V* curves of the corresponding devices with and without ITIC distribution control.

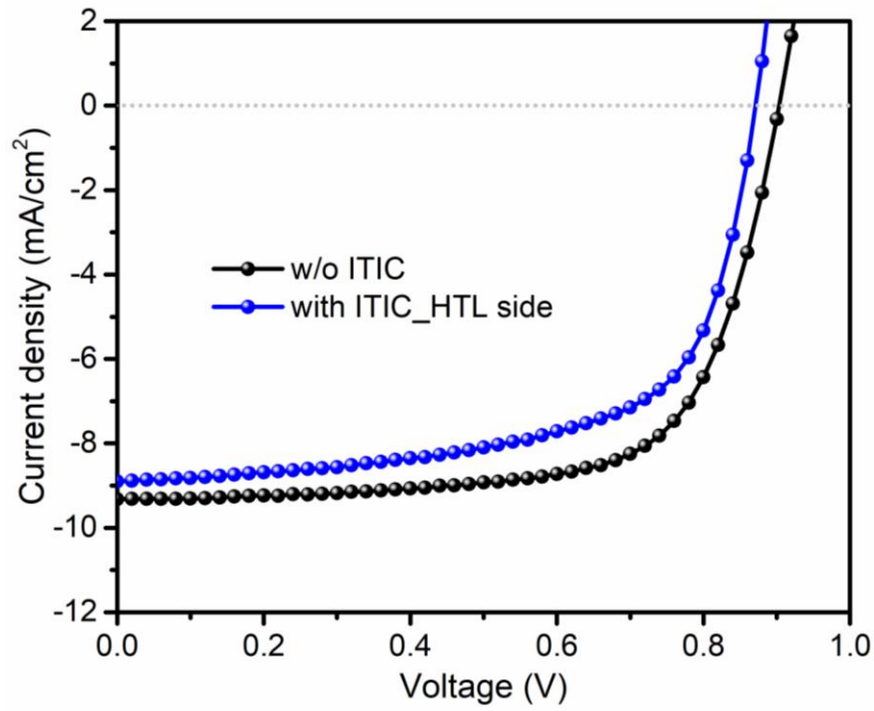


Figure A3.12 *J-V* curves of the QD devices without ITIC and with ITIC only located at HTL side.

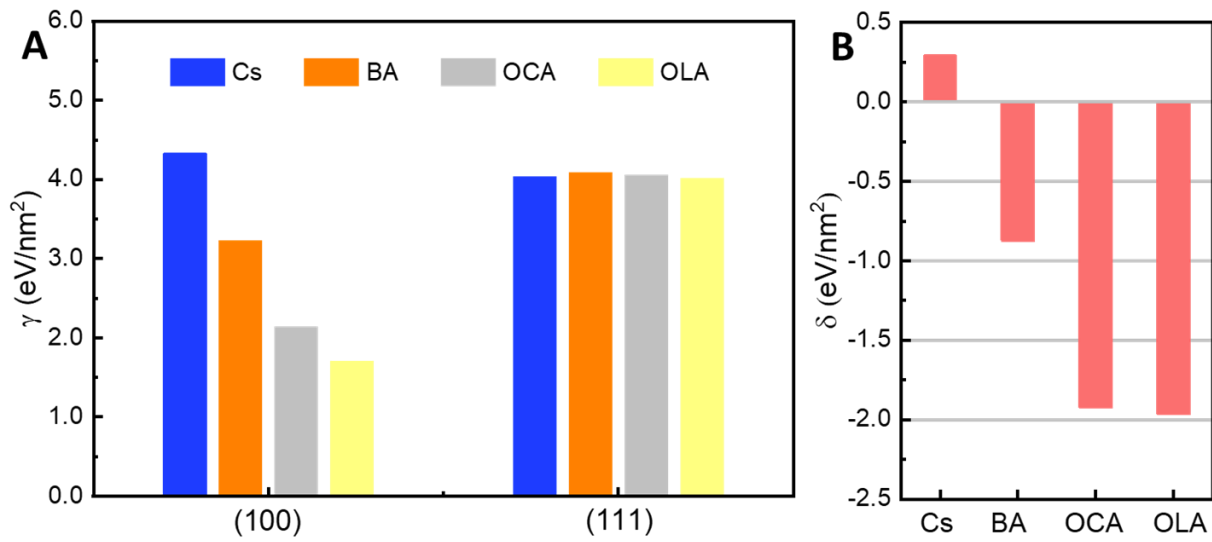


Figure A4.1. (A) The calculated surface energy γ of plane (100) and (111) for CsPbI₂Br slabs terminated with Cs, BA, OCA and OLA. (B) $\gamma_{100} - \gamma_{111}$ for CsPbI₂Br slabs terminated with Cs, BA, OCA and OLA.

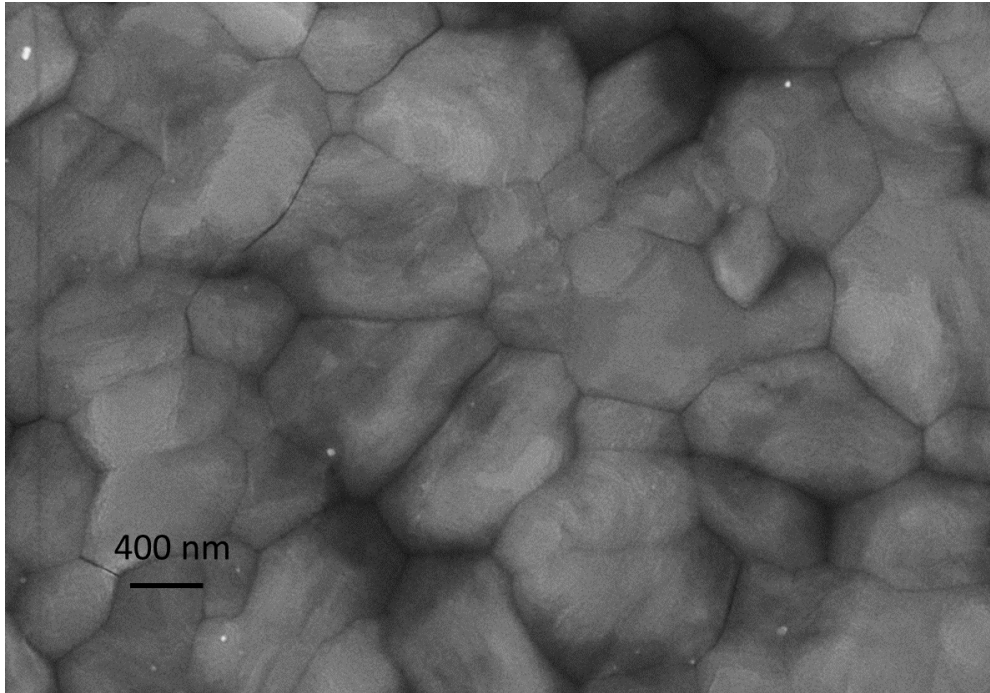


Figure A4.2. SEM image of CsPbI₂Br film without IPA treatment.

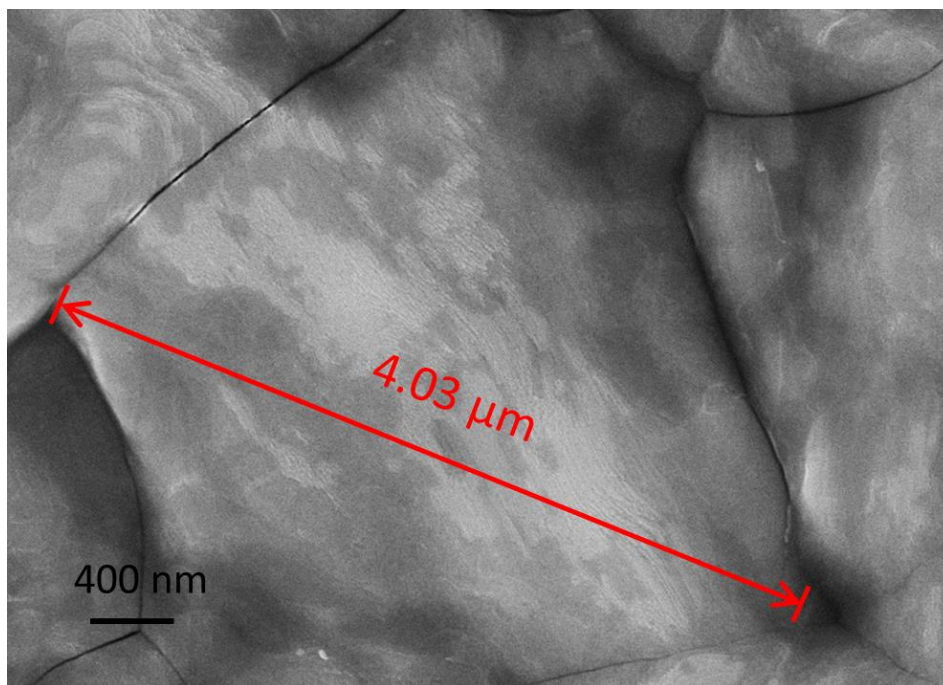


Figure A4.3 SEM image of CsPbI₂Br film with OLA treatment. The grain size is as large as 4 microns.

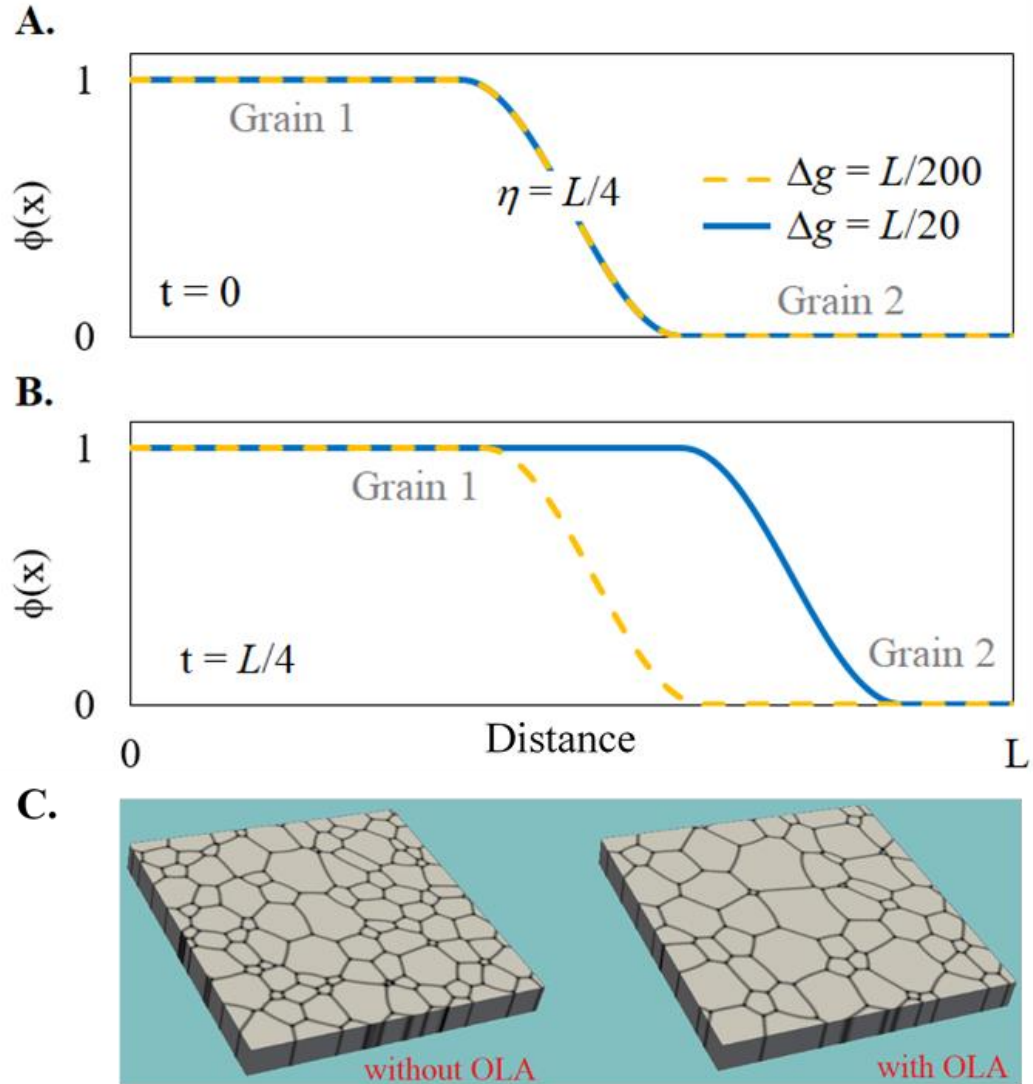


Figure A4.4. (A)-(B) A demonstration of the Phase-field model: analytical calculations of a 1D grain growth with a smooth interface and two different driving forces, $\Delta g = L/200$ and $\Delta g = L/20$, where $\Delta g = v/\mu$ and μ is taken to be unity. (A) initial condition ($t=0$), (B) at a later time ($t=L/4$). L : total length, η : interface width. (C) Snapshots of a 3D simulated grain growth of CsPbI₂Br films without OLA and with OLA treatments.

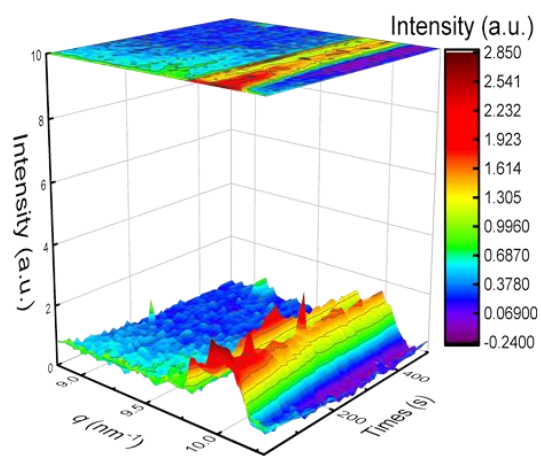
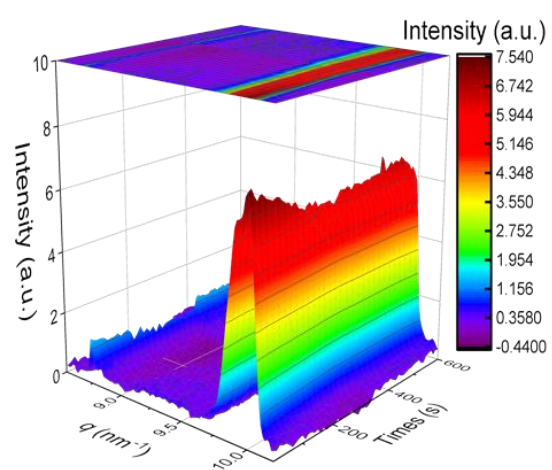
A.**B.**

Figure A4.5 3D in-situ GIWAXS patterns of CsPbI₂Br films. (A) without OLA treatment; (B) with OLA treatment.

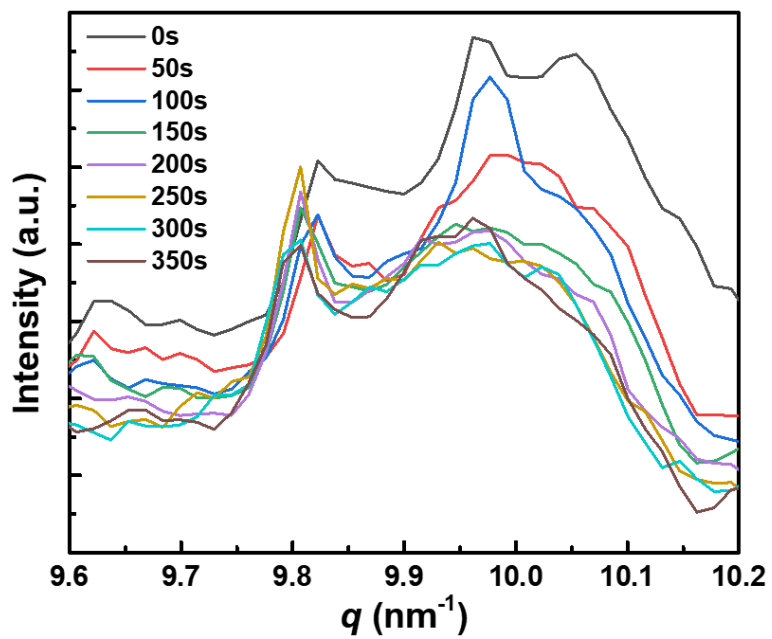


Figure A4.6 Evolution of 1D GIWAXS patterns of CsPbI₂Br films without OLA treatment.

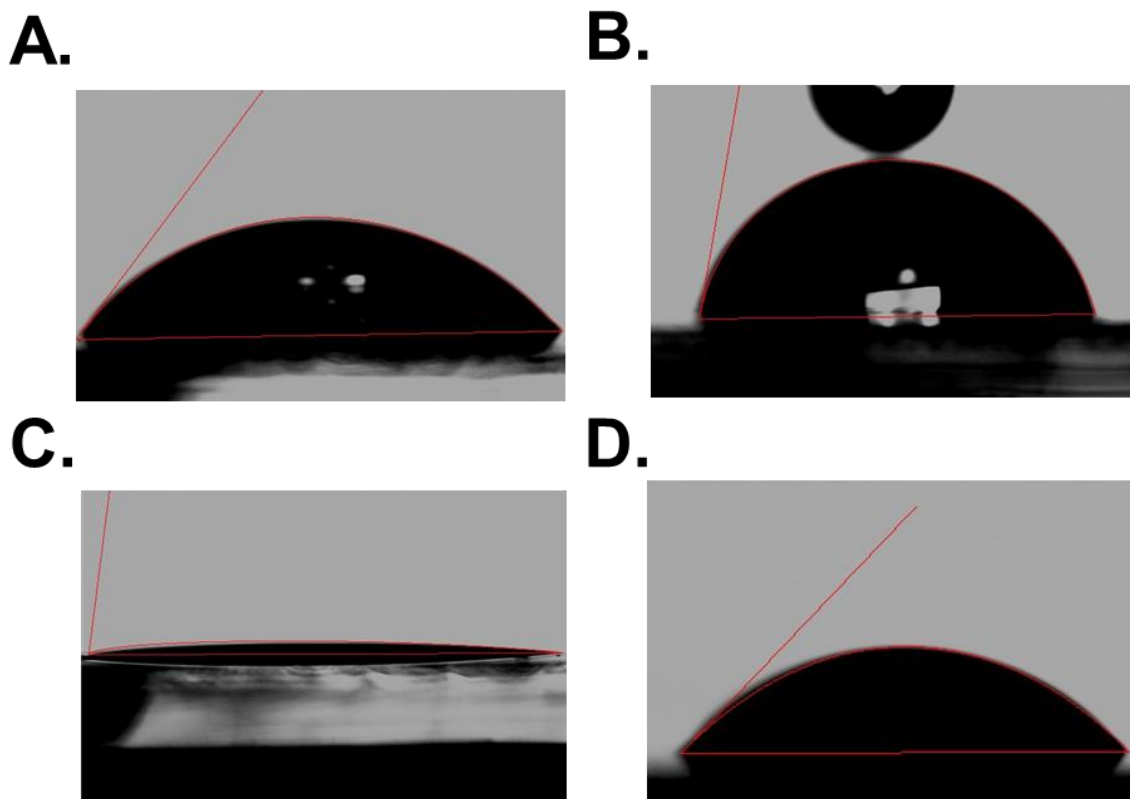


Figure A4.7 Contact angles of H₂O with CsPbI₂Br films. (A) without OLA treatment and (B) with OLA treatment on H₂O; and of diiodomethane (DIM) with CsPbI₂Br films (C) without OLA treatment and (D) with OLA treatment.

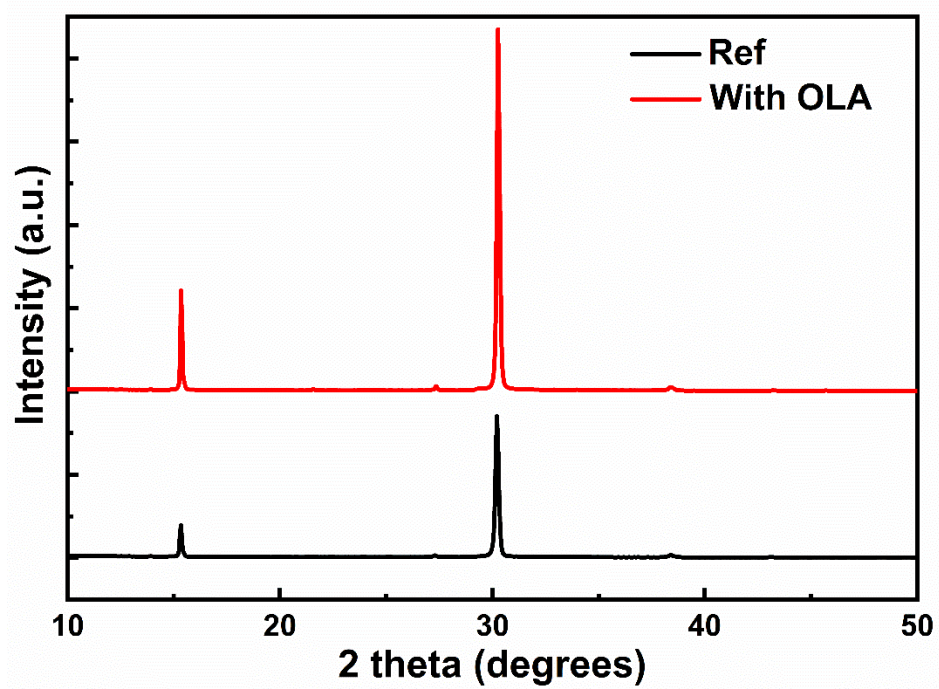


Figure A4.8 XRD patterns of CsPbI₂Br films with and without OLA treatment.

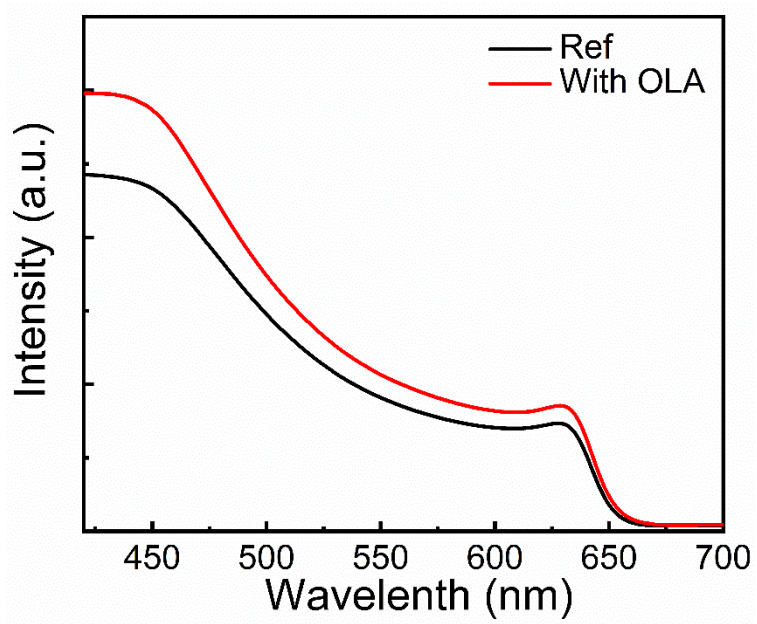


Figure A4.9. UV-Vis spectra of CsPbI₂Br films with and without OLA treatment.

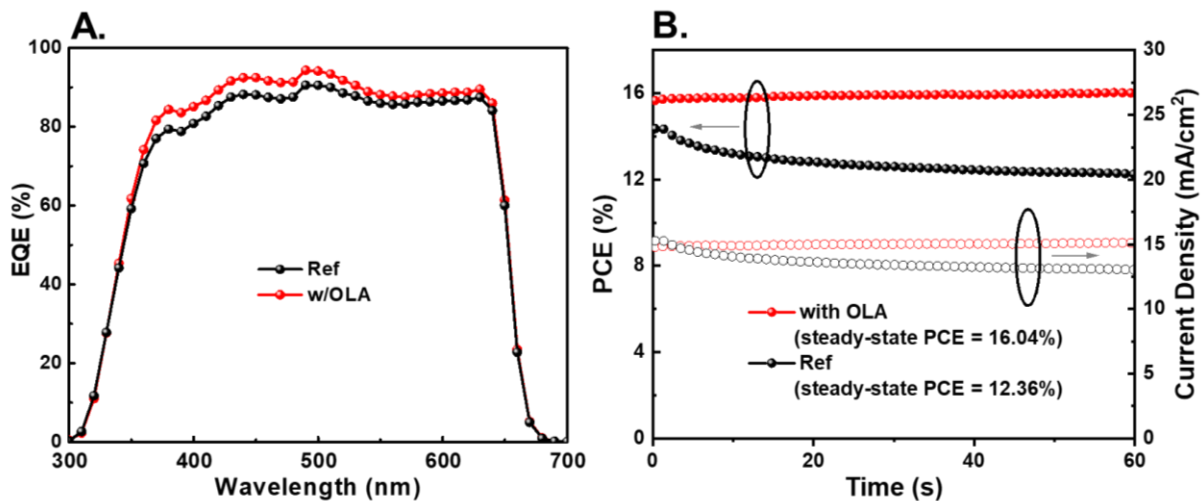


Figure A4.10 (A) EQE curves of the devices with or without OLA treatment. (B) Stabilized maximum power output and the photocurrent density at maximum power point as a function of time for the best performing perovskite solar cells with or without OLA treatment, as shown in Figure 4A, recorded under simulated one-sun AM1.5G illumination.

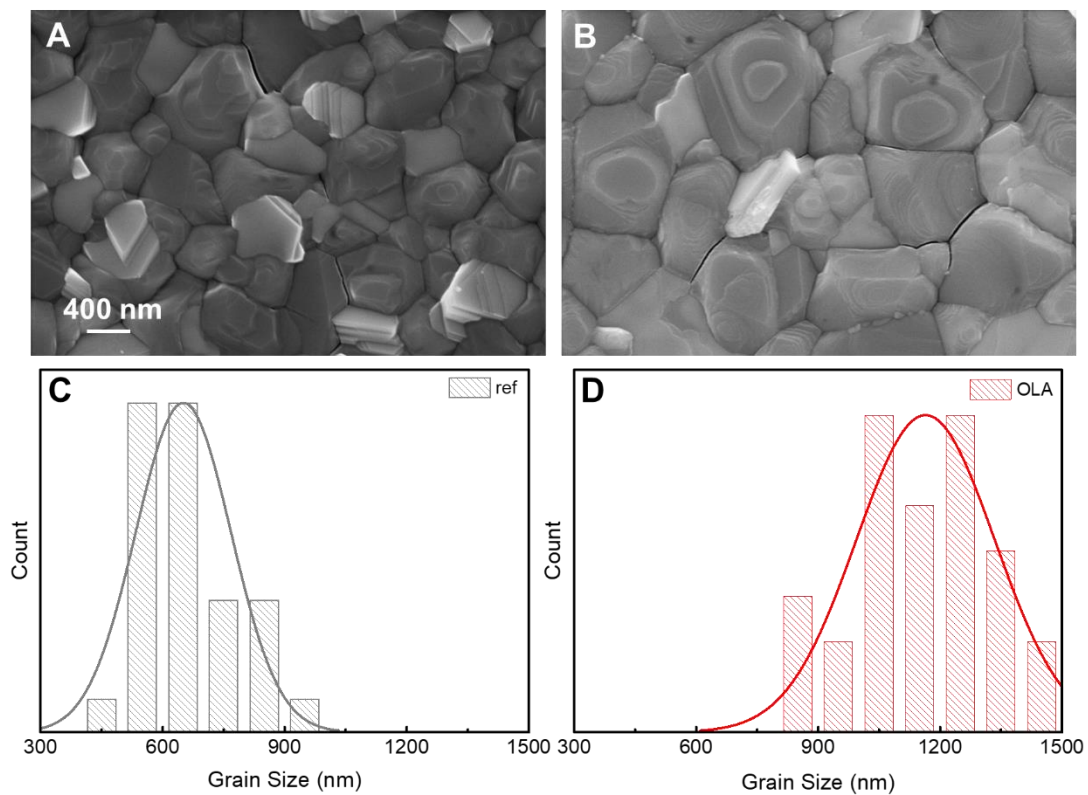


Figure A4.11 SEM image of FA-based perovskite films (A) without and (B) with OLA treatment. Grain size statistical distribution of FA-based perovskite films (C) without and (D) with OLA treatment.

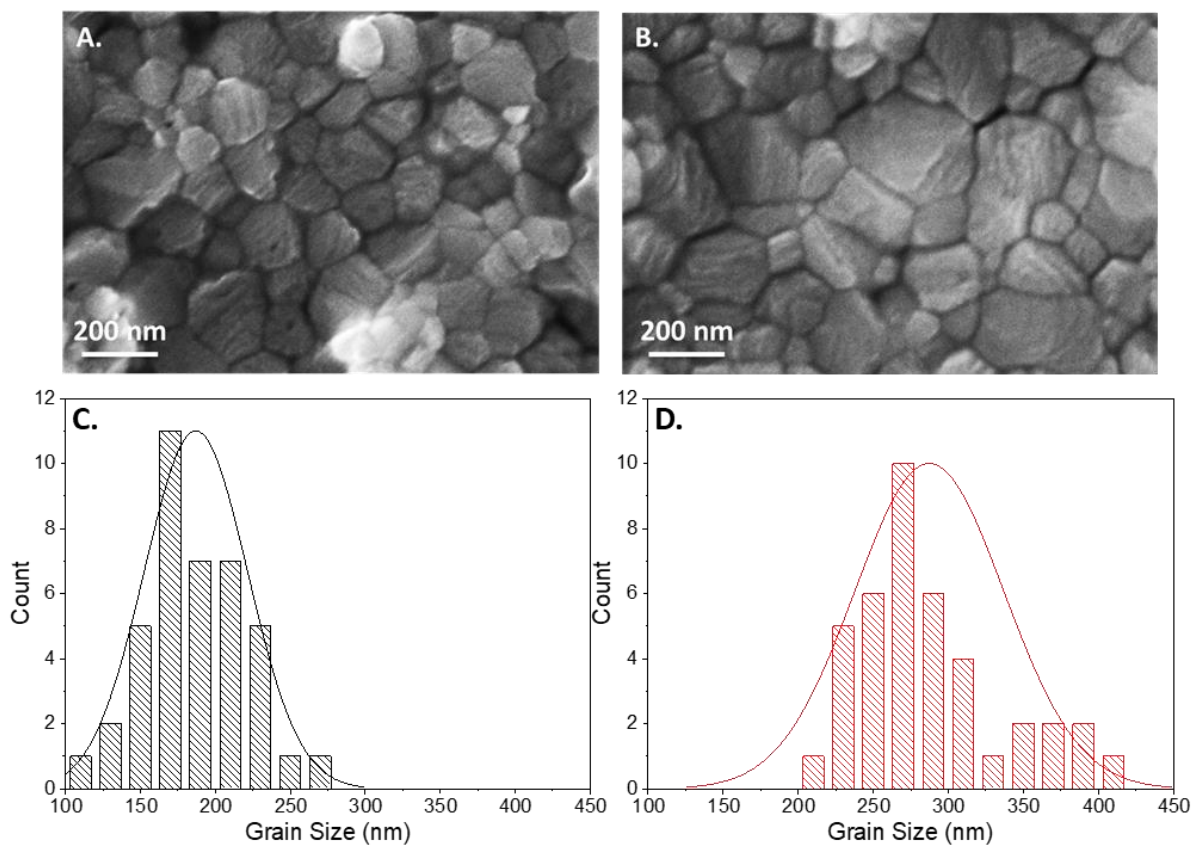


Figure A4.12. SEM image of MA-based perovskite films (A) without and (B) with OLA treatment. Grain size statistical distribution of MA-based perovskite films (C) without and (D) with OLA treatment.

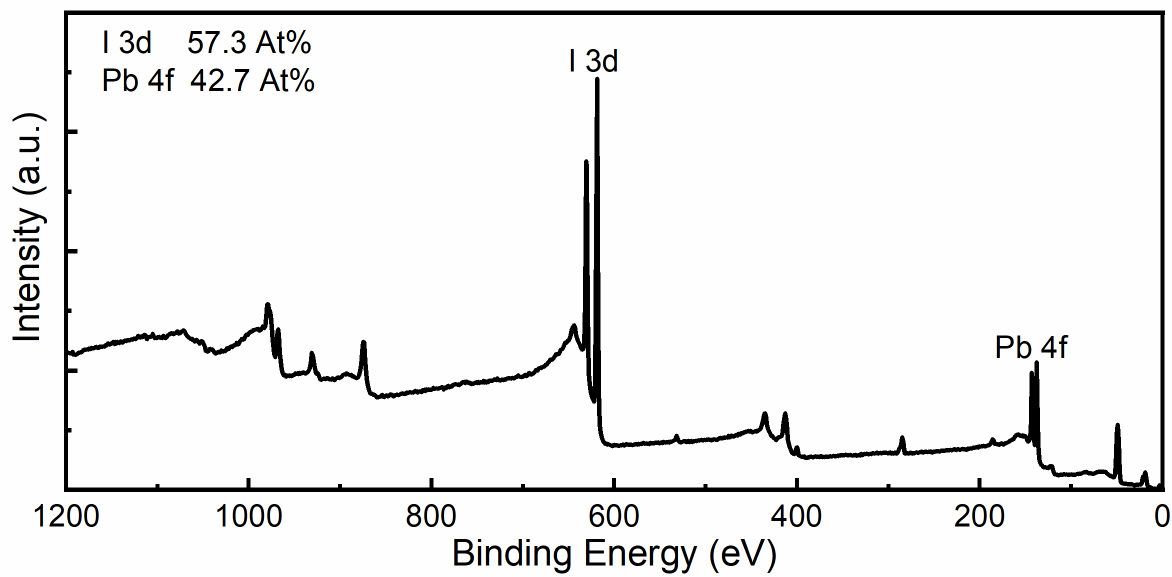
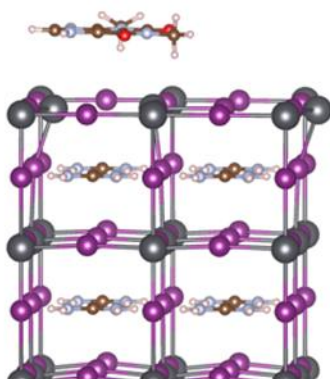


Figure A5.1 XPS full scan of the reference perovskite film, Pb 4*f* and I 3*d* peaks were integrated to determine the surface composition.

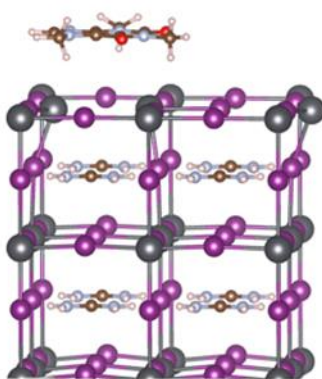
Iodine vacancy

w Theophylline



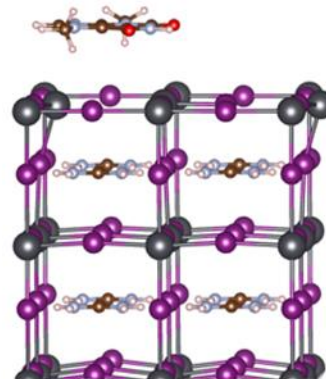
$$E_{\text{int}} = +0.68 \text{ eV}$$

w Caffeine



$$E_{\text{int}} = +0.84 \text{ eV}$$

w Theobromine



$$E_{\text{int}} = +0.72 \text{ eV}$$

Figure A5.2 DFT-D3 predicted interaction energies between the molecule and slab complex for the V_I case.

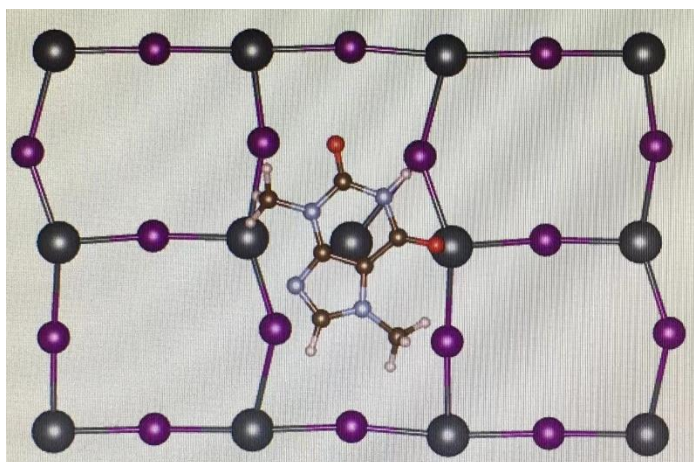


Figure A5.3 Top view of theoretical model of perovskite with theobromine surface passivation of Pb_I antisite.

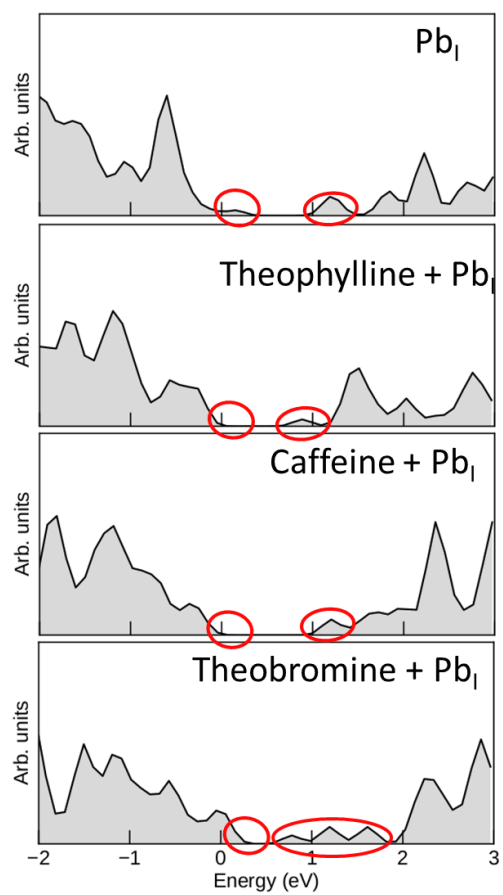


Figure A5.4 Theoretically Predicted *t*DOS of the surface Pb_I antisite defect with or without small molecule treatment.

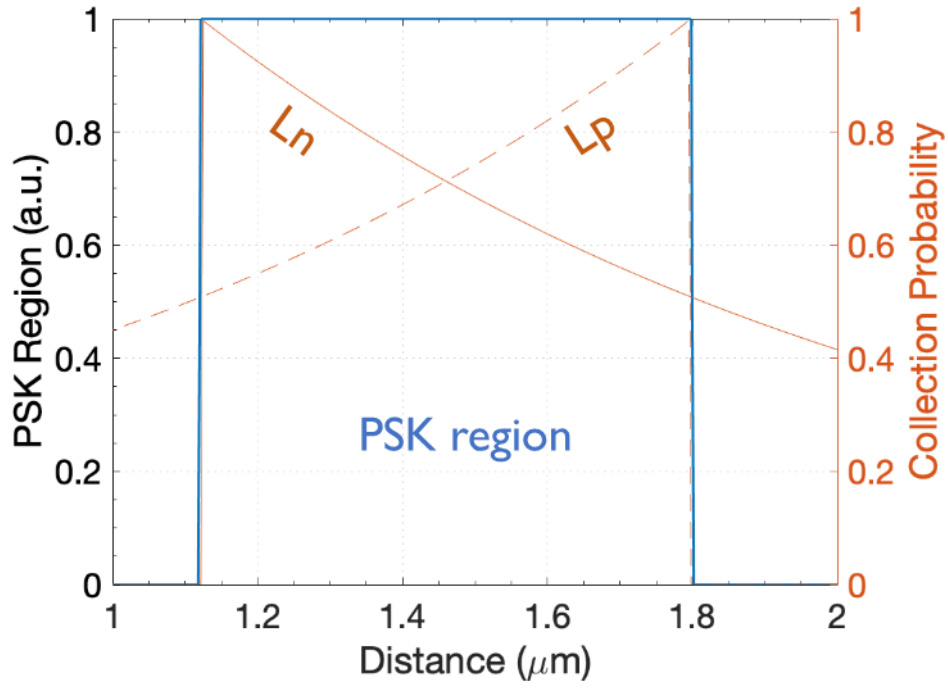


Figure A5.5 Carrier extraction probability extracted from EBIC.

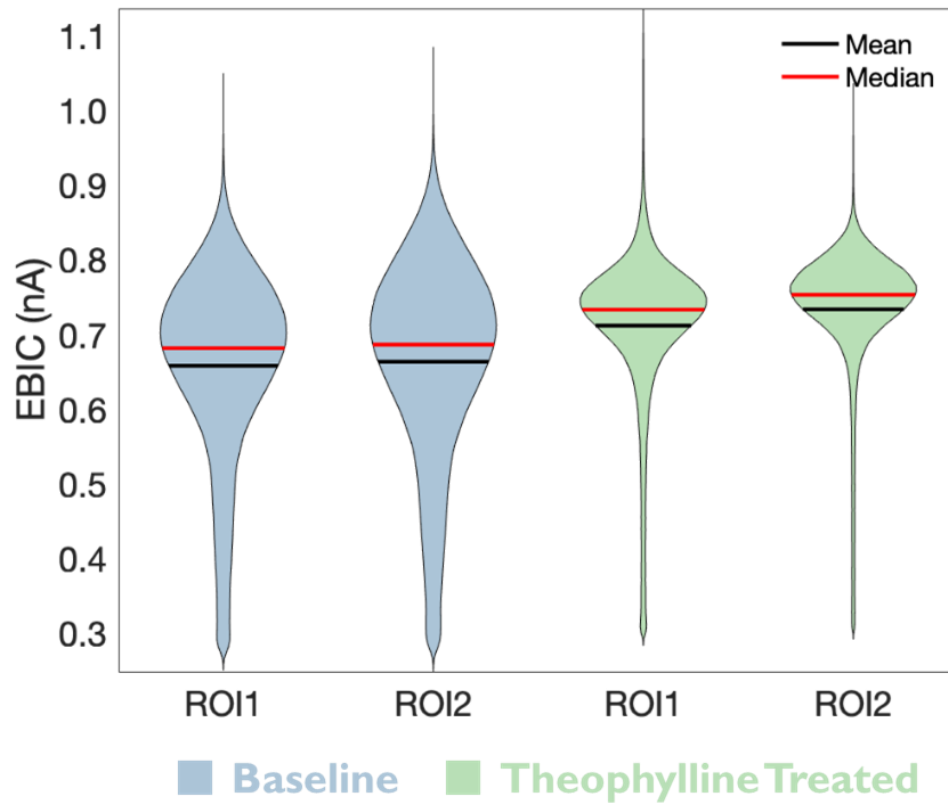


Figure A5.6 EBIC distribution profiles of perovskite active layers with or without theophylline treatment.

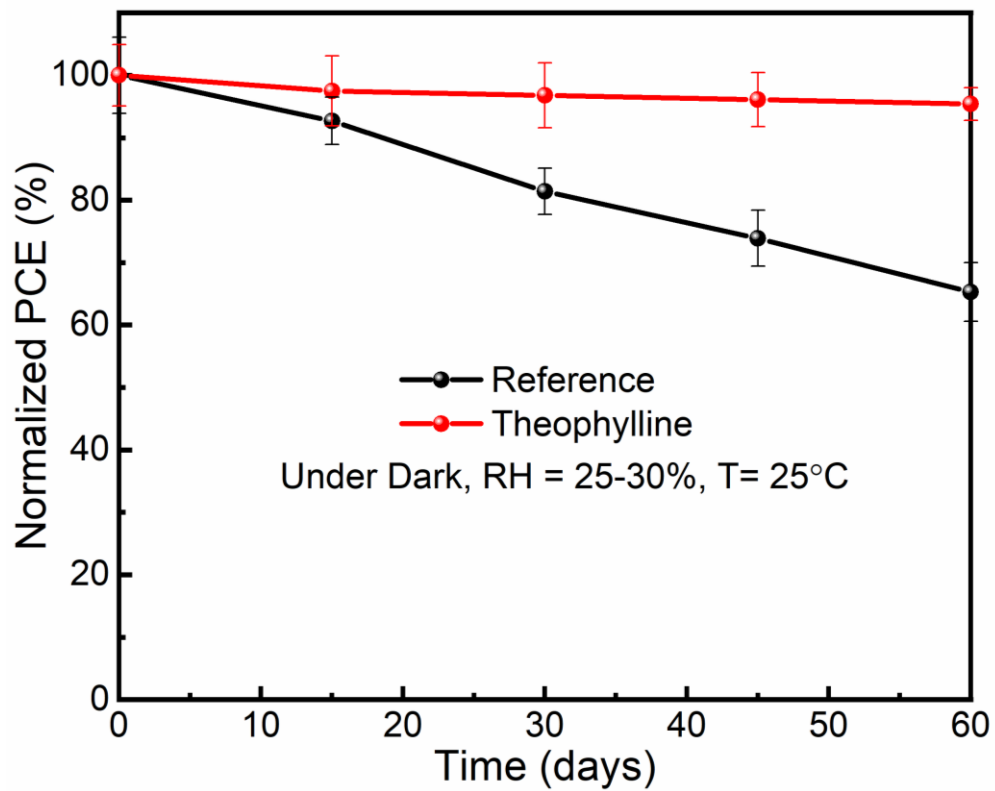



Figure A5.7 Evolution of power conversion efficiency (PCE) of perovskite solar cells with or without theophylline treatment. The devices were stored under dark with controlled humidity.

Appendix B

Table B2.1 Fitted parameters for time-resolved photoluminescence (PL) decay profiles of FAPbI₃ and CsPbI₃ CQDs in Figure 1. The data were fitted to biexponential decay model (*intensity* = $A_1 e^{-t/\tau_1} + A_2 e^{-t/\tau_2} + B$ where A_1 , A_2 and B are constants, t is time, τ_1 and τ_2 are lifetimes). The average lifetimes (τ_{ave}) were calculated by $\tau_{ave} = A_1 \tau_1 + A_2 \tau_2$.

Parameters	FAPbI ₃ CQDs	CsPbI ₃ CQDs
A₁ (%)	65.6	99.9
τ_1 (ns)	25.3	2.7
A₂ (%)	34.3	0.01
τ_2 (ns)	158.3	12.2
τ_{ave} (ns)	70.9	2.7

Table B2.2 Summary of solvents used for ligand treatment of FAPbI₃ CQDs⁵. The polarity of mixed solvent was determined by the arithmetic average of solvent polarity adjusted according to the volume fraction of each solvent.⁷



'Grade I' solvent				
Name	Water	Methanol	Ethanol	Isopropanol
Relative polarity index	1.000	0.762	0.654	0.546
'Grade II' solvent				
Name	t-butanol	2-pentanol	ACN/toluene (v:v 2:3)	EtOAc
Relative polarity index	0.506	0.488	0.243	0.228
'Grade III' solvent				
Name	CB	Toluene	Octane	Hexane
Relative polarity index	0.188	0.099	0.012	0.009

Table B2.3 Photovoltaic parameters of FAPbI₃ CQD solar cells with different cycles of ligand treatment. Short-circuit current density (J_{SC}), open circuit voltage (V_{OC}), fill factor (FF), power conversion efficiency (PCE).

Ligand treatment cycle	J_{SC} (mA/cm ²)	V_{OC} (V)	FF	PCE (%)
1-cycle	1.35	0.62	0.324	0.27
2-cycle	8.17	0.99	0.531	4.31
Solid state	11.84	1.10	0.644	8.38

Table B2.4 Photovoltaic parameters of FAPbI₃ perovskite solar cells based on bulk and CQD thin films. J_{sc}, V_{oc}, FF, PCE and stabilized power output (SPO).

		J _{sc} (mA/cm ²)	V _{oc} (V)	FF	PCE (%)	SPO (%)
Bulk	reverse	21.71	1.07	0.675	15.68	14.4
	forward	21.81	1.04	0.592	13.42	
QD	reverse	9.72	0.98	0.721	6.87	6.9
	forward	9.61	0.98	0.736	6.93	

Table B4.1 Calculated surface energies based on DFT-D3 method. Ref. refers to the case where Cs⁺ cations are present in the top layer, whereas they are replaced by BA, OCA and OLA for the remaining cases.

Type of Treatment	γ_{100} (eV/nm ²)	γ_{111} (eV/nm ²)	δ (eV)
Ref.	4.33	4.03	+0.29
BA	3.23	4.09	-0.87
OCA	2.14	4.06	-1.92
OLA	1.71	4.01	-1.96

Table B4.2. The contact angles of H₂O and DIM on CsPbI₂Br with or without OLA treatment and their respective calculated surface free energies.

<i>i</i>	H ₂ O (°)	DIM (°)	γ_s [mN m ⁻¹]
Ref	46.3	7.4	59.78
OLA	76.1	46.3	38.38

Table B4.3 Surface formula, number of formula per unit cell and atomic energy term that enter γ^{clean} for the calculation of surface energies at $T = 0$ K. n is the number of formula units per unit cell.

Slab	Formula	n	$2A * \gamma^{clean} + nE^{bulk} - E^{slab}$
100	$CS_nPb_nI_{2n+1}Br$	3	$-E_I$
010	$CS_nPb_nI_{2n+1}Br$	3	$-E_I$
001	$CS_nPb_nI_{2n}Br_{n+1}$	3	$-E_{Br}$
110	$CS_{n-1}Pb_nI_{2n}Br_n$	4	E_{Cs}
101	$CS_{n-1}Pb_nI_{2n}Br_n$	4	E_{Cs}
011	$CS_{n-1}Pb_nI_{2n}Br_n$	4	E_{Cs}
111	$CS_{n-1}Pb_nI_{2n}Br_n$	8	E_{Cs}

Table B4.4. Average and the best device data based on CsPbI₂Br treated with or without various types of organic ammoniums.

Type of Treatment	Voc (V)	Jsc (mA cm ⁻²)	FF (%)	PCE (%)	
				average	best
Ref	1.103±0.02	15.15±0.25	0.73±0.05	12.17±1.05	13.13
BA	1.137±0.01	15.96±0.46	0.75±0.03	13.55±0.28	14.01
OCA	1.166±0.02	16.29±0.25	0.76±0.01	14.44±0.38	14.94
OLA	1.231±0.01	16.48±0.26	0.80±0.01	16.23±0.28	16.58

Table B5.1 ΔH_a , formation energy of neutral defects considered in this study. The energies are in eV.

Defect type	ΔH_a (eV) Surface	ΔH_a (eV) Bulk
I _{Pb}	3.15	3.89
Pb _I	0.57	1.46
V _I	0.51	0.63
V _{Pb}	3.20	2.97

Table B5.2 Photovoltaic parameters of average and the best perovskite solar cells with or without various types of surface treatments.

Type of Treatment	Voc (V)	Jsc (mA cm ⁻²)	FF	PCE (%)	
				average	best
Ref	1.153±0.02	24.19±0.35	0.73±0.07	20.36±0.53	21.02
Theophylline	1.187±0.01	24.74±0.46	0.77±0.02	22.61±0.58	23.48
Caffeine	1.168±0.02	24.63±0.39	0.75±0.01	21.58±0.69	22.32
Theobromine	1.151±0.02	24.36±0.43	0.70±0.03	19.63±0.65	20.24

Table B5.3 Photovoltaic parameters of best perovskite solar cells under reverse or forward scan with or without theophylline treatment.

Type of Treatment	V_{oc} (V)	J_{sc} (mA cm⁻²)	FF	PCE (%)
Reverse (Ref)	1.164	24.78	0.729	21.02
Forward (Ref)	1.159	24.19	0.693	19.43
Reverse (Theophylline)	1.191	25.24	0.781	23.48
Forward (Theophylline)	1.191	25.23	0.749	22.51